Pattern Reconfigurable Antenna Using Active Frequency Selective Surface

By:

Naeemeh Hamidi

A dissertation submitted in partial fulfillment of the requirements for the degree of
Master of Science in Telecommunications

Evaluation committee

Research Director	Prof. Tayeb A. Denidni
	INRS-EMT
Internal examiner	Prof. Tarek Djerafi
and jury president	INRS-EMT
External examiner	Prof. Raed Shubair
	Khalifa University

Contents

List of Figures

[4]

[5]

List of Tables

ABSTRACT

With the widespread improvement of wireless communication systems and appearing the new generation of mobile telecommunications such as 4G as well as 5G, a transmission of information with high data rate is feasible. Antenna is an important part of telecommunication systems where the information is transmitted and received. Most importantly, to improve the communication link and cover more users, in particular in base station antenna, it is necessary to steer the beam radiation of the antenna. This can be carried out mechanically as well as electronically which each one has its drawback and advantage. In mechanical approach, the installation infrastructure brings more difficulty. Also, in electronic methods due to using the phase shifter, it incurs a large loss and complexity to the design.

In this thesis, first and foremost, a reconfigurable radiation pattern antenna based on frequency selective surfaces is introduced. To implement that idea, a modified electric-field coupled (ELC) resonators is presented, which works at 2.4 GHz. To transmit and reflect the illuminated power a pin diode is integrated in the middle of ELC resonator, where by turning "on" or "off", the resonant frequency of transmission coefficient is shifted to a desired frequency band.

Then, the stair-case monopole antenna operating at 2.4 GHz is proposed in the next part which is surrounded by octagon FSS walls, where each one consists of a 2x3 ELC inclusions. By switching "on" three FSS walls and keeping remaining walls in off-state, the radiation pattern in azimuth plane is switching from omnidirectional to directional pattern. To validate, a prototype of antenna along with eight FSS walls incorporated by pin-diode is fabricate and attached to the control unit part. The measured reflection coefficient of the antenna is less than -10 dB over 2.35-2.55 GHz. The measured radiation pattern in H-plane clearly shows a directional beam in different states with a measured realized gain of more than 5 dBi.

To receive a maximum power in a random angle, a transmitted antenna propagates power and the aforementioned antenna with FSS panel is switched in 8 cases by control unit part.

Finally, a design of control unit interface with proposed reconfigurable pattern antenna is presented and discussed in more details.

ACKNOWLEDGMENTS

First of all, I sincerely wish to thank my supervisor Prof. Tayeb A.Denidni, who gave me the opportunity to join his research group. It was a real pleasure for me to have such an exceptional scholar and it was my honor to be his master student.

Chapter 1 Introduction

1.1 Motivation

Reconfigurability in terms of radiation pattern is crucial for wireless communications systems since it can improve the link quality and reduces the interference and most importantly increase the signal to noise ratio. Reconfigurable antennas offer flexibility in terms of frequency, pattern, and polarization, hence versatile and flexible operations in many applications. In fact, in a rich scattering environment, it is imperative to design antenna element with desired radiation patterns into a predefined angle so as to re-direct the beam radiation for covering more areas and users and suppressing the undesired signals from other directions. Thus, a multipath propagation fading can be reduced which in turn results in the improvement of spectral efficiency by taking into account the fact that the higher rate of information can be transmitted in a given bandwidth [1], [2].

Several works have been introduced to achieve a reconfiguarable radiation pattern such as the use of RF p-i-n diodes [3], [4], microelectromechanical system (MEMS) switches, varactor diodes, GaAs FET switches [5], or mechanical actuation. Reconfigurable antennas using p-i-n diodes suggest high reliability, fast switching speed, and more efficiency in terms of cost as opposed to MEMS [6]. Furthermore, more study has been investigated to substitute p-i-n diodes due to the power consumption of MEMS, high isolation, and considerable low insertion loss. However, they are costly and it is required a power-up converter chip to generate high voltages of 30–80 V [7].

The radiation pattern of the antenna element could be unidirectional, bidirectional, multidirectional or omnidirectional. In reconfigurable radiation pattern, the radiated beam can be redirected from one pattern to another one [7–12]. For instance, the radiation pattern of the antenna in [9] could be reconfigured from unidirectional to omnidirectional, wherein the radiation beam of the antenna in [8] could be reconfigured from bidirectional to unidirectional. For a unidirectional pattern, the main beam of the antenna can also be steered to different directions. A typical example of such type of beam steerable antennas is a phased-array antenna. As opposed to patch or slot antennas, a phased-array antenna has this capability to offer a more gain n and quick response to beam steering. Nevertheless, there are several drawbacks of phased-array antennas. First, the size of each array element is usually about a half-wavelength long, making the generation of grating lobe as well as an increase in total size of the antenna arrays. Second, a phased-array antenna system is usually incorporated with complex active device network requiring a number of phase shifters and power amplifiers. This element incurs large losses as well as increases the cost of the whole phased-array antenna system. Third, the shape of radiation beam may alter over beam steering [13]. As a consequence, researchers have investigated lots of works on pattern reconfiguration applying low-profile and low-cost antennas [7–9, 14]. For instance, the square loop antenna proposed in [15] could steer the tilted main beam in four different quadrants and hence scan the entire space in front of the antenna. This was indeed a low-profile solution for beam steering and easy to implement. However, the beam could not be steered continuously since the antenna could only be switched among four different states.

1.2 Problem identification

It is imperative to be familiar with link budget definition along with its performance to design appropriate system in this project. Thus, in this part, the explanation about the link budget is provided and we will present a conventional RF communication system to illuminate how we can maximize the link performance of the system by applying the proposed designed pattern reconfigurable antenna. In RF telemetry link the first parameter is the output power of the transmitter and the total gain as well as loss to recognize the real value of the power delivered to the receiver. To design a consistent link budget, the appropriate level of power in the receiver should be in excess of that required for a minimum level of performance.

An explanation of all the parameters such as gain as well as losses existed between the transmitter and the receiver is considered to as the link budget. The parameter of the link budget systems is included as shown in Fig. 1-1.

$$P_{RX} = P_{TX} - L_{TX} + G_{TX} - L_{PATH} + G_{RX} - L_{RX}$$

$$Fade\ Margin = P_{RX} - Rx\ Sensitivity$$
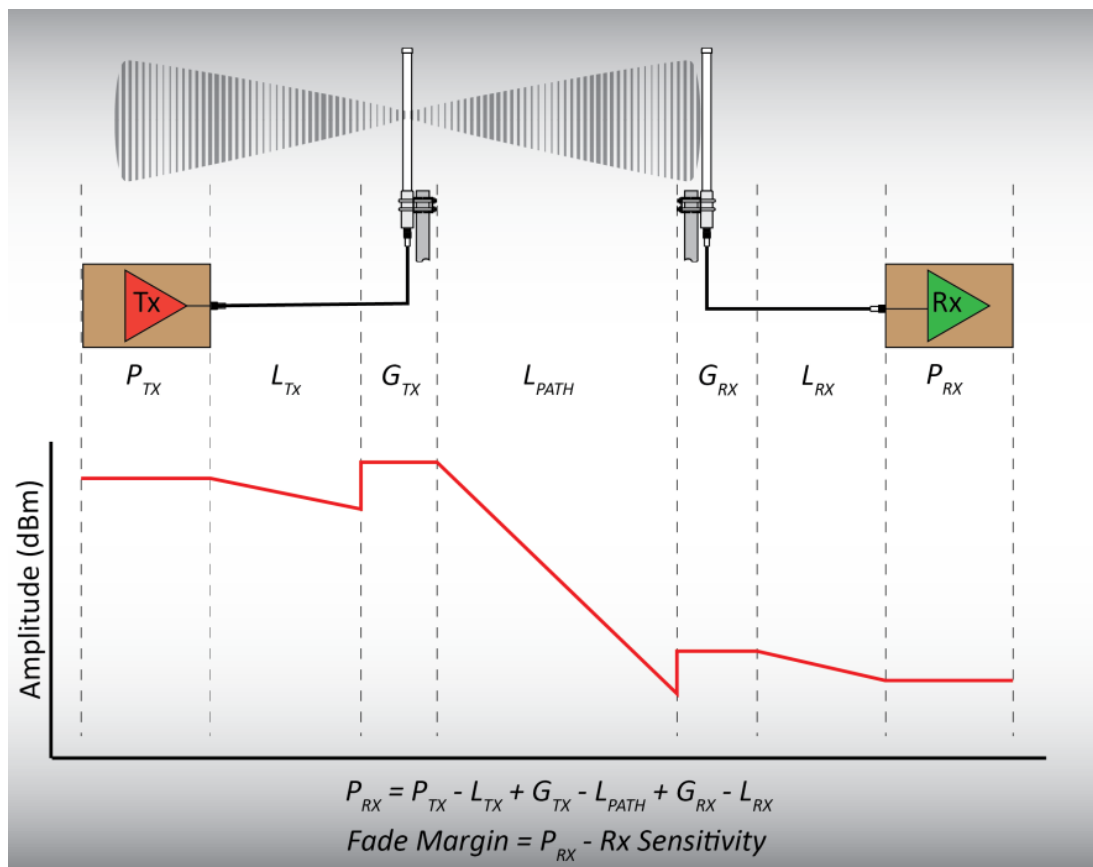
Fig. 1-1 System Gain-Loss Profile for a Link Budget[16].

Where:

P_transmit = the power in transmitter in terms of dBm.

L_transmit = the loss of system in terms of dB at transmitter.
GTX = the peak gain of antenna in terms of dBi at the transmitter.
Loss = the total losses of propagation losses in terms of dB between the antenna in transmitting and receiving modes.
GRX = the peak gain of antenna in terms of dBi at the receiver.
LRX = the entire system loss in terms of dB at the receiver.
PRX = the delivered power at receiver in terms of dBm.

The power level which is in excess of than that needed for a defined minimum level of system characteristics is related to as the fade margin. Since, it provides a border of safety in the state of a transitory attenuation or fading of the received signal power. The smallest received power level deployed for the link budget can be fully random—based on the designer's knowledge—but is most often related to the receiver's sensitivity. In fact, the receiver's sensitivity defines the least RF input power which is necessary to generate a functional output signal. A usual value for receiver sensitivity is in the range of –90 to –120 dBm.

To better recognize the mechanism of the link operation, we are employing a typical RF communication system called RF320 (INR RF320). This system includes:

- ✓ RF320 radio (both ends): The output power corresponds to 5 watts (37 dBm); the sensitivity of the system should be 0.25 µV (–119 dBm) for 12 dB SINAD (signal-to-noise and-distortion ratio); the operating frequency corresponds to 2.45 GHz.
- ✓ The radiation pattern of the antenna should be Omnidirectional and the peak gain corresponds to 3 dBd (5.15 dBi); VSWR (voltage standing wave ratio) < 2:1.
- ✓ The connector loss corresponds to 0.5 dB.
- ✓ The loss of transmission line at receiver and transmitter should be ≈ 0.5 dB.
- ✓ The path loss of propagation is an unbarred line of sight (LOS) over a smooth earth.
- ✓ Assume, the total distance between the transmitter and receiver is equal to 32.2 k.

Base on abovementioned assumption we can estimate the link budget

The transmitted power:

The RF320 RF output power is defined in terms of watts. To generate the output power the following equation is deployed in terms of watts to power in dBm:

$$P_{dBm} = 10\log(P_{watts}) + 30 \tag{1}$$

The output power of the above mentioned system corresponds to 5 watts.
Thus:

$$P_{dBm} = 10\log(5\ watts) + 30 \tag{2}$$

$$P_T = 37\ dBm \tag{3}$$

The loss of the system is the summation of the whole insertion loss in the transmission line in addition of any loss because of the mismatch impedance matching with antenna. There are other components in the RF systems such as coaxial cables, as well as possibly even bandpass filters

deployed to link the transceiver to the antenna, which causes a loss. In fact, each element in the transmission line which does not amplify will show some portion loss; a decrease in the level of output power compared to its input is known as insertion loss. In most states, the main loss will be considered to the insertion loss of the reasonably longer cable linking antenna mounted on tower. The characteristics of cable datasheet will naturally define its loss in a table indicating attenuation in dB per unit of length in terms of frequency.

When the output impedance of transceiver is matched to the antenna along with the transmission line, then the maximum power is delivered to antenna, however if there is a mismatch of impedance, it leads to a mismatch loss. It is possible that each component in the transmission line will demonstrate some small deviation from the standard 50 Ω characteristic impedance, and the net effect is the total of these cascading mismatches. However, the minimal effect of the transmission line on the link budget is neglected and the antenna mismatch is considered as the main loss. The most general impedance mismatch of the antenna called VSWR; for instance, VSWR < 2:1. The following equation is given to achieve a relation between the VSWR and mismatch loss.

$$Mismatch\ loss = -10\log\{1 - [\frac{VSWR - 1}{VSWR + 1}]^2\} \tag{4}$$

Therefore, a VSWR of 2:1 equates to a mismatch loss of 0.511 db.
Based on the preceding information, we can now calculate the system loss for both ends of the link.

$$Loss_T = surge\ Kit(-0.5) + cable(-1.7) + connectors(-0.5) + mismatch(-.0511) \cong$$
$$-3.2\ dB \tag{5}$$

$$Loss_R = surge\ Kit(-0.5) + cable(-0.85) + connectors(-0.5) + mismatch(-.0511) \cong$$
$$-2.35\ dB \tag{6}$$

Antenna Gain:

The value of the antenna gain employed in a link budget is presented in terms of dBi, which is in relation to state when the antenna radiates isotopically. It is conventional for a manufacturer's datasheet to indicate the peak gain of antenna in units of dBd, which is the relative gain compared to actual dipole antenna. In comparison with an isotropic radiator, a classical half wave vertical dipole antenna will demonstrate a gain of 2.15 dB in the azimuthal plane. The conversion of the gain in terms of in units of dBd to units of dBi is given as follows:

$$dBi = dBd + 2.15 \tag{7}$$

The RF320 antenna in the above example has a defined gain of 3 dBd. Thus, the estimation gain of transmitting and receiving antenna in terms of dBi is given as follows:

$$Gain_T = Gain_R = 3 + 2.15 \tag{8}$$

$$Gain_T = Gain_R = 5.15\ dBi \tag{9}$$

[13]

Path Loss:

In most states, the path loss is the key factor to loss in the link budget. It is the summation of free space loss along with the other losses induced by the interaction of the electromagnetic waves with the ground and/or obstacles along the direction of propagation.

The propagation of the Line-of-Sight:

In the most common RF link, the principle mode of electromagnetic waves propagates in line of sight, which is a direct path between the antenna in transmitting and receiving modes. Thus, for a single element antenna, the maximum direction of propagation is restricted by the distance to the RF horizon. As demonstrated in Fig. 1-2, the RF horizon is different from the optical horizon.
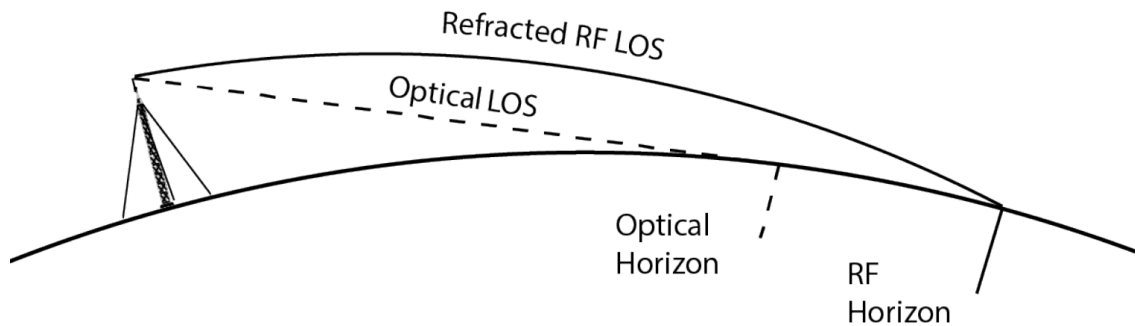
Fig. 1-2 Optical Horizon vs. RF Horizon.

The optical horizon originates from an optical straight path line which corresponds to a straight direction of distance from the antenna to a defined curve line to the earth's surface. In fact, the RF signal travers a bend path line which is primarily located in parallel of the surface of the earth , however, it is curved because of the refractive index of the that is initially parallel to the earth's surface but is progressively bent toward the surface due to the refractive properties of the air. Thus, the space to the RF horizon point is roughly 7 percentages more than the space to the optical horizon. For a conventional atmosphere (which the refractive index is 1.33) over a flat earth, the distance to the RF horizon is determined based on the height of the antenna as follows:

$$t_{HOR} = 4.14\sqrt{l} \tag{10}$$

t_{HOR}= relative space to the Rf horizon in terms of kilometers
l= the distance of the antenna to earth

In the RF system link, the maximum line-of-sight path space corresponds to the summation of the RF distance point when the antenna works in transmitting and receiving mode:

$$HLS_{MAX} = 4.4\sqrt{L_T} + 4.4\sqrt{L_R} \tag{11}$$

Thus, for the aforementioned RF link:

$$HLS_{MAX} = 4.4\sqrt{30} + 4.4\sqrt{10} \tag{12}$$

$$HLS_{MAX} = 35 \; km \tag{13}$$

In order to the Rf link to be taken into account as line of sight, the space of the antenna in two modes of transmitting and receiving should be the same or less than the maximum line of sight path length as follows :

$$t_P \leq LOS_{MAX} \tag{14}$$

Thus, when the distance between the transmitter and receiver antenna is 32 km we can consider proposed RF link as LOS since its value is less than maximum estimation which is 35 km.

Free Space Model:

When electromagnetic waves propagate in free space density of the power is minimized. These facts give rise to the classic free space loss equation:

$$dfL_{dB} = 32.5 + 20\log(t) + 20\log(f) \tag{15}$$

Where:
dfL_{dB} = free space loss in terms of dB
t = distance in terms of kilometers
f = frequency in terms of Gigahertz

Thus, for a distance of 32.1 km and the frequency of 2.45 GHz:

$$dfL_{dB} = 32.5 + 20\log(32.1) + 20\log(2.45) \tag{16}$$

$$dfL_{dB} = 107.2 \; dB \tag{17}$$

However, the loss of free path length is deployed in the estimation of link budget it is imperative to be aware of that in this section. In fact, the expressions free space means that there is no atmosphere as well as no curved surface. Thus, this does not represent a real environment to calculate the precise link budget.

2-Ray Multipath Propagation:

In the real environment the electromagnetic waves will face unavoidable things or a natural obstruction which restricts the calculation of link budget .In fact, the electromagnetic waves will

be scattered, refracted as well as diffracted which we have to consider the effect of multipath ray propagation in estimation of link budget.

If we do not have a precise knowledge about the propagation of the EM wave in this situation, it would be hard to distinguish the received signal in the receiver. For that purpose we deploy a software application employing established experimental propagation models linked to a GIS database to estimate the losses for blocked line-of sight path of propagation.
In fact, a conventional atmosphere as well as a free path line over a flat earth will be considered.
In the case when the receiver receives the signal, it is hard to say that the EM wave is related to direct path length. In most cases, the received signal is the combination of reflected wave as well as line of sight signal. Thus, the captured signal by the receiver is the summation of the amplitude and phase of line of sight direction and reflected signal.
In the free line of sight path, the most source of reflection is the curvature of the earth. This can cause a considerable effect when the distance between transmitter and receiver antenna is enough large. The configuration of direct path and reflected path for two rays of propagation is revealed in Fig. 1-3.
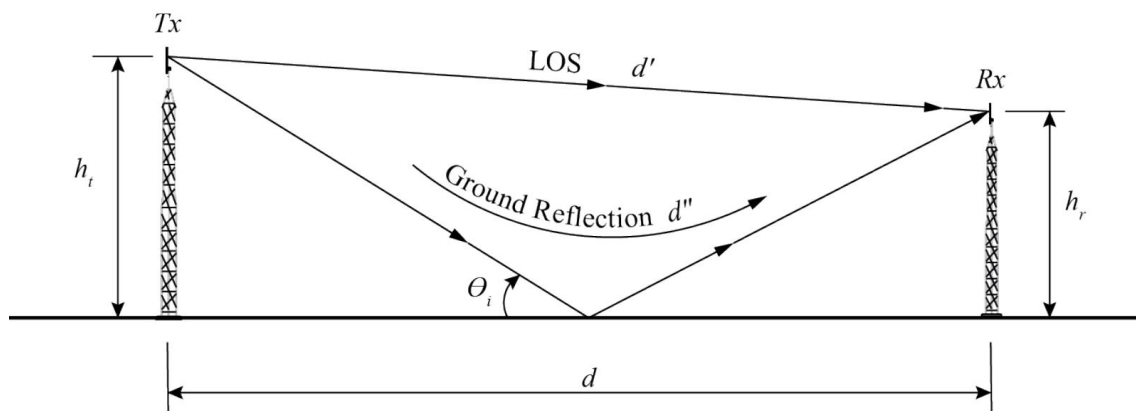
Fig. 1-3 Path Geometry for 2-Ray Propagation Model.

In fact, the reflected signal captured in the receiver has different amplitude and phase in comparison with the direct incident wave. The phase difference is attributed to the different path length of incident as well as reflected wave arriving at receiver. When the EM wave is polarized horizontally, there is a 180 degree in the point of reflection .Conversely, in the vertical polarization, the reflected wave has a phase shift when the angle of incidence is less than 30 degree, and also this can be equal 180 degree if the angle of incident wave is very small.

A large path direction has considerable effect on the amplitude of the reflected EM wave .The effect of combination of reflected EM wave along with the incident wave can be constructive or destructive. The positive effect happens when the EM wave is captured in phase ($\theta_{diff} < \pm 90$). In fact, when there is a zero phase shift and small variation in amplitude in return gives raise a 6 dBi gain in received signal strength as opposed to LOS EM wave. Also, when the wavefront is captured in the receiver by phase ($\theta_{diff} > \pm 90$), the reflected signal is out of phase with direct signal which has negative effect. Thus, this results in a cancellation of the signal and noting is delivered in the receiver

The power level of received signal:

Assuming, the input parameters of the link budget is defined and known , then the level of the received power in the receiving mode can be estimated as follows .

From Fig. 1-1:

$$P_{RX} = P_{TX} - L_{TX} + G_{TX} - L_{PATH} + G_{RX} - L_{RX} \tag{18}$$

Thus, the power received in the conventional RF320 system is as follows:

$$P_{RX} = 37\ dBm - 3.2\ dB + 5.15\ dBi - 13.8\ dB + 5.15\ dBi - 2.35\ dB = -89\ dBm \tag{19}$$

It should be mentioned that the sensitivity of the receiver determines the minimum input power which is required to produce appropriate output power. There is a key factor for determining the sensitivity of the receiver as follows:

✓ The required minimum input power to limit the errors in the received signal to a maximum Bit Error Rate (BER). The conventional value corresponds to: −103 dBm for 1 x 10^{-4} BER— specifying bit error for each 1000 bit .

For a 50 Ω system (the standard for the telecommunications industry), the following equation can be deployed to convert volts to power in dBm:

$$P_{dBm} = 10 \log \left[\frac{(V. 10^{-6})^2}{50} \right] + 30 \tag{20}$$

Where:
P$_{dBm}$ = power in dBm
V = rms voltage in microvolts

Thus, the sensivity of the usual RF320 system is given by:
Rx Sensitivity at 0.25 uV for 12 dB SINAD

$$Rx\ Sensitivity\ (P_{dBm}) = 10 \log \left[\frac{(0.25. 10^{-6})^2}{50} \right] + 30 \tag{21}$$

$$Rx\ Sensitivity = -119\ dBm \tag{22}$$

Fade Margin:

If we subtract the sensitivity of the receiver from the estimated received power, we can obtain the value to which transmitted path losses or signal fading can be tolerated before system performance is affected.

1. 3 Problem remedies and project objectives

In previous section, we discussed about the link budget and the system parameters of a typical communication link (INR RF320). As explained the performance of communication system is presented by the defined bit error rate (BER) curve. For achieving such a BER curve for a wireless communication link, it is imperative to explain the sub-system parameters such as maximum coverage area, as well as fad margin

A wireless local area network (WLAN) is a wireless computer network that connects two or more users deploying a wireless distribution method (often spread-spectrum or OFDM radio) in a limited area such as a home, school, computer laboratory, or office building. This brings about users the ability to move around within a local coverage area and yet still be linked to the network.

A WLAN can also prepare a broadband connection to the Internet. Most modern WLANs are based on IEEE 802.11 standards and are marketed under the Wi-Fi brand name. Fig. 1-4 shows the allocated channels for IEEE 802.11 standards.
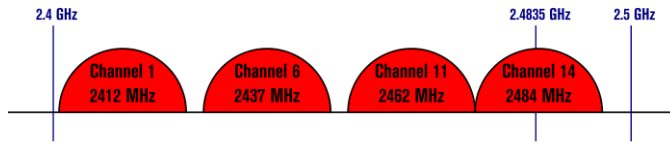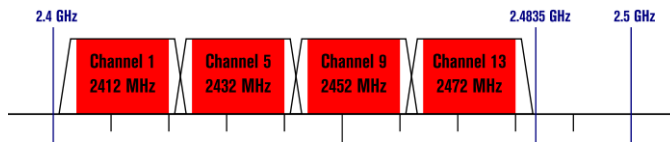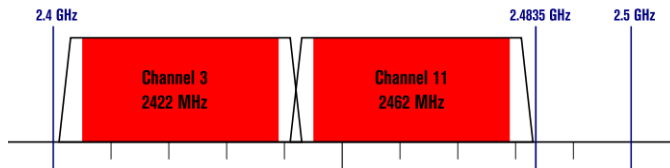
(a)
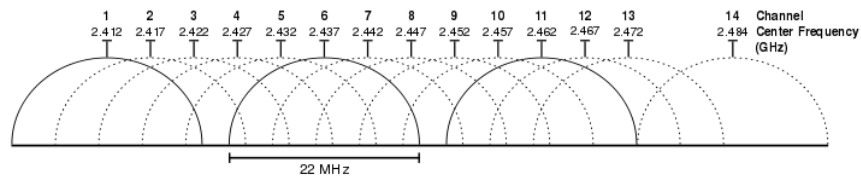
(b)

Fig. 1-4 Allocated channel for IEEE 802.11 standards.

In Fig. 1-5, we calculated the received power with considering an omnidirectional antenna as the radiating element in access point, and for mobile targets. As it is illustrated in Fig. 1-5, the maximum coverage area is considered to be 50 m. If we imagine that the receiver sensitivity is -80dBm, which means in the worst case we need -80dBm received power at the receiver to have the desired BER in the receiver baseband section. As it is shown in Fig. 1-5, the received power in the receiver for the maximum distance condition in the best scenario (unobstructed line-of-sight (LOS) without any channel fading) is 8dBm lower than sensitivity of the receiver Detecting such a signal will cause a huge amount for BER in the baseband section.

Omni-Directional Antenna
G_t=Gain=2.5dB

P_t

0dBm

Transmitter

R

$$Power = \frac{P_t G_t}{\frac{4}{3}\pi R^3}$$

For minimum distance (R=10m) ……. -60dBm
For Maximum distance (R=50m) ……. -85dBm

$$Power = \frac{P_t G_t G_r A_r}{\frac{4}{3}\pi R^3}$$

Receiver Gain=15db
Input P1dB=-6dBm

Signal

Receiver Chain

For minimum distance (R=10m) ……. -63dBm
For Maximum distance (R=50m) ……. -88dBm

For minimum distance (R=10m) ……. -48dBm
For Maximum distance (R=50m) ……. -73dBm
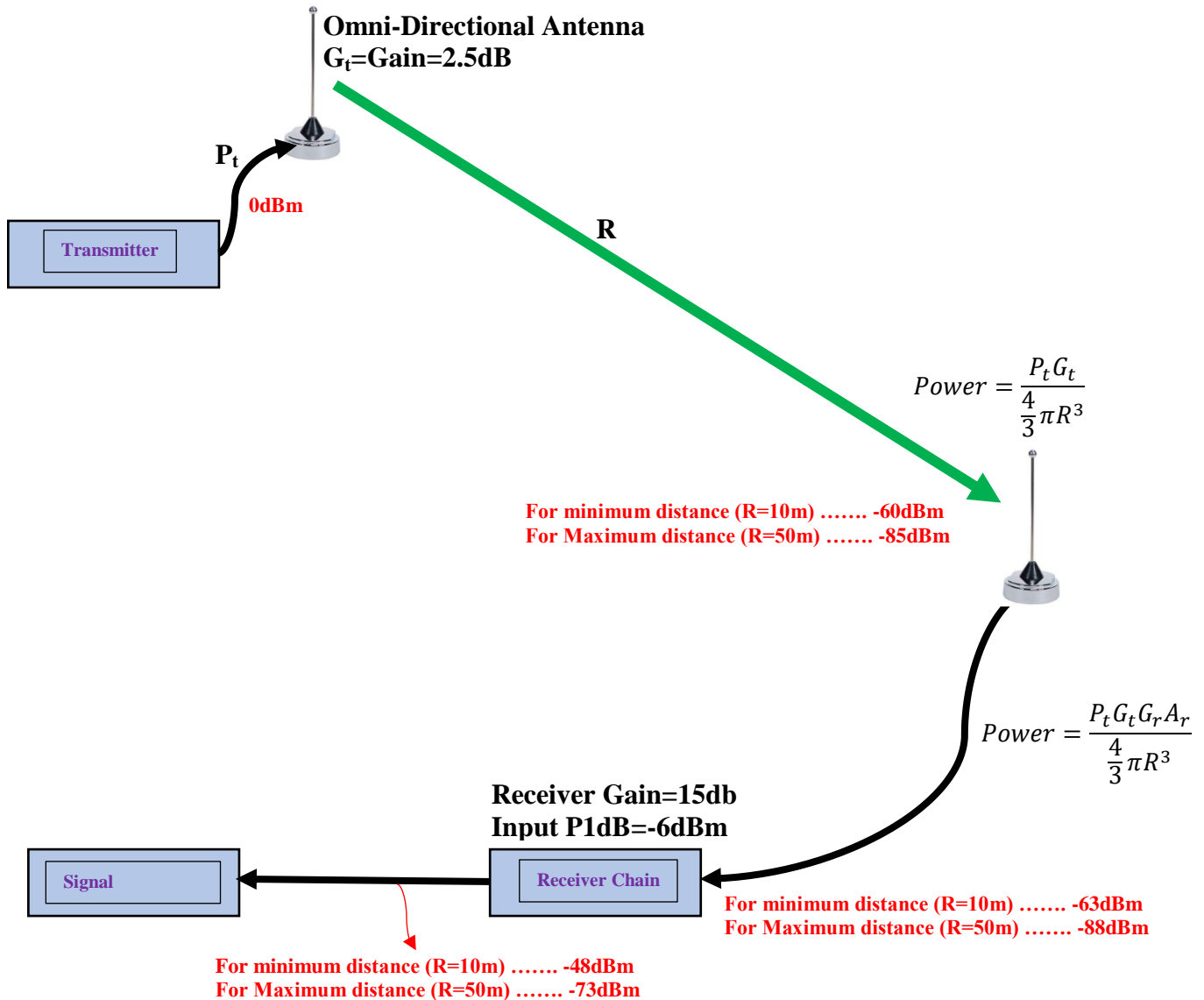
Fig. 1-5 A typical wireless local area network with considering an omnidirectional antenna as the radiating element in access point, and mobile targets.

[20]

If we considered the topology in Fig. 1-6 with a pattern reconfigurable antenna for the access point side, we can improve the link performance in different aspects.

The first thing is that it compensate for the maximum distance condition signal level which is lower than 8dbm below the sensitivity of the receiver. As it is illustrated in Fig. 1-6, the received signal power is higher than sensitivity in the same situation as Fig. 1-5. In this system we should have knowledge about the position of the mobile device to be able to focusing the radiation pattern toward the target; this can be done by searching the space by the pattern reconfigurable antenna and reading the received power level at different directions. However, in a more complicated system with more than one user, we need to have a network signal processing protocol for having the best performance for all the users. If the users are in different sectors of the pattern reconfigurable antenna (Fig. 1-7a), we are able to detect them one by one and define their distance and their angle. However, if we have two or more users in one sector (Fig. 1-7b), it is impossible to define their number and their distance. In this situation, we need to read the power after demodulating the different channels; in order to do this, we need to read the power after channel detection. Fig.1-8 shows the proper place for estimating the channel power, and the proper topology for the receiver of a system with a pattern reconfigurable antenna. In this receiver topology, we consider an 8-sector pattern-reconfigurable antenna system.

In this thesis, the structure shown in Fig. 1-7(b) is not deployed since the purpose of this thesis is designing the reconfigurable antenna based on FSS inclusions. In fact, there is no receiver, a digital control unit is designed to verify the performance of the pattern reconfigurable antenna. This can be implemented by RF power estimation for user detection. To implement the aforementioned scenario in Fig. 1-7b, it is crucial to possess a complete receiver to estimate the power of different users.

Omni-Directional Antenna
G$_t$=Gain=2.5dB

P$_t$

0dBm

Transmitter

R

$$Power = \frac{P_t G_t}{\frac{4}{3}\pi R^3}$$

For minimum distance (R=10m) ……. -60dBm
For Maximum distance (R=50m) ……. -85dBm

$$Power = \frac{P_t G_t G_r A_r}{\frac{4}{3}\pi R^3}$$

Receiver Gain=15db
Input P1dB=-6dBm

Signal

Receiver Chain

For minimum distance (R=10m) ……. -53dBm
For Maximum distance (R=50m) ……. -78dBm

For minimum distance (R=10m) ……. -48dBm
For Maximum distance (R=50m) ……. -73dBm
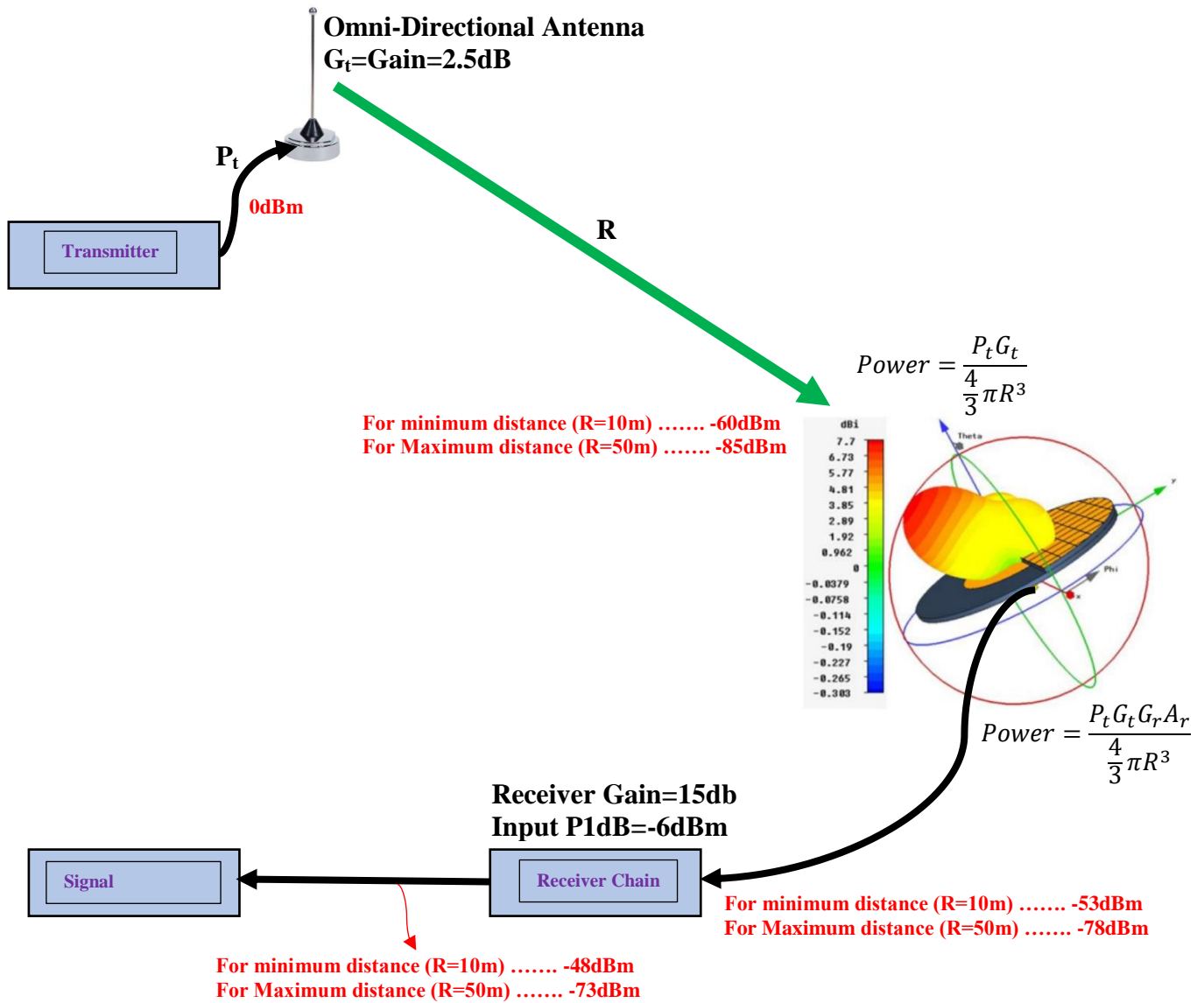
Fig. 1-6 A typical wireless local area network with considering a pattern reconfigurable antenna as the radiating element in access point, and an omnidirectional antenna for mobile targets.
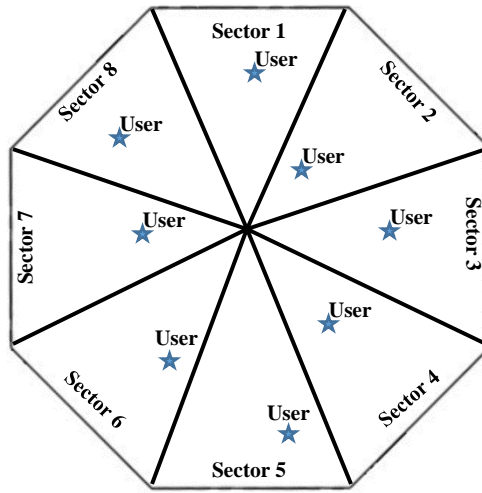
(a)
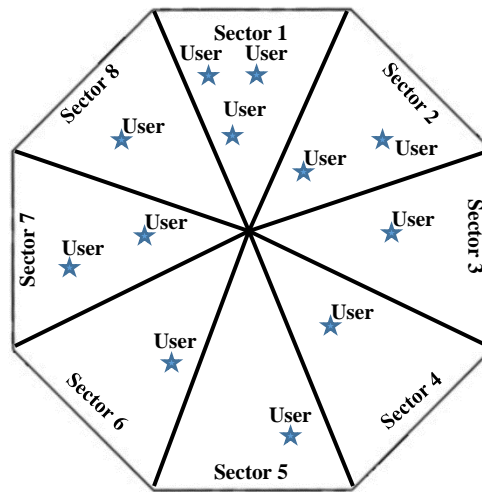
(b)

Fig. 1-7 Different users' locations scenario. a) Location detectable using RF power estimate. b) Location detectable using channel power estimate.

Signal Processing Layer

RF Power Amplifier

RF Mixer

Power Harmonic

Baseband Signal

4-Line SPI
Protocol

SPDT

Sensitizer

SPDT

SMA Connector

IF Channel Select Filter   IF Amplifier   LN   RF Band Select Filter

Baseband Signal

RF Mixer

Power Level

**Channel Power
Estimation**

Antenna Plane 1 Driver

Antenna Plane 2 Driver

Connector

Antenna Plane 3 Driver

Antenna Plane 4 Driver

Antenna Plane 5 Driver

Antenna Plane 6 Driver

Antenna Plane 7 Driver

Antenna Plane 6 Driver

Fig. 1-8 The proper topology for the receiver of a system with a pattern reconfigurable antenna.

1. 4 Thesis executive summary and accomplishments

To accomplish the aforementioned approaches, a literature review about reconfigurable antennas is investigated in Chapter 2. In fact, the radiation beam of the reconfigurable antenna is discussed and its effect on the link budget will be presented. In Chapter 3, more details about the reconfigurable antennas based on active FSS cells is presented. In Chapter 4, the control unit is designed and discussed to develop an electronically reconfigurable radiation beam antenna.

Chapter 2 Literature Review on Pattern-Reconfigurable Antennas

2.1 Introduction

Wireless communication systems are extending toward multi-task environments for different applications. This multi objective prepares the users to be linked to various services and connections with variety of services at different time slots. It is evident that a lot of antennas are integrated into aircrafts or other vehicles; it is therefore appropriate to provide a single antenna element which has different functionalities to be placed in small area for different applications. A radiating element which has this capability to change its properties, such as the resonant frequency, polarization or radiation beam, can be considered as a reconfigurable antenna. A reconfigurable antenna has this ability to provide additional characteristics and degree of freedom to wireless communications and users to improve the link quality and enhance the performance of the systems. The main objective of reconfigurable antenna is to reduce the number of elements for specific applications; however, it can be applied for sophisticated applications such as phased array systems as well as MIMO systems. Additionally, the reconfigurability in terms of radiation pattern is the alternative approach as opposed to phased array and adaptive array systems. A reconfigurable Antenna gives us this permission to allocate the desired spectrum in multi-band wireless communication systems. Also, it brings about a minimum number of antenna element, most importantly, it reduces the dimension of the antenna. There are different techniques to implement a reconfigurablity in terms of radiation pattern, such as using tunable elements in the feeding networks, employing phase shifters and tunable filters, tunable elements embedded such as PIN diodes, MEMS (switches, varactors, and moveable parts) and optical switching in the radiating elements, mechanically moveable radiating elements.

2. 2 Reconfigurable Antenna Base on Active Bowtie FSS

The configuration of the antenna element presented in [17] is a hexagonal cylinder and is comprised of two major parts [17]. The antenna element is dipole and is located in the middle of the structure. In fact, the antenna element acts as an excitation source and the remaining parts are frequency selective surface inclusions. To create FSS unit cell, a bow-tie shape is deployed and its constituted parameters was calculated. When the diode is switched on, the FSS unit cell acts in the transmission mode, and when the diode is switched off, the FSS lattices work in reflection

state, which has different characteristic compared to conventional ones. The proposed structure consists of 3 sidewalls operating in transmission mode and 3 sidewalls working in reflection mode, where it acts as a reflector. The measurement results reveal that the radiation beam can be steered in six steps along the entire azimuth plane with average gain of 5dBi where the beamwidth corresponds to 80° at 2.5GHz. Thus, these simple and low cost structures propose an excellent candidate for wireless communication systems and low power base station systems.

In fact, the proposed inclusion is comprised of a bow-tie lattice with a length of L=110 mm and a width of W=46 mm. A PIN diode is integrated in the middle of bow-tie cell shown in Fig.2-1 to change the state from transmission to reflection. The magnitude of the S11 for the proposed unit cell when it is working in the transmission and reflection mode was achieved and shown in Fig.2-2.

There is a bi-cone dipole located at the center of the hexagonal cylinder as an excitation source as shown in Fig. 2-3. The operation of this reconfigurable antenna can be described as follows. In fact, when the pin diode is switched on, the FSS unit cell works in the transmission mode for the incident electromagnetic wave; when the diode is switched off, the FSS inclusion acts as a reflector which reflects all of the incident waves. Thus, the FSS cells with off states of the hexagonal cylinder can reflect the incident electromagnetic wave to form a directional radiation pattern. By sequentially switching the states of the PIN diodes, this beam-switching antenna is able to steer the radiation pattern along the azimuth plane. The measured reflection coefficient in terms of different bias configurations is shown in Fig. 2-4. The measured radiation pattern of the antenna, when 3 sidewalls are switched on at 2.5 GHz, is shown in Fig.2.5.
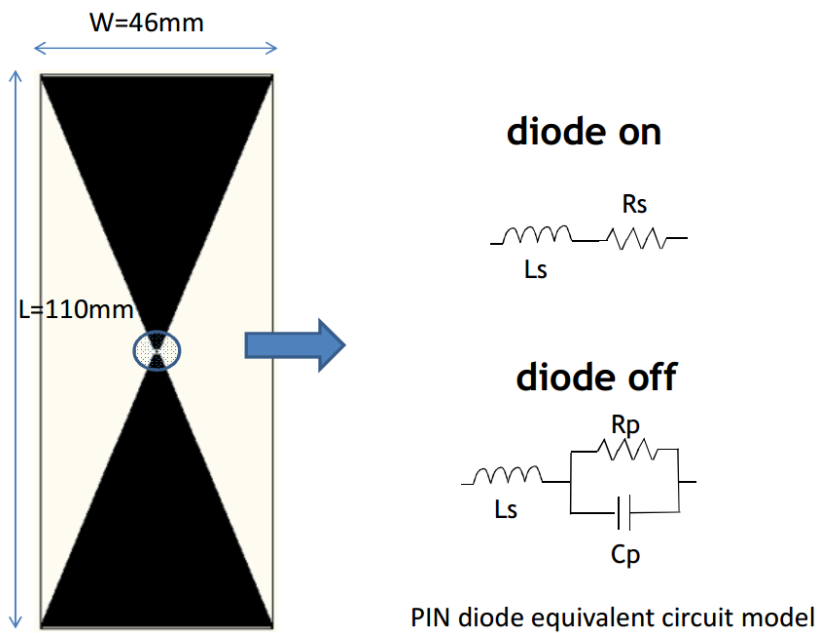
Fig. 2-1 Unit cell and the equivalent circuit model of PIN diode [17].
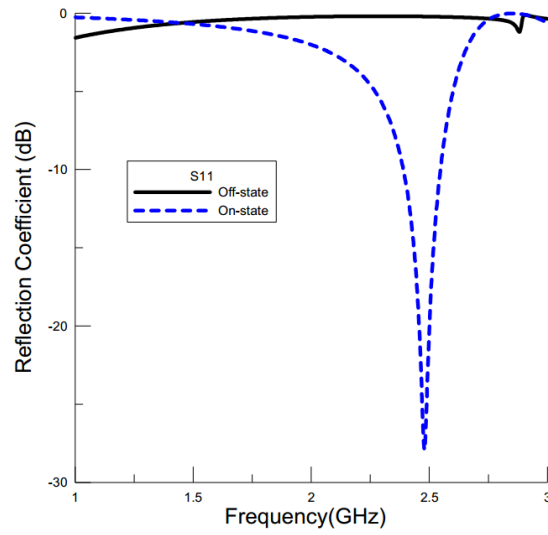
Fig. 2-2 Reflection coefficients of both diode turn-on and turn-off state [17].
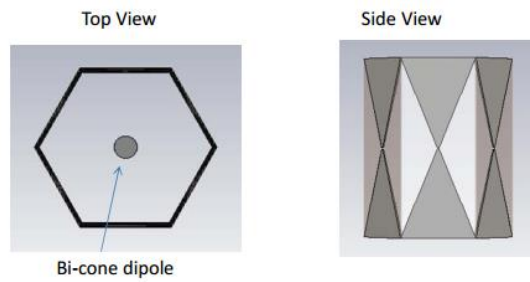
Fig. 2-3 Reflection coefficients of both diode turn-on and turn-off state [17].
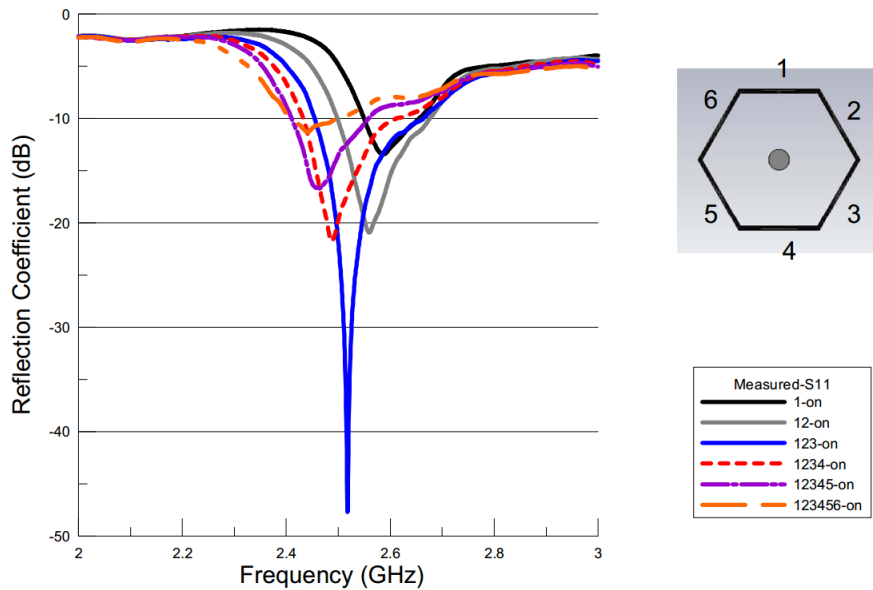
Fig. 2-4 Measurement results of the reflection coefficient against the number of turn-on sidewalls [17].
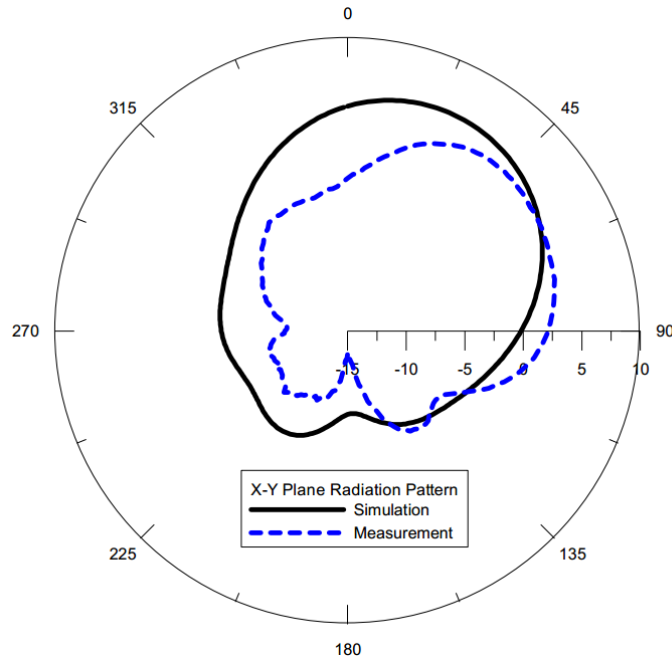
Fig. 2-5 Simulation result of X-Y plane 2D radiation pattern [17].

2. 3 Reconfigurable Antenna Based on Reconfigurable FSS

The active FSS is comprised of the number of unit cells that permit to switch the radiation pattern of the antenna into a desired direction. The approach consists of an active cylindrical FSS structure which contains a number of PIN diodes and is comprised of 10 equal columns. Then, in the middle of the array of FSS walls, a classical dipole antenna is embedded. The radiated beam of the antenna is steered by turning on and off of the PIN diodes. The measured antenna gain working at 1.8 GHz corresponds to 9.1 dBi which covers all azimuth angles in 10 steps. This structure is an excellent candidate for base station applications [18].

This FSS inclusion shown in Fig.2.6 consists of two elements: an array of circle loops along with a discontinuous strip. To achieve reconfigurability in terms of transmission coefficient of the FSS unit cell, a PIN diode is integrated in the middle of the rectangular strip. The result of the proposed FSS lattice in terms of transmission and reflection coefficient is revealed in Fig. 2-6.

The configuration of proposed FSS flexible surface which forms of the cylinder is located in the surrounding of dipole as shown in Fig.2-7. The active FSS structure is comprised of 10 columns, where each panel includes three FSS scatters. In the top of each FSS panel, an RF-choke as well as a resistor is attached to the whole FSS unit cell, and the RF-choke is attached in the below of FSS cells. The main objective of RF-chokes is to prevent the effect of direct current feeding on the FSS unit cells. Also, the main role of resistor is to restrict the biasing current of diodes.

To change the radiation pattern of the dipole antenna from omnidirectional to directional, it is crucial to switch the FSS columns between ON and OFF states. For each angle, the diodes for the specific sector are turned ON whereas the other diodes are switched OFF. In the On state, the EM waves of the dipole propagates into a desired direction while in the off state the FSS unit cells prevent the propagation and reflect all of the radiated signals. The specific sector, which is defined by the size of the aperture of the reflector, can be estimated by the number of columns when the FSS cells are turned ON. As shown in Fig. 2-8, the maximum value of the directivity is achieved when all three columns work in the ON state. The comparison between the simulation and measurement results of the proposed FSS antenna is shown in Fig.2.9.Also, the radiation pattern in both E and H-planes at 1.8 GHz are shown in Fig.2.10.
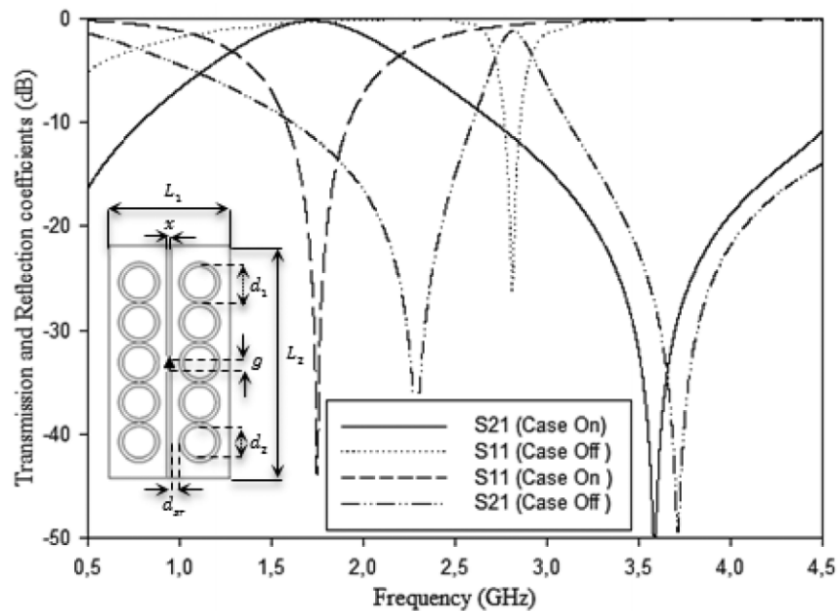
Fig. 2-6 Transmission and reflection responses of the proposed active FSS unit cell [18].
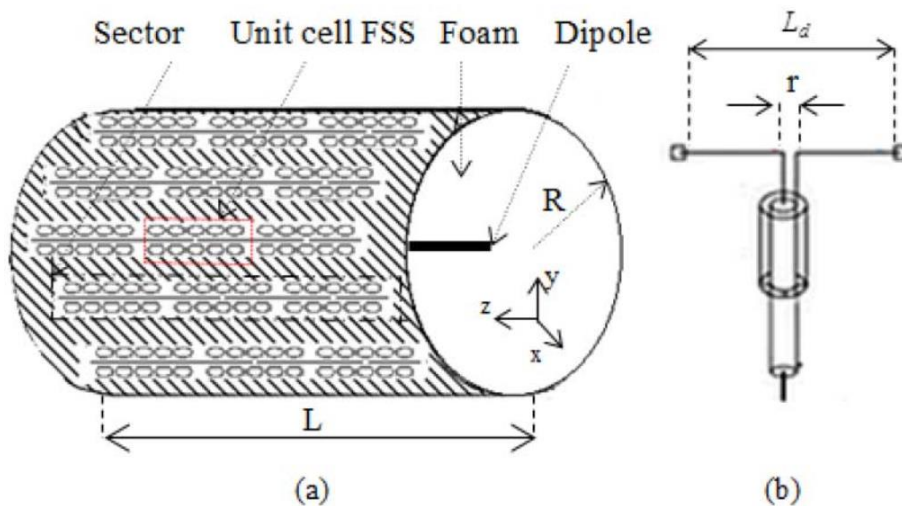
Fig. 2-7 Proposed active FSS antenna. (a) 3-D view. (b) Excitation source [18].
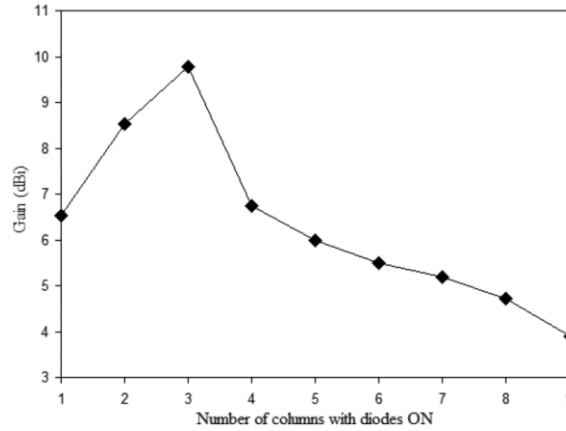
Fig. 2-8 Effect of number of columns (in ON state) on gain of the proposed antenna [18].
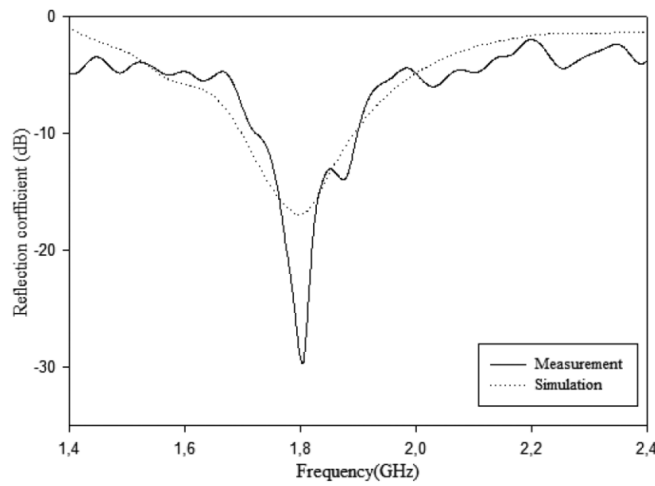
Fig. 2-9 Reflection coefficient of the cylindrical active FSS [18].
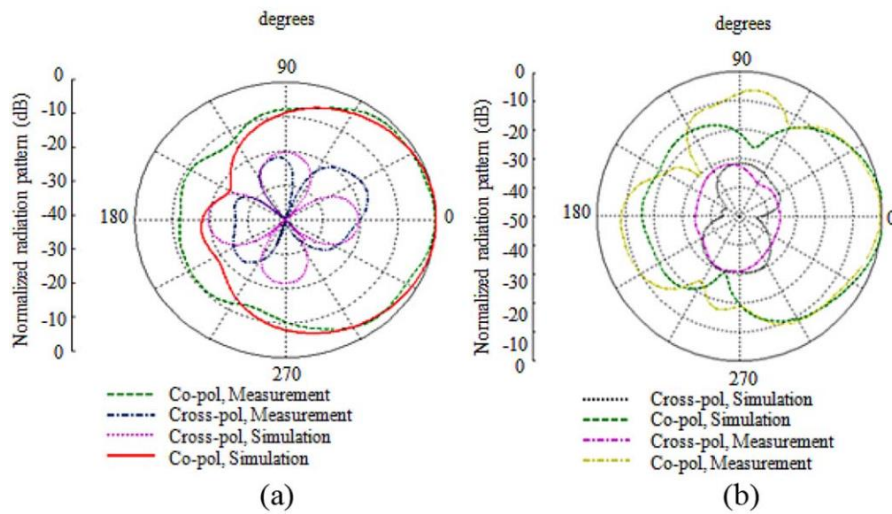
Fig. 2-10 Measurement and simulation radiation pattern of the proposed antenna in the directional mode: (a) H-plane; (b) E-plane [18].

2. 4 Beam Steering with Integrated Ferroelectric Varactors

The main objective of FSS is to act as a transmitarray with a bandpass property in Ku-band [19]. The FSS scatters consist of a capacitive and inductive element which generate a bandpass for the illuminated waves. By changing the capacitive value of the FSS cells on a screen-printed barium strontium-titanate (BST) thick-film ceramic, its operating frequency is altered. Thus, this technique proposes a low-cost and simple approach suitable for incorporating varactor diodes into the FSS cell. A fabricated structure of FSS unit cell consists of two capacitive layers which the total size corresponds to 40 mm x 40 mm. Also, each panel composed of a maximum number of 1600 integrated BST varactors that are fabricated by deploying a chemical as well as metallization process. An illuminated waves passing through the FSS wall will cause a phase shift, which can be tuned by tuning the passband. This cause the transmitted waves deflect to a predefined angle by employing a gradient phase over the FSS unit cell. In fact, a 360 degree phase shift is achieved by creating a multilayer FSS panel. The fabricated FSS panel proves its application for steering the illuminated wave into a pre-defined direction.

Fig. 2-11 reveals the methodology of a transmitarray for steering the radiated beam, where includes two antennas in the receiver and transmitter, respectively as well as a beam forming network between them. The aforementioned FSS scatter is comprised of three layers. In fact, a thin layer is deployed to realize the tuning of capacitors. In the light of the periodicity of the FSS cells which are repeated in each direction, a single cell with defined boundary conditions is taken into account.

Fig. 2-13. demonstrates the schematic of the capacitive layer of FSS cells with 20 bias channels provided for fabrication. On the right side, each second row is attached to an individual bias pad, and on the left, all other rows are dc grounded. Fig. 2-14 shows the measured radiation patterns of the FSS in three tuning states.
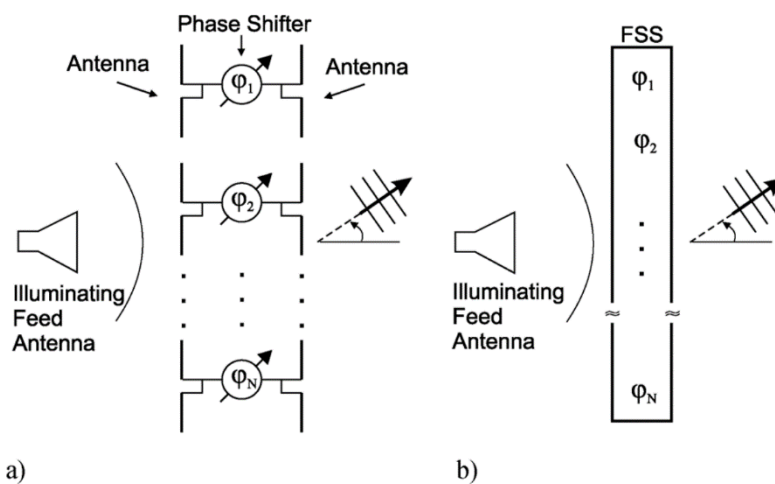
Fig. 2-11 a) The concept of a transmitarray for beam steering, which consists of two antenna arrays for receiving and transmitting, respectively, and a beam forming network between them. b) A tunable FSS with phase shifting capability, which can control the beam [19]
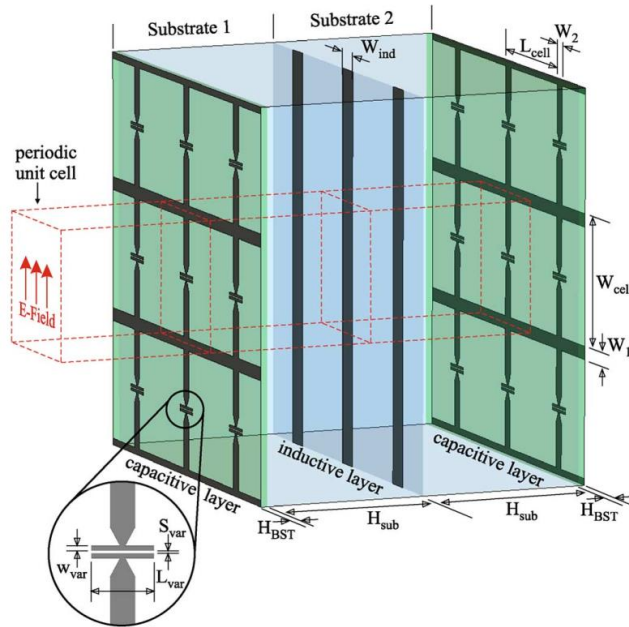
Fig. 2-12 a) Proposed FSS consists of 3 metallization layer on two substrates. Thin BST layer are implemented for tuning the capacitors. Due to the periodicity, a single unit-cell with periodic boundaries is considered in simulations[19].
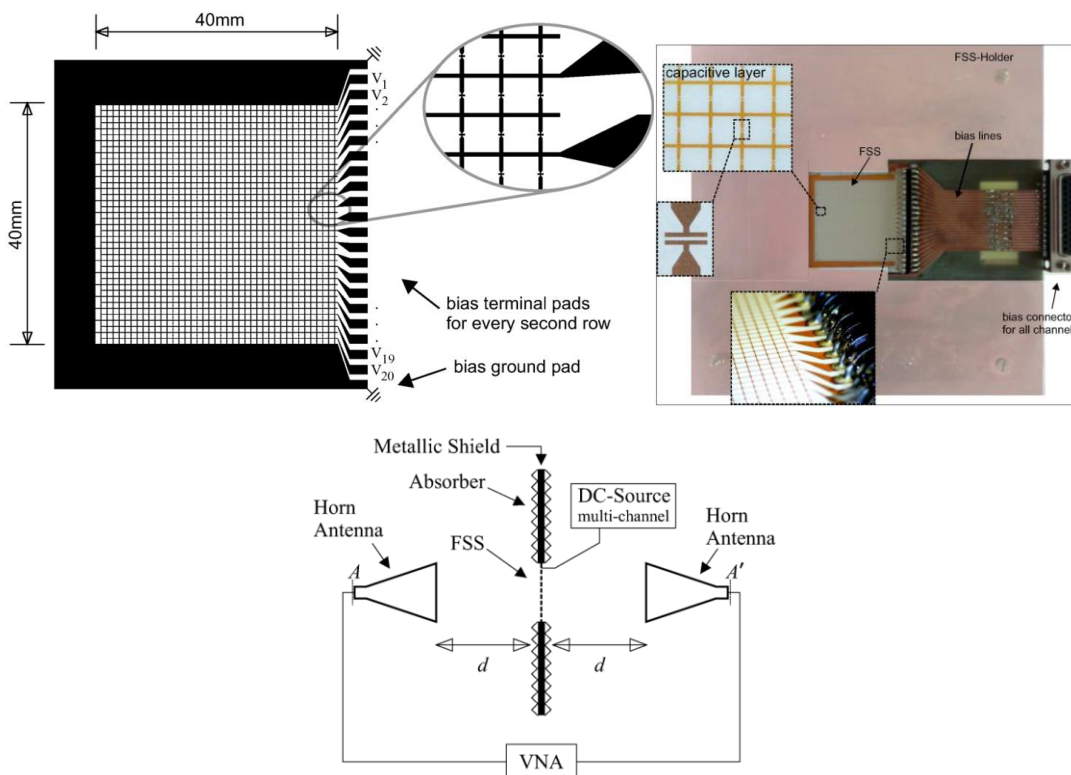
Fig. 2-13 The layout of the capacitive layer of FSS with 20 bias channels prepared for prototyping. On the right side, every second row is connected to an individual bias pad, and on the left, all other rows are dc grounded [19].
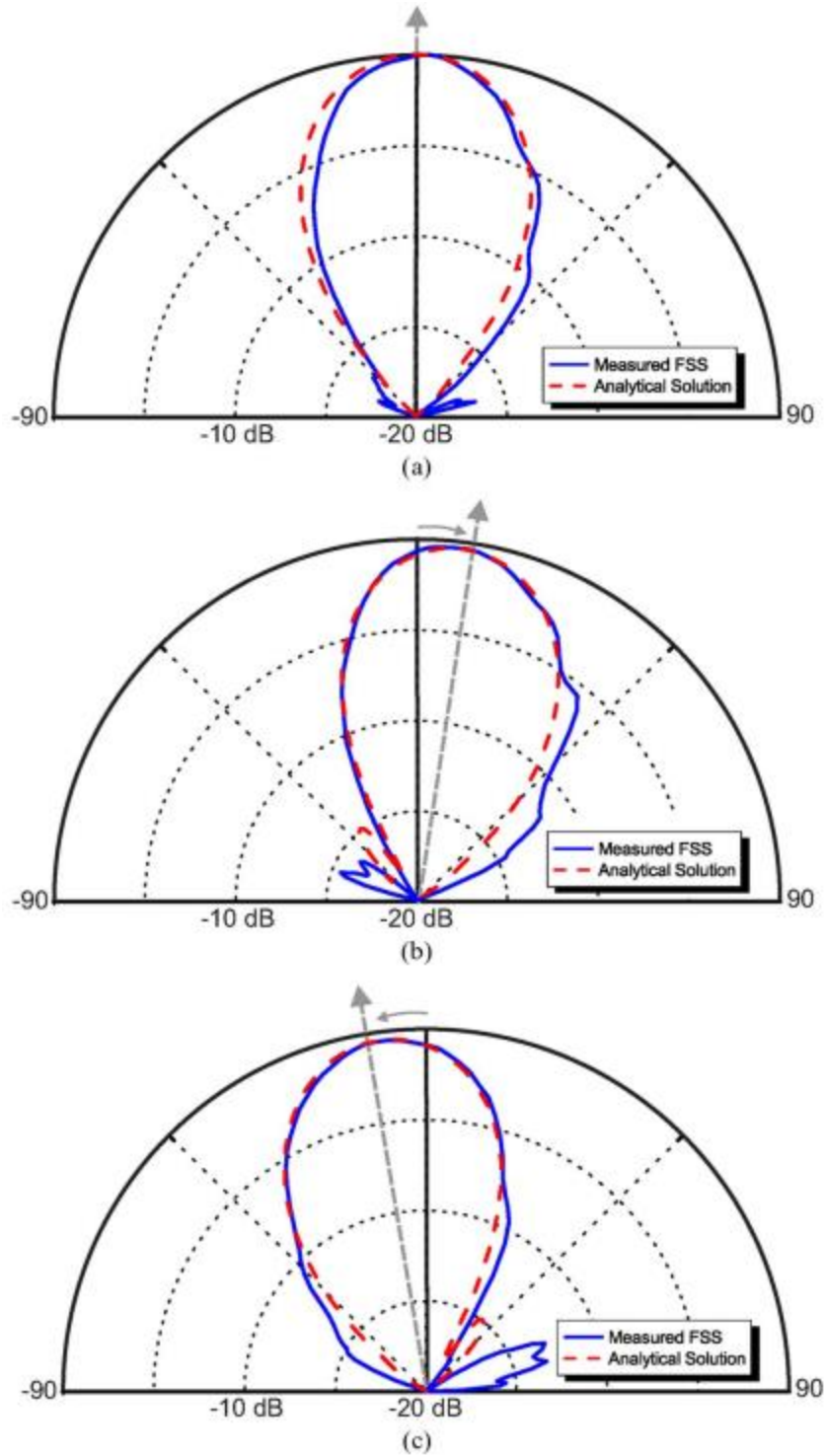
Fig. 2-14 Measured radiation patterns of the FSS in three tuning states. All curves are normalized to the maximum power in the untuned case. The radiation angle is steered between . The results are fitted with an analytical model. (a) Untuned state; (b) voltage[19]

2. 5 High-Gain Reconfigurable Sectoral Antenna

The FSS unit cell composed of metallic scatters with PIN diodes in each cell, and it is embedded cylindrically in the surrounding of the dipole antenna which has an omnidirectional radiation pattern [20]. The FSS configuration is composed of two semi-cylinders. By changing the state of each column and switching the PIN diode on or off, a radiated beam of the antenna can be steered into a predefined angle. The impact of the each pin diode as well as the radius of the cylindrical structure is carefully investigated to achieve the best directive radiation pattern in desired direction. In addition, an approach to enhance the reflection coefficient of the dipole antenna is also presented. A prototype of the dipole antenna along with FSS cells is fabricated and the measurement results indicate that the beamwidth in the azimuth and elevation planes at 2.1 GHz corresponds to 20 and 70 degree with a maximum realized gain of 13 dBi. Thus, this structure is an excellent case for outdoor wireless communication system. The above mentioned inclusion proposed in Fig. 2-15(a), is comprised of a metallic lattice where a pin diode is integrated into each strip .Fig. 2-16 reveals the transmission and reflection coefficient of the proposed FSS inclusion when the pin diode is turned on and off. To achieve a high-gain characteristic with reconfigurable radiation pattern, an array of dipole antenna was designed and placed in the middle of FSS panels illustrated in Fig. 2-17(b). In Fig. 2-18 the result of the reconfigurable radiation pattern is shown .
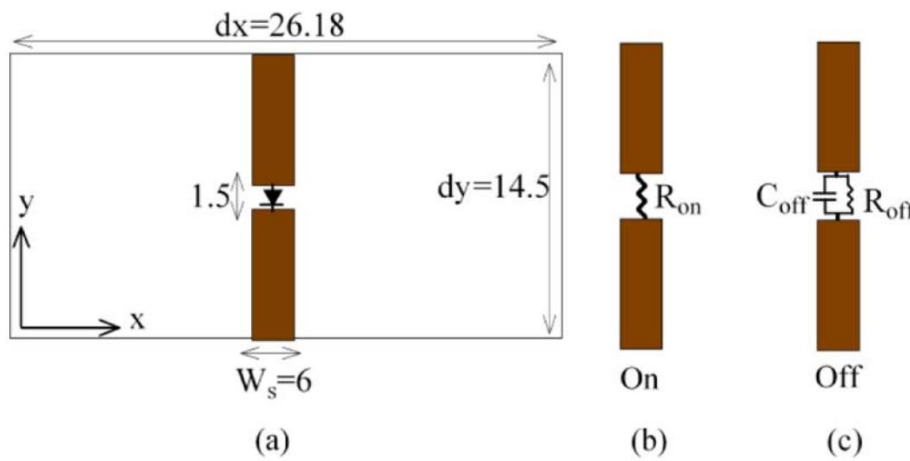
Fig. 2-15 (a) Schematic of the FSS unit cell (all the dimensions are in millimeters), (b) on-state equivalent circuit, (c) off-state equivalent circuit[20].
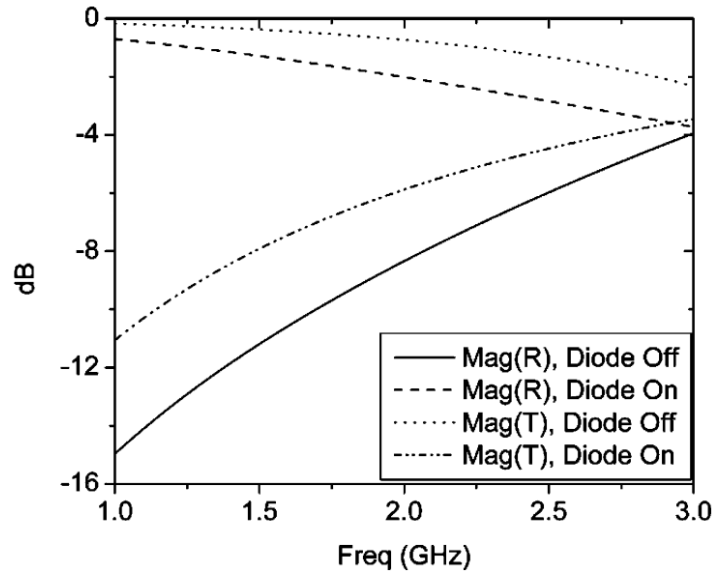
Fig. 2-16 Magnitude of the transmission and reflection coefficients of the FSS unit cell in on- and off-states[20].
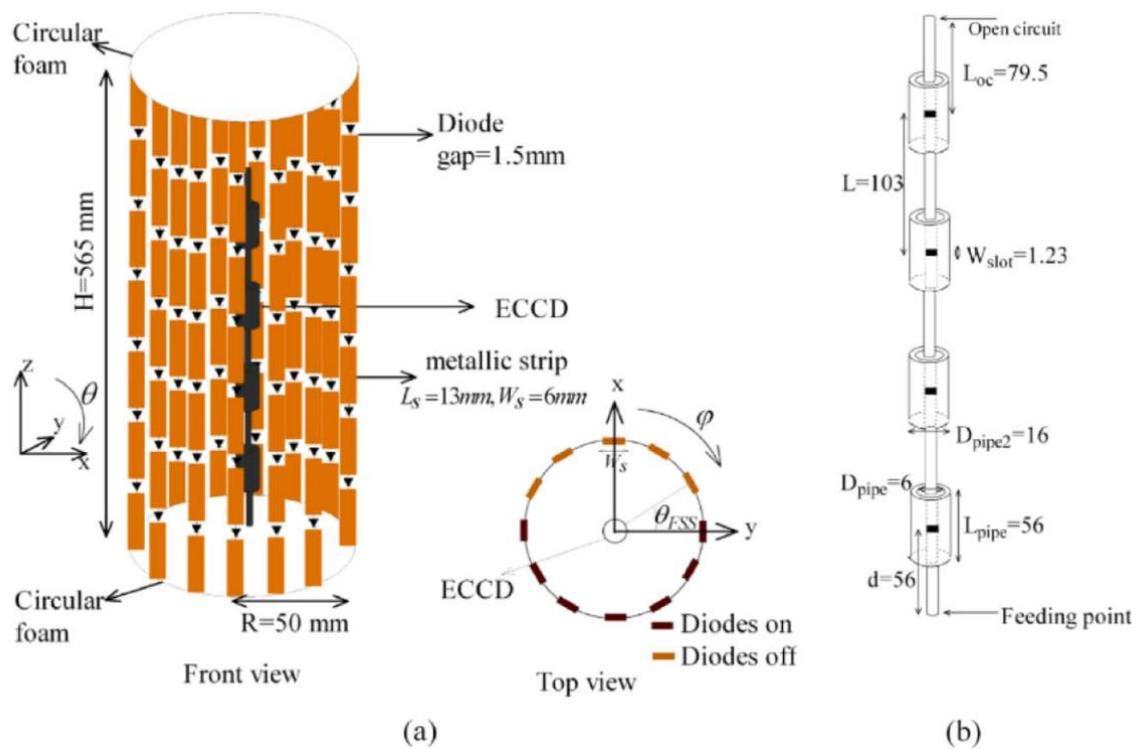
Fig. 2-17 (a) Reconfigurable sectoral FSS antenna, (b) ECCD array antenna (dimensions in mm)[20].
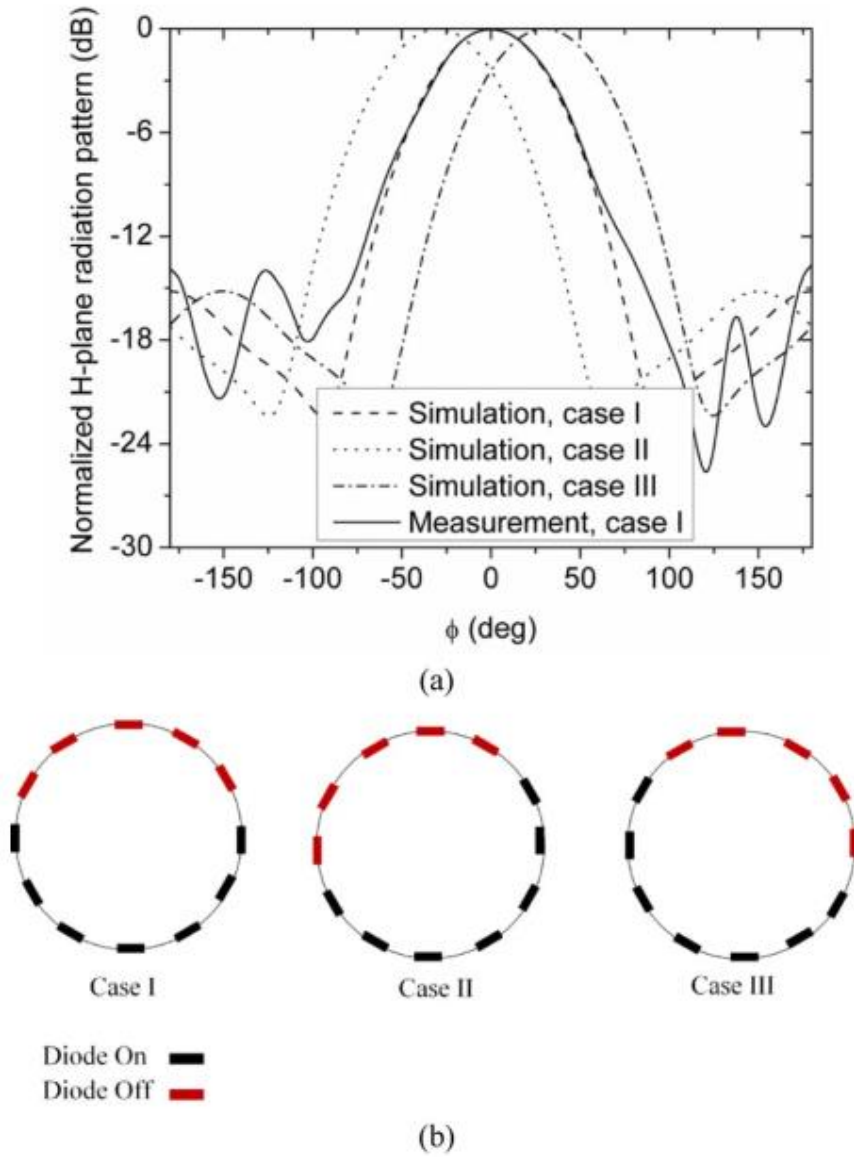
Fig. 2-18 Antenna reconfigurability, (a) H-plane radiation pattern, (b) diode state configuration [20].

2. 6 Agile Radiation-Pattern Antenna

The design of smart antenna working at 2.45 GHz is presented by deploring FSS scatters integrated by pin diode. In fact, by operating the FSS unit cell in two modes of transmission and reflection the illuminated waves by dipole can be manipulated for achieving a reconfigurable radiation pattern in the azimuthal plane. The cylindrical FSS unit cell located around the antenna can sweep the radiation beam in azimuth plane. The measurement results indicate that the sweeping the beam can be implemented. The impedance matching of the antenna corresponds to 200 MHz. Also, the back lobe radiation of the antenna is equal to 13 dB at 2.55 GHz. The measured and simulated reflection coefficient of the proposed FSS antenna is shown in Fig.2.19. It proves that the matching of the antenna is around 200 MHz. Fig. 2-20 demonstrates the 3D configuration of the Antenna structure with FSS. This antenna is comprised of an active cylindrical frequency selective surface (ACFSS) illuminated by a classical dipole located at its center. To prove the aforementioned concept, the antenna radiation pattern was measured at different frequencies over the operating bandwidth of dipole antenna. It can be observed in Fig.2-21 that the best operation of the antenna occurs at the frequency of 2.55 GHz, whereas the magnitude of reflection coefficient corresponds to 10 dB. There is a good agreement between simulation and measured ones. The radiation pattern is directive and the back-lobe level is more than 13 dB. The discrepancy between the simulation and measured results is attributed to the RF-cable effect, feed-line loading on the EM response of the FSS screen, as well as fabrication tolerances.
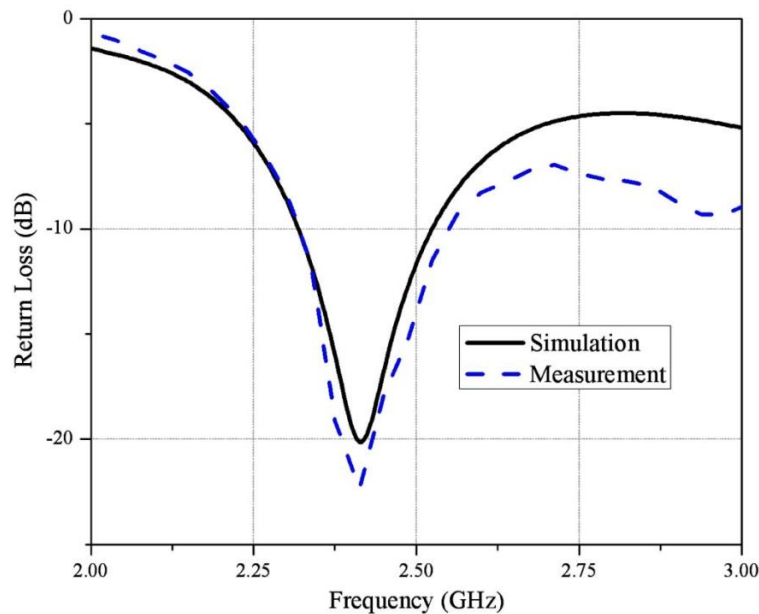
Fig. 2-19 Measured and simulated return loss[21].
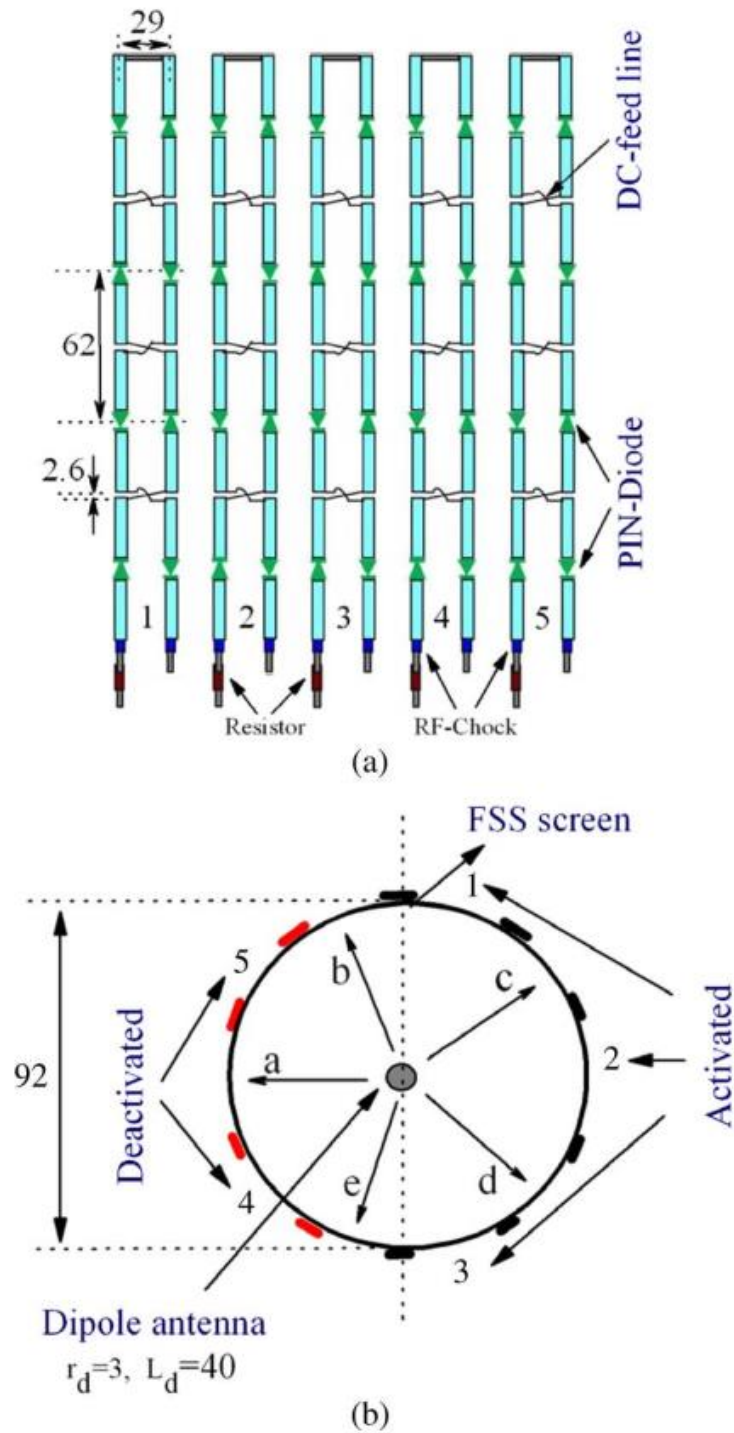
Fig. 2-20 Proposed antenna configuration (all dimensions are in mm). (a) Distributed configuration of the proposed FSS screen. (b) Cross section of the proposed ACFSS [21].
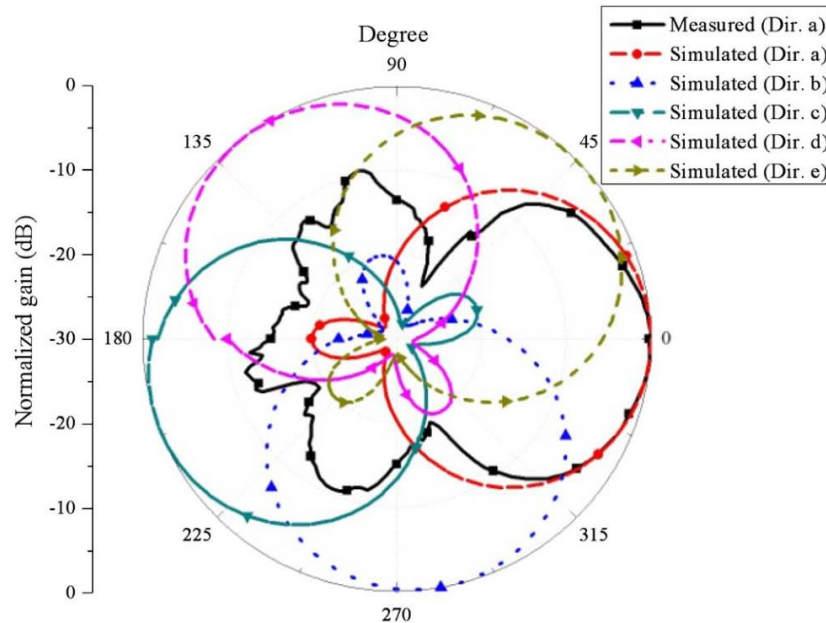
Fig. 2-21 Measured (2.55 GHz) and simulated (2.45 GHz) H-plane radiation patterns [21].

2. 7 Dual-Band Beam-Sweeping Antenna Based on Active Frequency Selective Surfaces

This antenna is composed of a dual-band omnidirectional monopole antenna operating at 2.45 GHz and 5.2 GHz and two cylindrical AFSS screens [22]. The dual-band omnidirectional monopole antenna is designed as a radiating source and surrounded by the proposed two cylindrical AFSS screens. The unit-cells of the two proposed AFSS screens consist of two metallic crosses connected by a pin-diode vertically. By switching the pin-diodes, the transmission and reflection characteristics of unit-cell of the two AFSS are investigated, respectively, at their own operating frequency. This leads to the variation of the radiation pattern when the cylindrical AFSS screens are loaded around the monopole antenna. Therefore, by switching the pin-diodes with specified combinations, the dual-band beamforming antenna with multiple discrete states can be achieved at 2.45 GHz and 5.2 GHz.

The geometry of the proposed AFSS unit-cells operated at 2.45 GHz and 5.2 GHz are shown in Fig. 2-22. Each AFSS unit-cell contains two metallic crosses connected by a pin-diode in serial. Fig. 2-23(a) shows the simulated transmission coefficients of the 2.45 GHz AFSS unit-cell in both ON and OFF states, and Fig. 2-23(b), showing that electromagnetic waves are reflected and transmitted by the AFSS unit-cell at 5.2 GHz when the diode is ON and OFF.

The proposed dual-band beam-sweeping antenna schematic is shown in Fig. 2-24. A dual-band monopole antenna in the center is designed as a radiating source and surrounded by two proposed cylindrical AFSS screens that have a common center. The operation mechanism of the

dual-band beam-sweeping antenna is stated as follows. For the outer cylindrical AFSS screen, it is divided into six parts. In each step of operation, three adjacent pin-diodes in three AFSS unit-cells are ON and the others are OFF. The AFSS unit-cells with OFF-state diodes have a high transmission coefficient and almost transparent for incident electromagnetic waves radiated from the monopole antenna at the center and the other parts with ON-state pin-diodes provide a high reflection coefficient acting as a metallic reflector. This means three parts are open and the other three parts are closed to the propagation of electromagnetic waves. Therefore, the omnidirectional radiation pattern of the monopole antenna is converted into a directional one. The inner cylindrical AFSS screen works in the same operating method. The outer and inner cylindrical AFSS screens can work independently when they are placed in one antenna system. Therefore, by switching pin-diodes in different AFSS screens between the ON and OFF states, the radiation pattern could scan the entire azimuth plane by six steps at 2.45 GHz and 5.2 GHz at the same time. Different scenarios are defined in Fig.2-25 for testing the proposed antenna. Fig. 2-26 shows the measured radiation pattern results in the azimuth plane of Case I.
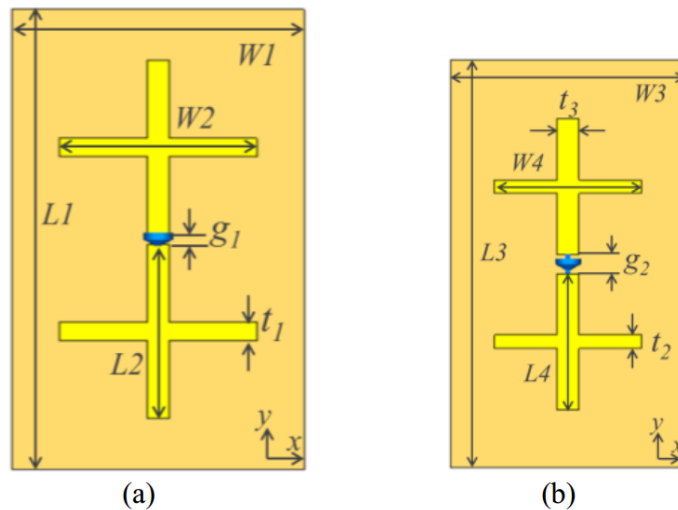
Fig. 2-22 Geometry of AFSS unit-cells: (a) 2.45 GHz AFSS unit-cell, (b) 5.2 GHz AFSS unit-cell [22].
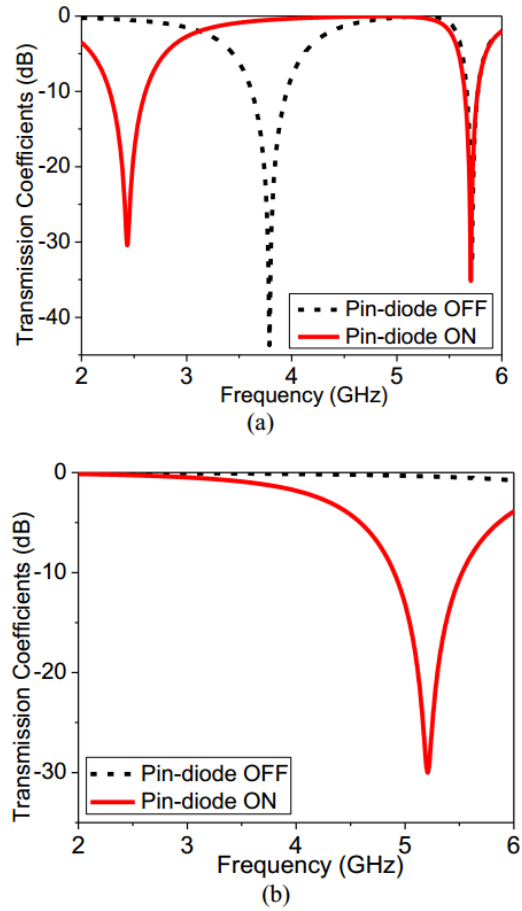
Fig. 2-23 Simulated transmission coefficients of the AFSS unit-cells: (a) 2.45 GHz AFSS unit-cell, (b) 5.2 GHz AFSS unit-cell [22]
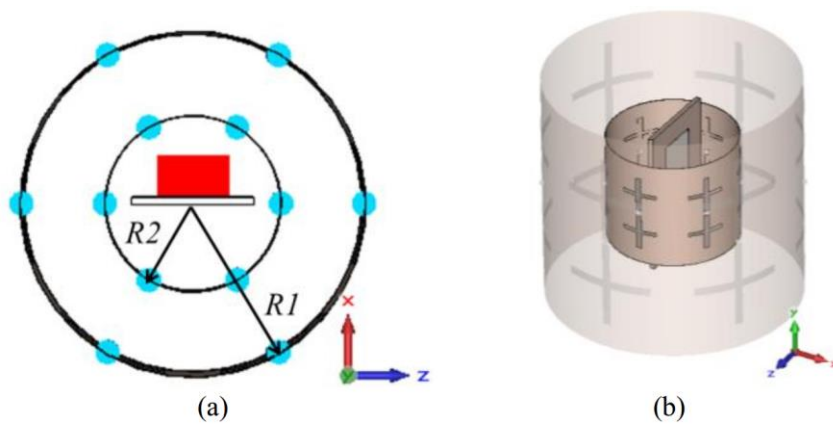
Fig. 2-24 Proposed dual-band beam-sweeping antenna structure: (a) top view, (b) side view [22]
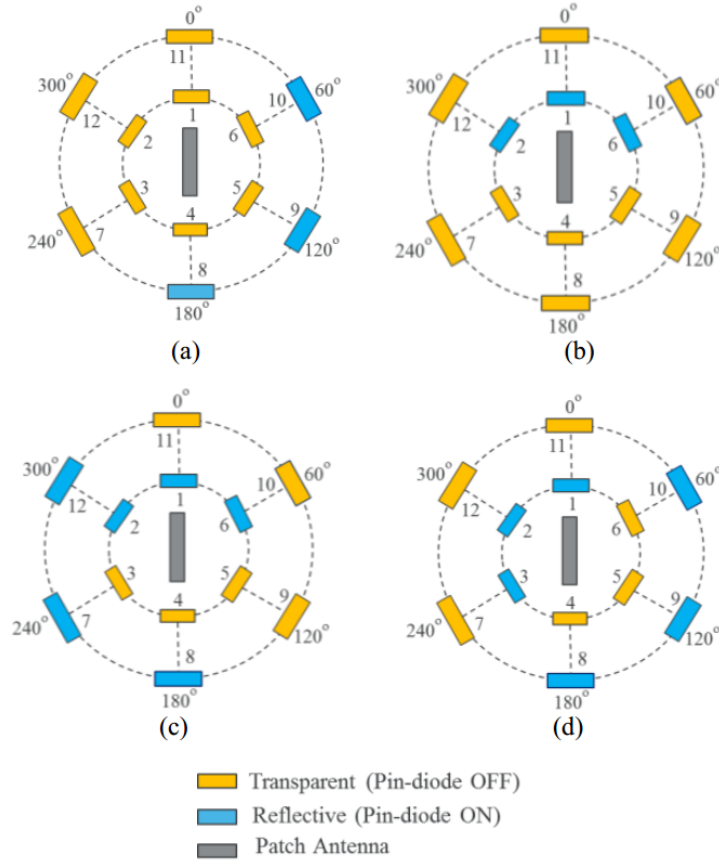
Fig. 2-25 Operation methods: (a) Case I, (b) Case II, (c) and (d) Case III [21]
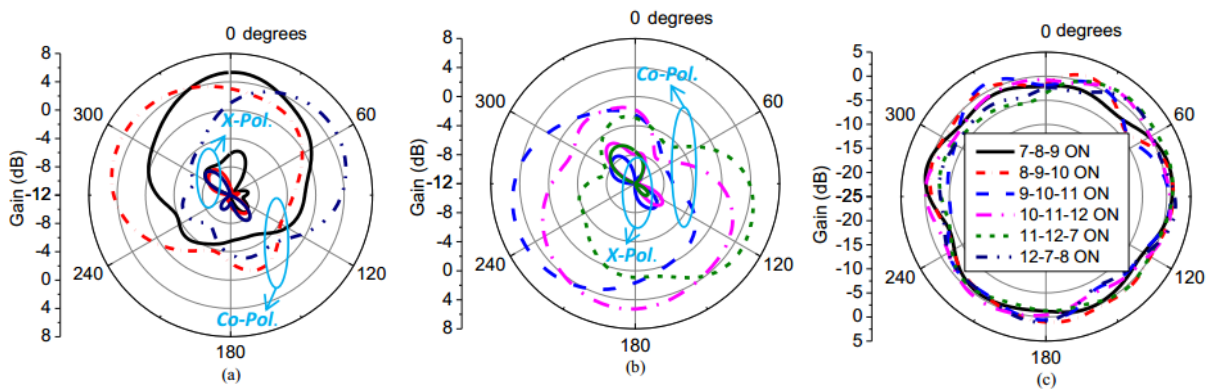
Fig. 2-26 Measured radiation patterns results in the azimuth plane of case I: (a) and (b) 2.45 GHz, (c) 5.2 GHz [22]

2. 8 Conclusion

The research survey on the topic of reconfigurable antenna demonstrates that still this topic is in the developing period and more multi-disciplinary research considering both hardware and software levels of the antenna system are demanded. Integrating reconfiguration mechanism into the antenna structure is one of the challenging topics in this area to alleviate or eliminate the undesired effect of the applied reconfiguration mechanism. Serving new technologies to propose more versatile reconfigurable structures is another attractive research area in this topic. Furthermore, introducing a smart element as components of an adaptive array antenna can also be an ultimate challenging configuration for the future modern smart communication systems.

Chapter 3 Design of Pattern Reconfigurable Antenna Based on Active Frequency Selective Surface

3. 1 Introduction

In this chapter, the basic principles of transmission line theory of inductive and capacitive walls will be investigated and studied in details. These passive-periodic-arrays have been employed to achieve the proposed reconfigurable FSSs wall for controlling the incident electromagnetic waves for designing the proposed pattern-reconfigurable antenna at 2.45 GHz. This is achieved by reconfiguring the equivalent impedance of the screen seen by the incident plane waves from an inductive operation to a capacitive operation. An 8 panel antenna is selected to be designed with the proposed technique at 2.5 GHz. In the section 3.2, we will present and design the proposed active frequency selective with all the details. In Section 3.3, an omnidirectional antenna will be designed and discussed as a base antenna for embedding in the proposed pattern reconfigurable antenna. In Section 3.4, the complete pattern reconfigured antenna will be designed and simulated with all details. Finally in Section 3.5, the measured results will be presented and compared with the simulation ones.

3. 2 Proposed Active Frequency Selective Surface Wall

Fig. 3-1 shows a wire-strip as an active FSS wall. The S-parameters are shown in Fig. 3-1. A unit cell of this FSS consists of discontinuous capacitive-loaded dipole integrated with a surface mount PIN diode. By changing the PIN diode state, a reconfigurable stop-band response is achieved around 2.45 GHz. However, as it is shown in Fig. 3-1, when the diode in the unit cell is in active state, the FSS is not completely transparent for the incident vertically-polarized waves. This considerably deteriorates the desired directive radiation pattern of the proposed pattern-reconfigurable antenna. Therefore, the transmission characteristic of the FSS should be improved when it is going to be used in the transient state (i.e., for example in the case which all diodes are in active mode). We have studied the reason for this phenomenon. The first and straight forward solution is reducing the strip width up to a value limited by practical limitations which will somehow reduce this problem. However, the transmission characteristic still needs to be more enhanced. By studying the subject more deeply, we founded that this imperfect transition mode behavior is due to that the incident wave will see the FSS wall as a medium with different

constitutive parameters. For solving this problem, we tried to design the proposed active FSS unit cell as a magneto-dielectric substrate. The proposed magneto-dielectric substrate increases the constitutive parameters of the host substrate. Magneto-dielectric substrates usually increase the permeability of the substrate. However, if we can design a magneto-dielectric substrate with equal permittivity and permeability, we can improve the active FSS response in transition mode. A magneto-dielectric substrate can be composed of periodic split-ring resonators (SRRs) loop circuits embedded in a low dielectric host medium. This magneto-dielectric substrate can provide equal permittivity and permeability ($\varepsilon_r \cong \mu_r$). The intrinsic impedance of a magneto-dielectric substrate ($\eta = \eta_o \sqrt{\varepsilon_r / \mu_r}$) will be nearly equal to the intrinsic impedance of the free space (η_o) if the value of relative permittivity and relative permeability are equal ($\varepsilon_r / \mu_r \cong 1$). This allows for a large impedance bandwidth because of the improved impedance matching conditions between the two medium. As a result, for improving the transparency of the FSS wall for the incident vertically polarized waves, we embedded a split-ring resonator around the discontinuous strip in discussed active FSS, as illustrated in Fig. 3-2(a).

The constitutive parameters of the new magneto-dielectric FSS unit cell are extracted using the method reported by Shi et al. [22] under the given boundary conditions illustrated in Fig. 3-2(b). As it depicted in Fig. 3-2(b), the bottom xy-plane is the first master boundary, and the top xy-plane is the correspondent slave boundary. Similarly, the yz-planes are the second correspondent master/slave boundaries. The two ports are placed in xz-planes, and the distance between them is 2.5mm, corresponding to a half wavelength in free space at 60 GHz. The Floquet port settings, under the specified boundary conditions (depicted in Fig. 3-2(b)), excite two plane waves with orthogonal electric fields such as TE(0,0) and TM(0,0) modes in the magneto-dielectric FSS unit cell plane. Moreover, higher order modes may also be specified in the port properties. The effective constitutive parameters are extracted and can be considered as the effective constitutive parameters of the whole magneto-dielectric FSS (Fig. 3-3). The frequency response of the magneto-dielectric FSS unit cell depends on the unit cell dimensions. The SRR-like length (L_{s1} and L_{s2}) are the most important parameter that influences the resonance frequency of the magneto-dielectric FSS unit cell; the resonance frequency of the SRR-like resonator decreases by increasing its length (L_{s1} and L_{s2}). As it can be seen in Fig. 3-3, the value of relative permittivity and relative permeability are equal ($\varepsilon_r / \mu_r \cong 1$) at the frequency 2.45 GHz; as a result, the proposed magneto-dielectric FSS is completely transparent for the incident vertically polarized waves. This can be seen in scattering parameters of the proposed magneto-dielectric FSS unit cell (Fig. 3-4).

In each magneto-dielectric FSS unit cell, a surface mount PIN diode is also integrated into the discontinuous dipole strips to reconfigure the electromagnetic response of the magneto-dielectric FSS unit cell. Considering a unit cell of the magneto-dielectric FSS, when the diode is in OFF state, the resonant elements of the magneto-dielectric FSS unit cell give a stop-band to the incident electromagnetic waves with the polarization along the dipole strips. By turning on the diodes, the stop-band will be gone, leading to the desired transmission characteristic at the operating frequency. An equivalent series LC circuit is used to model the OFF state of each PIN diode (GMP4201) in the simulations [20]. It does not have an effective impact on the transmission response of the FSS, the parasitic resistor of each diode can be neglected in the ON

state, and it can be modeled as a perfect conductor in ON state. High frequency PIN-Diodes, in spite of their non-linearity operation, are one of the most popularly used active elements employed to reconfigure the electromagnetic response of an FSS wall. Fig. 3-5(a) shows the employed electrical-circuit model of the GMP4201 PIN-Diode in the simulation [23]. In the ON state bias mode, the diode mainly have a small resistance, which does not have a significant impact on the desired response of the FSS wall. Because of its small value, the series self-inductance of the diode in ON state bias mode has been neglected. However, when it is in OFF state bias mode, the parasitic capacitance has significant impact on the frequency band of the surface in stop-band by effecting the total effective capacitance of the unit cell. Therefore, it is needed to consider its effect in the design of the FSS wall in OFF state bias mode.

In this magneto-dielectric FSS unit cell, the center frequency is mainly indicated by the resonant lengths of the dipole-strips and split-ring resonator discontinuous rings, respectively. The effective length of the dipole in the unit cell is about a half-wavelength at the frequency 2.45 GHz, and it is related to the magneto-dielectric FSS unit cell periodicity and the capacitance parasitic element of the PIN diode in OFF state mode. On the other hand, the average value of the resonant split-ring resonator (SRR) ring is about a wavelength at frequencies around 2.45 GHz. The other dimensions of the unit cell are optimized using the Ansoft HFSS software in terms of the maximum transmission state bandwidth centered at 2.45 GHz and maximum reflection for the ON and OFF states, respectively. The effect of unit-cell dimensions in configuring the radiation pattern of the antenna will be studied in the following subsection.
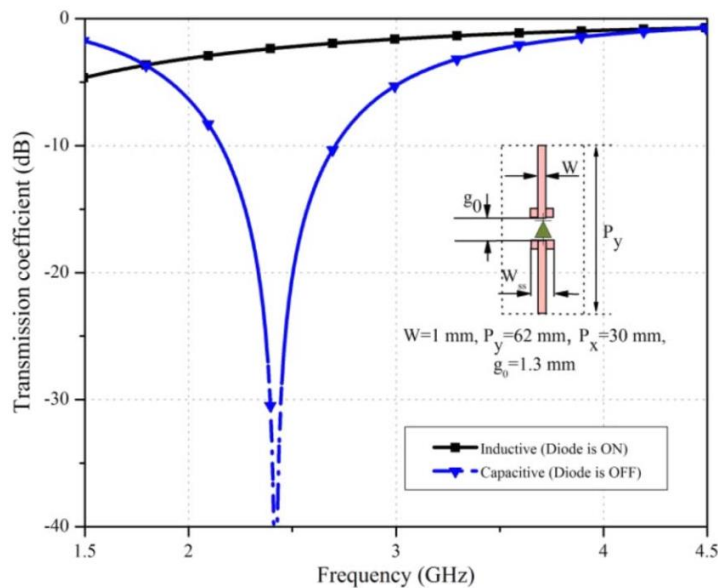
Fig. 3-1 Transmission response of an active FSS screen constructed of discontinuous capacitive loaded strips.

(a

(b
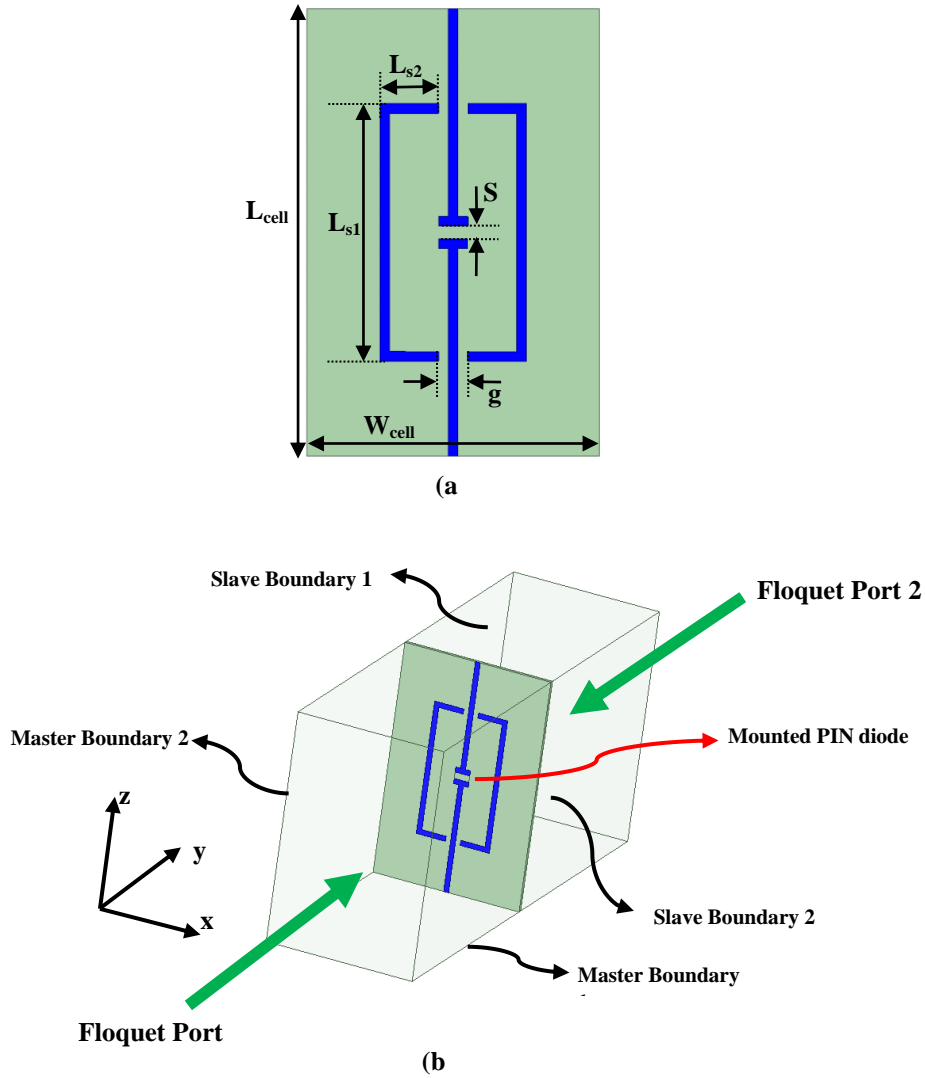
Fig. 3-2 (a) Proposed magneto dielectric FSS unit cell dimensions. (b) Specific boundary conditions and defined Floquet port excitation to extract scattering parameters. The unit cell dimensions are Lcell=46, Wcell=30, Ls1=26.5, Ls2=5, S=1.3, g=1, all in millimetre.
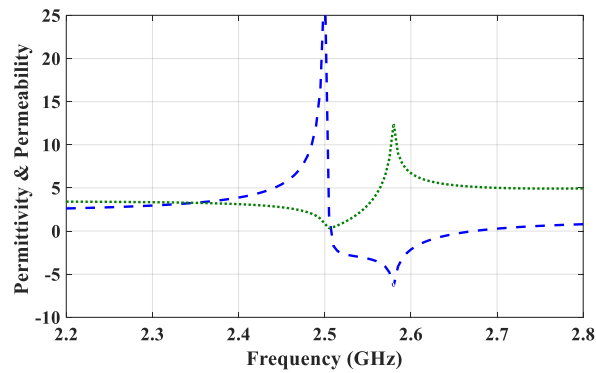
Fig. 3-3 Effective constitutive parameters of the magneto-dielectric FSS wall.
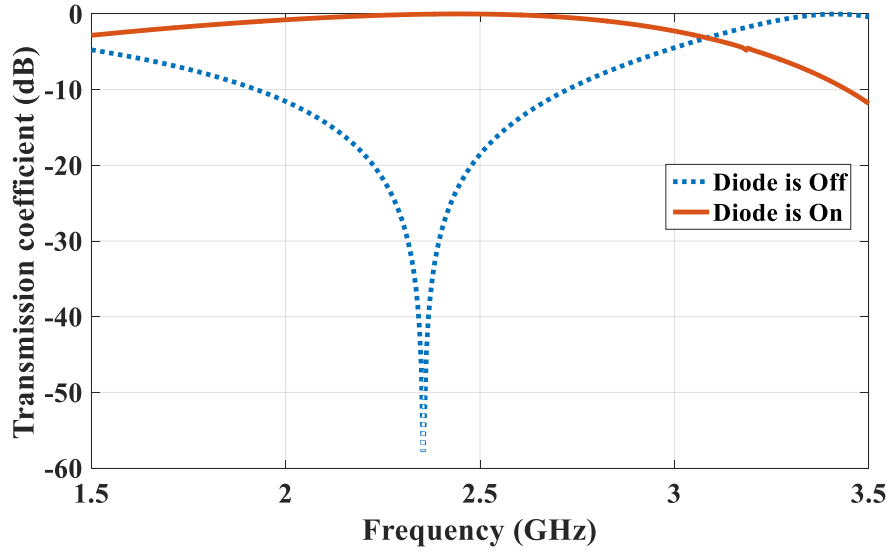
Fig. 3-4 Transmission response of the magneto-dielectric FSS wall.
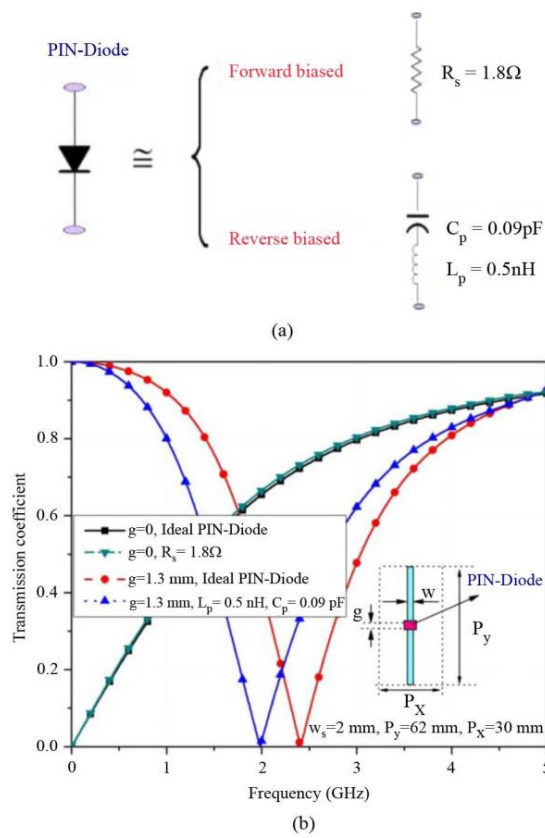
Fig. 3-5 Active element mode used in the simulations and its effect on the EM response of the discontinuous strips unit cell. (a) Actual PIN-Diode electrical circuit model used in the simulation. (b) Simulated transmission coefficient of the discontinuous strips

3. 3 Proposed Omnidirectional Pattern Antenna

A compact monopole antenna is shown in Fig. 3-6. It is in fact a simplified one of the presented monopole antenna in [24]. The proposed monopole antenna is selected because of its omnidirectional radiation characteristics at 2.45 GHz in the azimuth-plane, which makes it ideal to be employed in the proposed beam-switching antenna. Moreover, this monopole antenna configuration is simple, which makes it easy for fabrication. The monopole antenna constructed of two rectangular stepped monopole elements printed on the top of each other with a small GND plane in the back side of the substrate. The upper side resonators of the antenna are two rectangular patch with different sizes and designed to operate at 2.45 GHz. The proposed antenna can be fed directly by a 50 Ω coaxial cable. The proposed antenna was fabricated on the RO3006 substrate with a relative-permittivity of $\varepsilon_r = 6.15$ and a thickness of 1.27 mm. The optimized geometry parameters are given as: b_1=12 mm, a_1=12 mm, b_2=9 mm, a_2=10 mm, a_3=4.6 mm, b_3=7 mm. The simulated and measured reflection coefficients are shown in Fig. 3-7. From it, it can inferred that the measured results have a good agreement with simulated ones while a negligible frequency-shift happened mostly due to fabrication tolerances. The simulated and measured radiation patterns of the proposed monopole antenna is shown in Fig. 3-8.
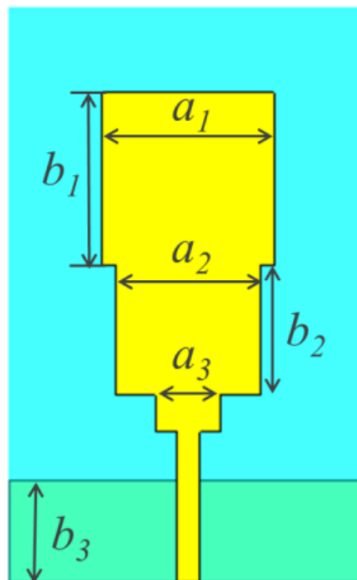
Fig. 3-6 Geometry of the proposed omnidirectional monopole antenna.
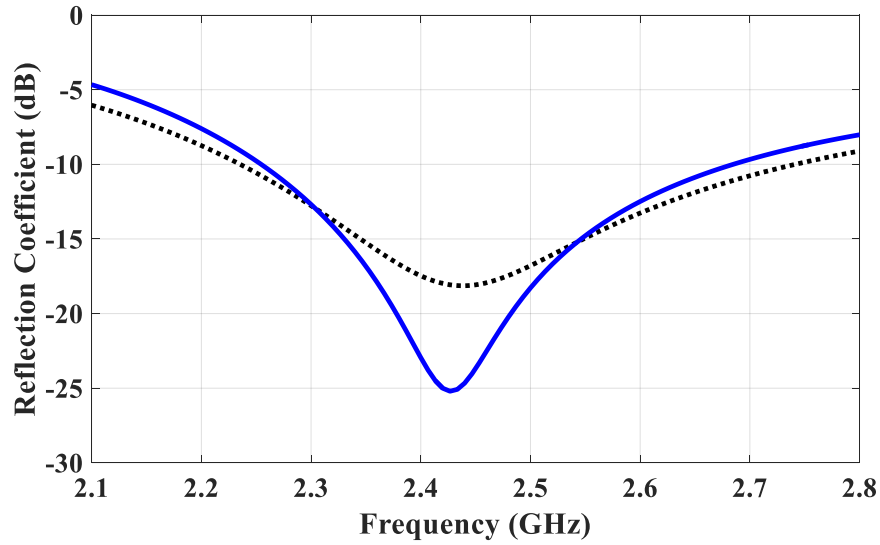
Fig. 3-7 Simulated and measured reflection coefficients results of the proposed omnidirectional monopole antenna.

Fig.

3-8

(a

(b

(c
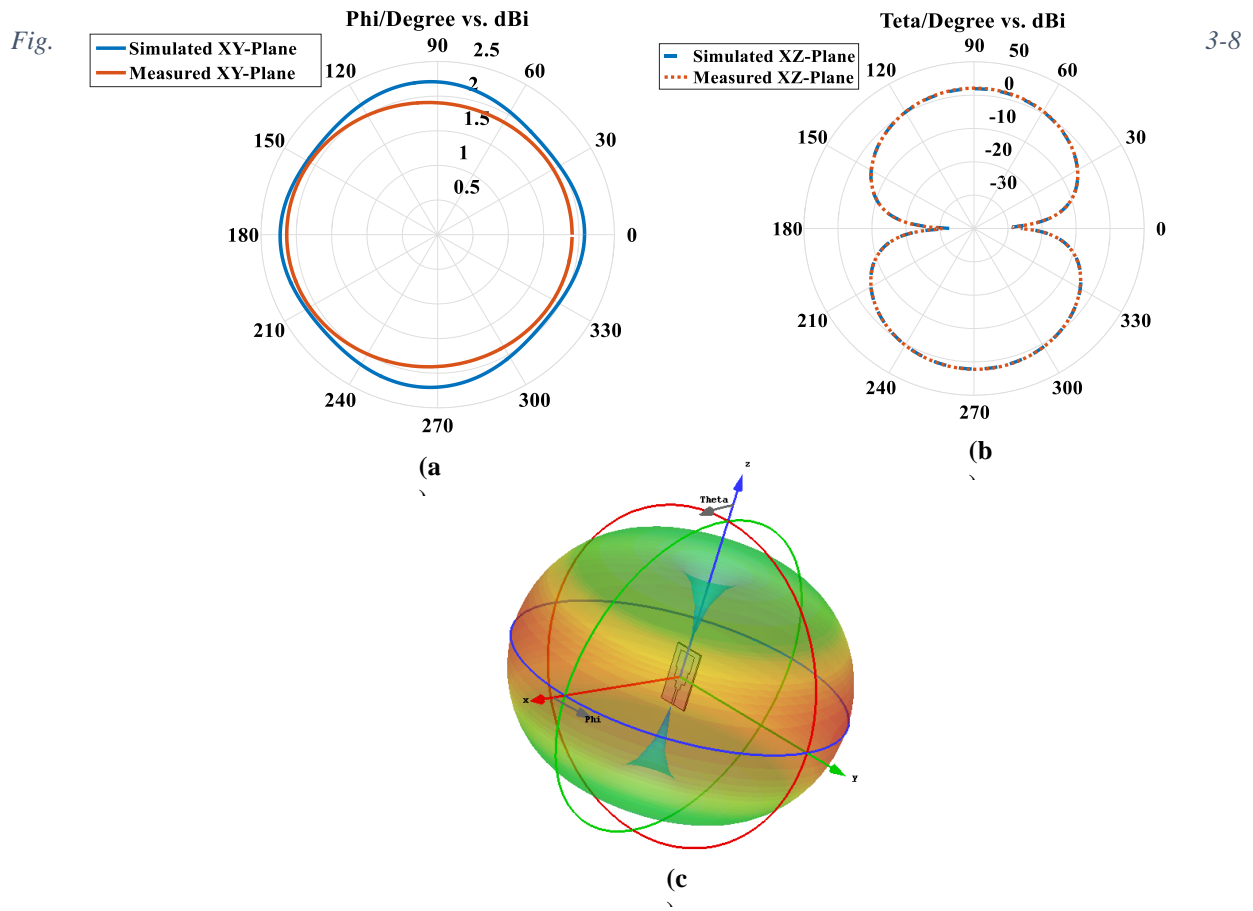
Simulated and measured radiation pattern of the proposed omnidirectional monopole antenna at 2.45 GHz.

3. 4 Proposed Pattern - Reconfigurable Antenna using Active FSS

The proposed pattern-reconfigurable antenna is shown in Fig. 3-9. Since the radiation mechanism of the pattern-reconfigurable antenna in Fig. 3-9 is based on the principle of reflector antenna, its overall physical dimensions are first calculated using the available formulated reflector structure, which is an octagonal corner-reflector antenna. Then, based on the calculated physical size for the cylindrical reflector and its reflection mechanism, a semi-cylindrical solid reflector is fitted to the octagonal corner-reflector to evaluate and calculate the appropriate size of the octagonal corner-reflector active FSS. Accordingly, the radiation mechanism which is shown in Fig. 3-10 is considered, where the illuminating source is placed on the axis of the semi-cylindrical solid reflector at radius distance of R. As it is known, based on the distance between the dipole and the semi-cylindrical solid reflector, the reflected waves from the side walls of the octagonal corner-reflector active FSS can be in phase. Moreover, this distance also indicates the level of the secondary lobes, side-lobe level and back-lobe level of the radiation-pattern, and the radiation resistance of the octagonal corner-reflector active-FSS antenna [25]. Therefore, based on the central illuminating source position R, different design positions can be chosen with an optimal directive radiation pattern. In this work, an omnidirectional dipole is placed at the first place position to achieve the minimum dimensions for the octagonal corner-reflector active FSS. This will reduce the required active-elements and the fabrication cost of the reconfigurable reflector. Therefore, the antenna distance from the octagonal corner-reflector active FSS is chosen in the range of 0.25–0.7 λ_o, where λ_o is the wavelength in the free space at the operating frequency. For this octagonal corner-reflector active FSS, the width of $W_{aperture}=2R$ is large enough to reflect the main parts of the waves which contributing to the main lobe of the radiation pattern [25]. Furthermore, the principal operation of the reflector is that which a wave radiated from the dipole is reflected parallel to its axes. Therefore, the main part of the waves radiated from the dipole at its center will be reflected back along the octagonal corner-reflector active-FSS axis. In fact, this octagonal corner-reflector active-FSS provides a radiation characteristic similar to a semi-cylindrical solid reflector with a radius dimension of (R). The hight of reflector is selected larger than the illuminating source dipole to reduce the back radiation in the E-plane. Therefore, L_{wall} is chosen larger than a wavelength, and based on the unit-cell periodicity, it is chosen in a way to consist three unit cells. The number of unit cells in each reflector wall is also selected according to the designed unit-cell periodicity and radius of the octagonal corner-reflector active FSS. Therefore, an array of 2×3 unit cells is chosen to be embedded in each reflector wall, which also shows the number of switching steps for the radiation pattern to support the entire azimuth angles in 8 steps or 8 sectors, as defined in Fig. 1-7.

(a)

(b)

(c
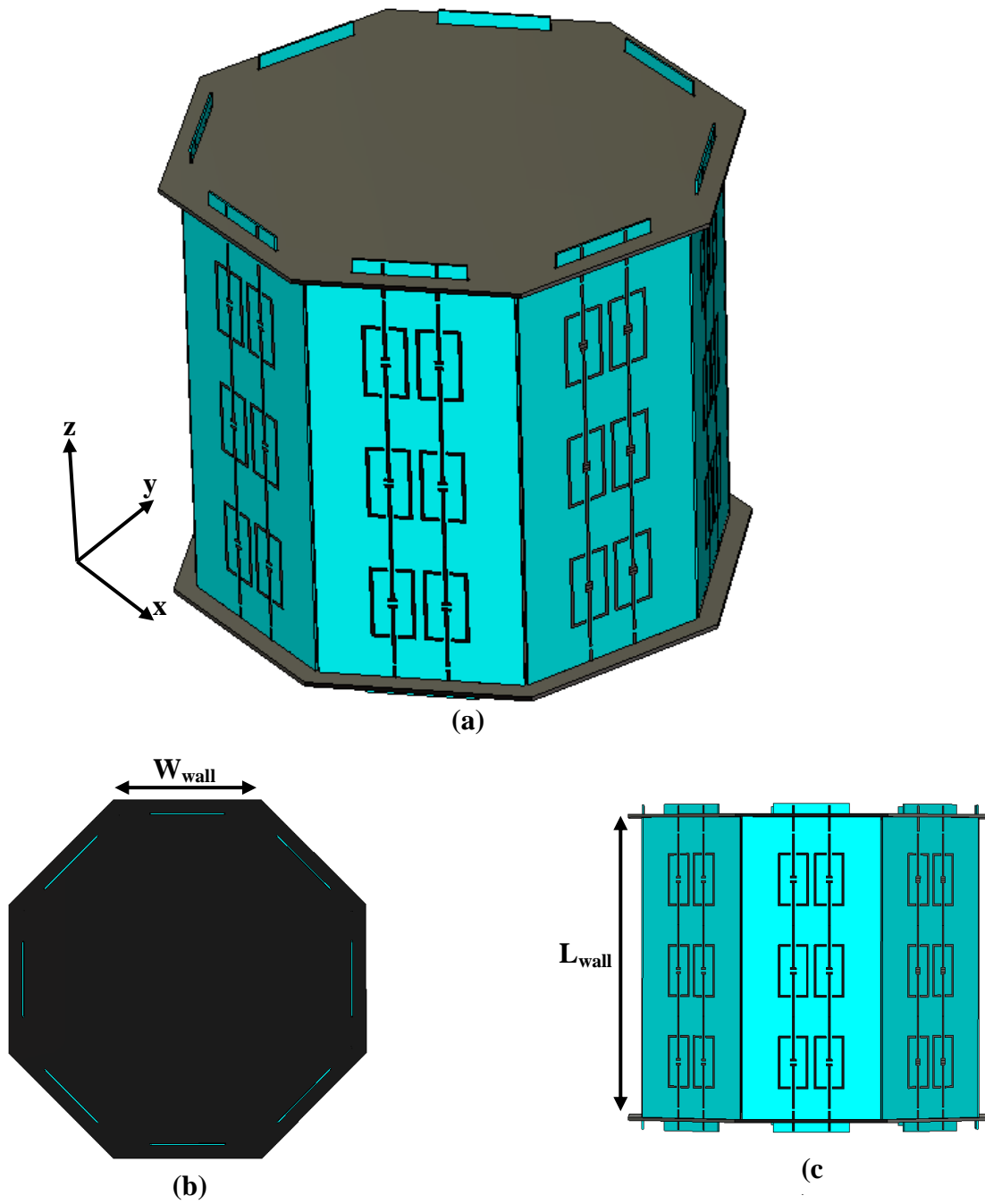
Fig. 3-9 The proposed pattern reconfigurable active FSS antenna structure. (a) 3D view of the proposed pattern reconfigurable active FSS antenna. (b) Top view. Side view.

Cylindrical solid reflector

$R \approx 0.25\text{–}0.7\ \lambda_o$

W_{wall}

Omnidirectional pattern antenna

$W_{aperture}$

Proposed octagonal corner-reflector
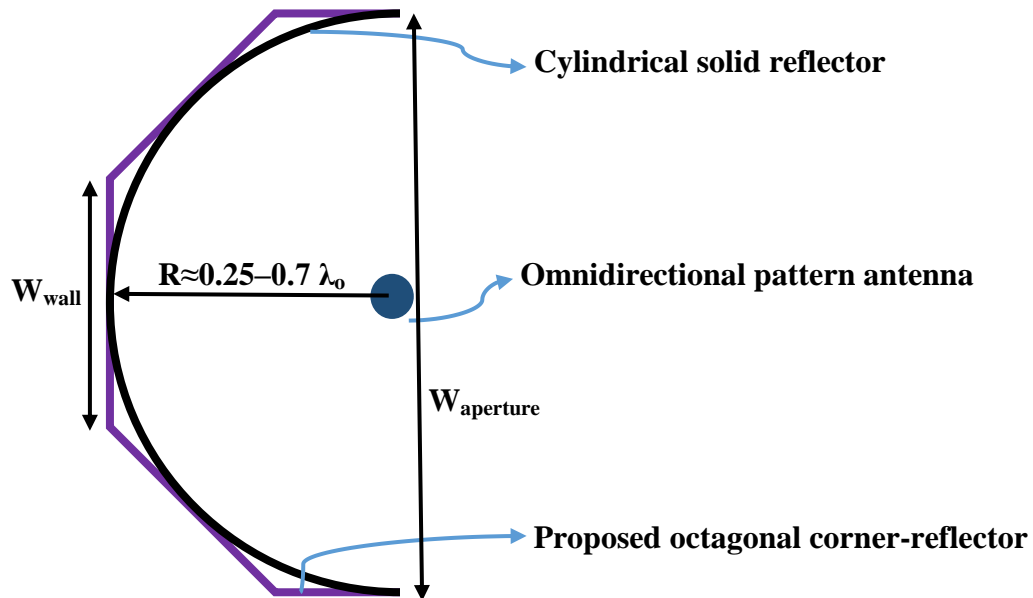
Fig. 3-10 Geometry of the cylindrical reflector antennas and FSS reflector.

Fig. 3-11 shows the simulated reflection coefficient results, carried out using HFSS software for the antenna geometries shown in Figs. 3-9. The final dimensions of the octagonal corner-reflector active FSS antenna used in the simulations are presented in Fig 3-9, and the unit cell dimensions have been given in Fig. 3-2. The reflection coefficient curves show that all antenna offers a matching band around 2.45 GHz. On the other hand, since the transmission response of the FSS screen is frequency dependent, the bandwidth of the semi-cylinder FSS reflector antenna is a little smaller than the octagonal corner-reflector active FSS antenna. It means that for the antenna with the octagonal corner-reflector active FSS, the input impedance of the omnidirectional pattern dipole is affected more by the octagonal corner-reflector active FSS. The corner reflector with an aperture of $W_{aperture}$, shown in Fig. 3-10, gives the highest gain. As it was predicted, a semi-cylinder solid-reflector with an equivalent aperture is provided almost a similar gain curve of an octagonal corner-reflector active FSS with the same aperture. However, the gain of antenna with octagonal corner-reflector active FSS surface is more frequency dependent, and its physical dimension is a little larger than the one with a semi-cylindrical solid reflector. As a unique advantage of the octagonal corner-reflector active-FSS, we can mention the effectively increased directivity. It shows that a compromise between the matching and maximum gain should be performed. The expected radiation mechanism of the antenna is successfully confirmed again by investigating its radiation patterns, shown in Fig. 3-12. As can be inferred, the radiation pattern of the proposed antenna is almost the same as the solid cylindrical reflector performances in terms of the back/side lobes.

The design procedure and the key design guidelines of the proposed octagonal corner-reflector active FSS antenna based on reflector antenna principles are summarized as follows:

➢ The antenna frequency is selected based on the required reconfiguration mechanism at the desired operating frequency, which is 2.45 GHz in this project.
➢ The radius of the octagonal corner-reflector active FSS is chosen in the range of 0.25–0.7 λ_o, where the λ_o is free space wavelength.
➢ The number of unit cells on each wall is calculated according to the designed unit-cell periodicity value.
➢ The height of the octagonal corner-reflector active FSS must be larger than a wavelength. Therefore, to obtain the minimum size for the antenna with the desired radiation pattern, three unit cells are considered along the octagonal corner-reflector active FSS axis.
➢ Because of the coupling between the illuminating omnidirectional antenna and the octagonal corner-reflector active FSS, the initial values of the octagonal corner-reflector active FSS radius should be tuned a little. The radius must be chosen in the range of 0.25–0.7 λ_o to ensure a minimum 10% matching bandwidth.
➢ Finally, the antenna dimensions are optimized using HFSS softwave for the desired radiation pattern and matching performance.
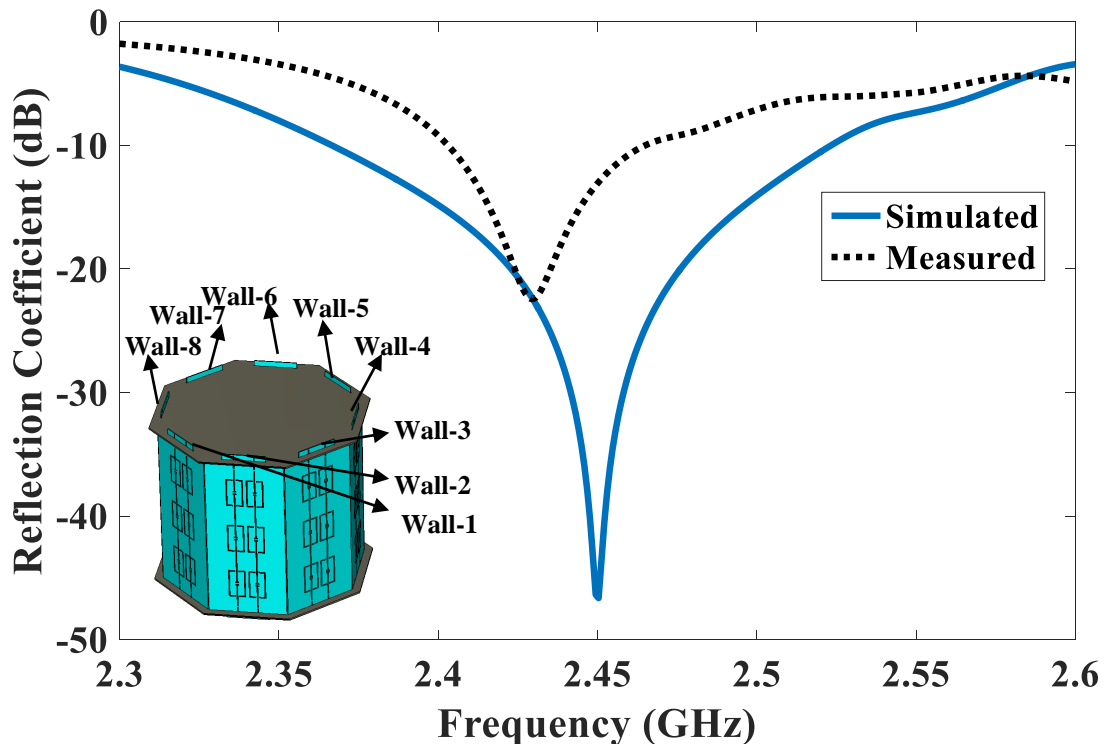
Fig. 3-11 Simulated and measured reflection coefficient results, carried out for the proposed octagonal corner-reflector active FSS antenna geometries shown in Figs. 3-9. The walls number 1, 2 and 3 are active.
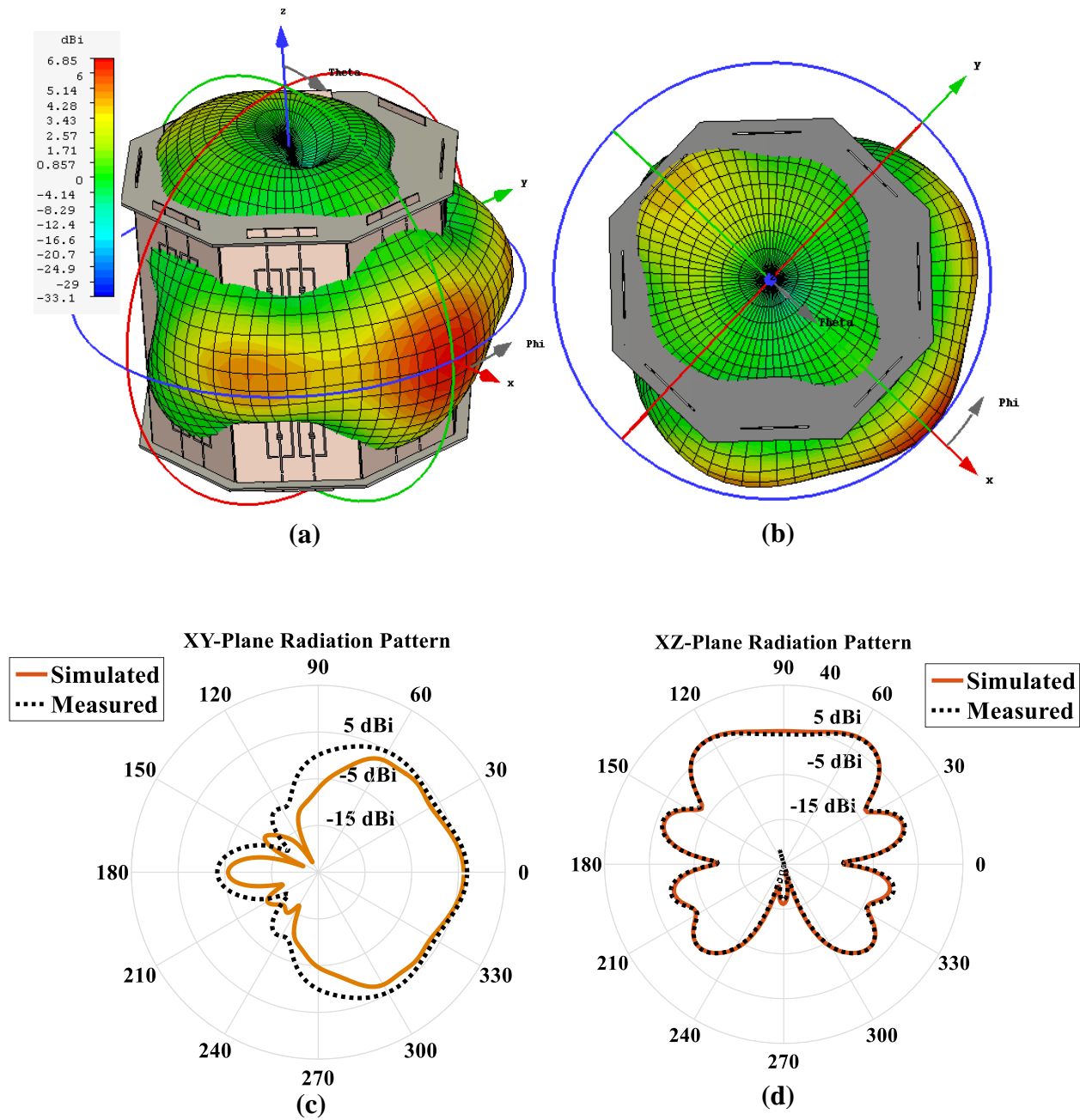
Fig. 3-12 Simulated and measured Radiation pattern results, carried out for the proposed octagonal corner-reflector active FSS antenna geometries shown in Figs. 3-9. The walls number 1, 2 and 3 are active.

3. 5 Measured Results

Fig. 3-13 shows a photo of the proposed fabricated octagonal corner-reflector active FSS antenna prototype based on the dimensions provided in previous sections. A simple omni-directional pattern antenna is used as a base antenna for illuminating the structures as it is explained in Section 3.3. The monopole antenna consists of two rectangular monopole elements attached at the top of each other with a small ground plane on the back of the substrate. The main resonators of the antenna are two rectangular elements with different sizes and designed to operate around 2.45 GHz. The proposed antenna can be fed directly by a 50 Ω coaxial transmission line. In addition, high frequency PIN-diodes, biased with DC-feed network, are connected to the FSS walls using RF-Chock inductors as it is indicated in Fig. 3-13. RF-chocks separate the biasing feed network from the FSS screen over the desired antenna bandwidth, and block the RF signal leakage towards the control unit circuit. Ridged foam is used as a stand to fix the feeding omni-directional pattern antenna in the middle of the cylinder.

To examine the performances of the proposed design, firstly the return losses of antenna is measured. Then, some measurements are performed for the directive H-plane radiation-pattern of antenna to find the best radiation pattern in terms of desired main beam, realized gain, side-lobe and back-lobe levels. Finally, other patterns are measured to evaluate the radiation performances in the other plane. Fig. 3-14 shows the measured results of the octagonal corner-reflector active FSS antenna prototype compared to simulated ones. As it can be noticed, the wideband feeding omni-directional pattern antenna is efficiently working from 2.25 GHz to 2.7 GHz; but when it is placed at the center of the cylindrical FSS, it operates effectively from 2.35 GHz to 2.55 GHz. The measured return loss for this structure demonstrates smaller matching compared to the simulation (from 2.4 GHz to 2.5 GHz). In addition, deactivating the diodes leads to a little shift in the return loss curve, which has been predicted by simulations. Its E- and H-plane radiation-patterns at the frequency 2.45 GHz are compared to the ones related to the octagonal corner-reflector active FSS antenna simulation results. Some asymmetry is noticed in the E- and H-planes of the omni-directional pattern antenna, which is mainly because of the RF-cable and the SMA connector used in the antenna implementation (see Fig. 3-8). However, its H-plane pattern is almost uniformly radiating over all angles. The measured E- and H-plane radiation-patterns demonstrate the best performance at the frequency 2.45GHz, which confirms the integrity of the proposed concept. It is clear that the proposed configuration can provide a directional radiation-pattern with back-lobe level better than -20dB and -17dB for H- and E-plane patterns, respectively. Because of scattering from the aperture edge, this level is a little degrading at the other angles in the back plane. As it would be expected, the parallel DC-feed lines affect the H-plane pattern. The gain of antenna ismeasured using the gain measurement comparison-method. It can be calculated from expression (5-3), in which P_{AUT} is the received power by the antenna under test. P_{STD} and G_{STD} are also the received power and gain of the standard horn antenna.
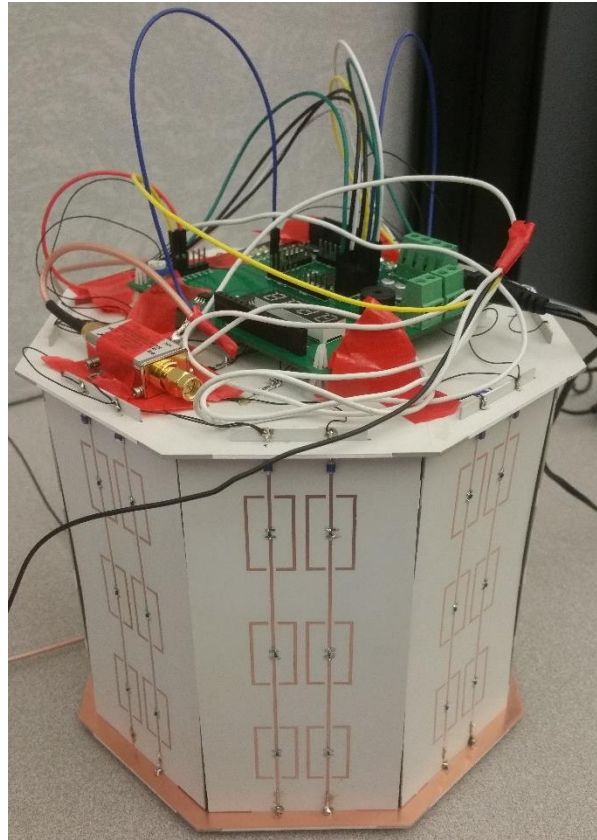
(a)
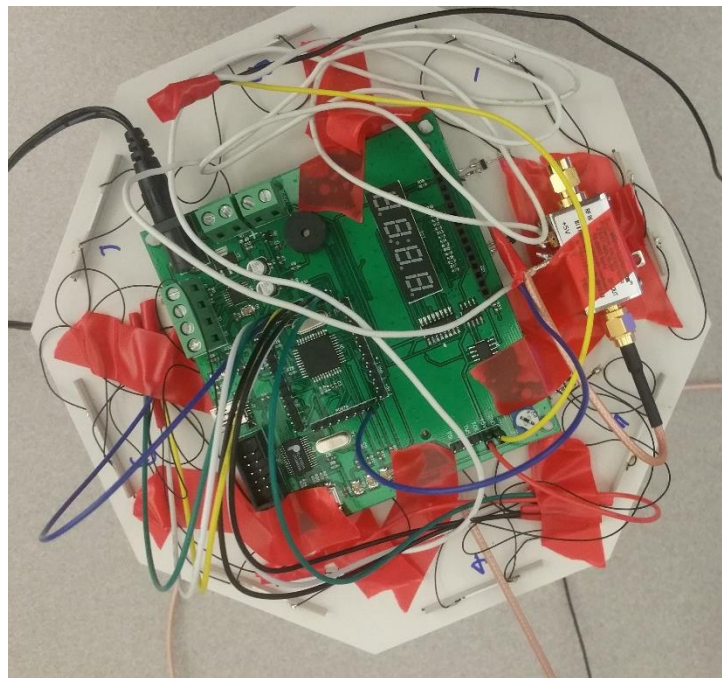
(b)

Fig. 3-13 Photo of the proposed fabricated octagonal corner-reflector active FSS antenna prototype.

$$G_{AUT} = G_{STD}P_{AUT} - P_{STD} \qquad (all\ units\ are\ in\ dB) \qquad (23)$$

Fig. 3-14 shows the measured gain for the antenna at 2.45 GHz. From this figure, it can be noticed that the antenna is able to offer a directive radiation-pattern with more than 5dB gain close to the desired operating frequency. The difference between simulation and measurement is due to the design and measurement inaccuracy.

The proposed antenna, known as an antenna under test (AUT), acts as a receiver (R_x) antenna to test the capability of the antenna to receive the signal from the transmitter (T_x) and to verify the transmitter direction based on the power received (P_r) signal. This will be done by turning the pattern in the 8 different direction using the control unit, measuring and saving the received power at different directions. By comparing the amount of the received power at the different pattern condition, we can predict the transmitter direction respect to the receiver. Here we have some measurement limitation that we should consider for performing a valid measurement.

First, the power received (P_r) signal measurement is carried out when the distance between the T_x and R_x varies from 1 m to 3 m. If we increase the distance between the T_x and R_x, we would not be able to measure the received power due to the fact that in the control unit the RF power detector (with part number: ZX47-60LN+) has the dynamic range of -60dBm to +10dBm, as it is indicated from the datasheet of the component in Fig. 3-15. Fig. 3-16 shows the free-space propagation loss with two horn antennas versus the distance. Fig. 3-18 shows the photo of the antenna measurement test setup. In this work, the measurement are done in a conditions, which is in an archaic chamber (7.95 m × 3.17 m) in the Antenna Research Group lab. Firstly, the practical indoor propagation is carried out in an archaic chamber at 1.6 m distance between the T_x and R_x. However, at the distance more than 1.5 m, this test is not applicable due to the fact that we don't have a receiver chain for AUT outside of the chamber for evaluating the different users. During the indoor measurements, the actual frequencies from the return loss experimental results, namely, 2.45 GHz are used to inject the signal at the RF signal generator. The AUT measurement is carried out with a fixed selected pattern direction. The indoor practical antenna measurement setup is shown in Fig. 3-17. Both AUT and positions at a height of 1 m must be placed face-to-face and aligned towards each other to obtain a line-of-sight (LOS) condition. At the left side, the signal generator is used to inject the RF signal to the AUT, while the equipment at the right side is a receiving antenna connected to the spectrum analyzer. Theoretically, the path loss (P_L) versus the distance between the T_x and R_x is described in the ground reflection (two-ray) propagation model [26], as formula shown in (24). Consider

$$P_L = 32.44 + [20\log(d)] + [20\log(f)] - G_T - G_R + [T_{other\ losses}] \qquad (24)$$

where *d* is the distance (km), *f* is the frequency (MHz), G_T is the transmitter gain (dBi), G_R is the receiver gain (dBi), and $T_{other\ losses}$ includes the floor, wall in [26]. The G_R gain value refers to the AUT during the simulation and the G_T gain value refers to the horn antenna with 10 dBi gain. When the distance between T_x and R_x increases, the signal decreases. The calculated received power is -50dBm for 1.6 m distance between T_x and R_x. If we increase the distance, the RF

power detector would not be able to measure the receiver power efficiently. So we select the distance 1.6 m between T_x and R_x.
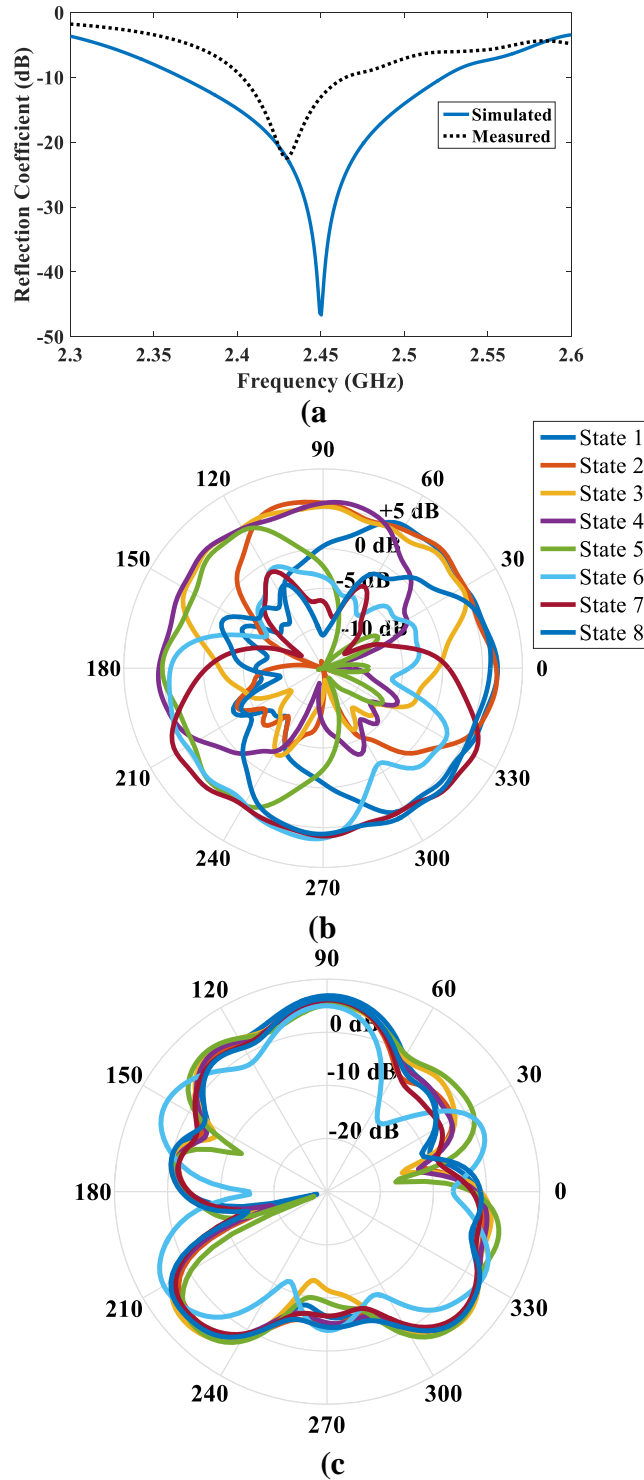
Fig. 3-14 Measured results for octagonal corner-reflector active FSS antenna (a) Reflection coefficient. (b) H-plane radiation-pattern. (c) E-plane radiation-pattern.

Simplified Functional Diagram

(a)

(b)
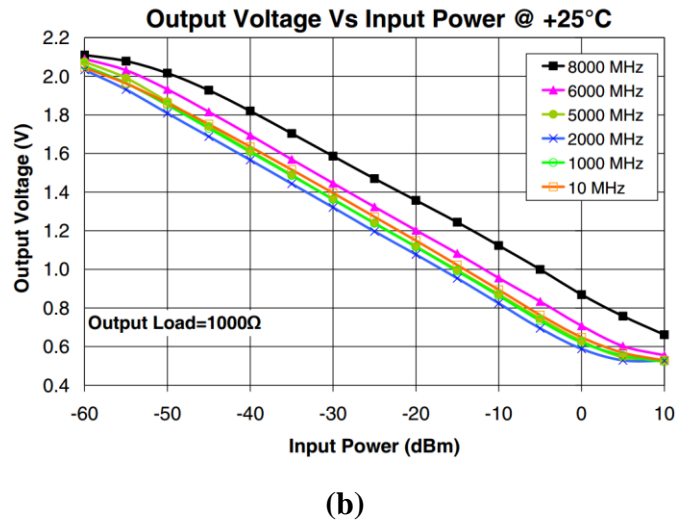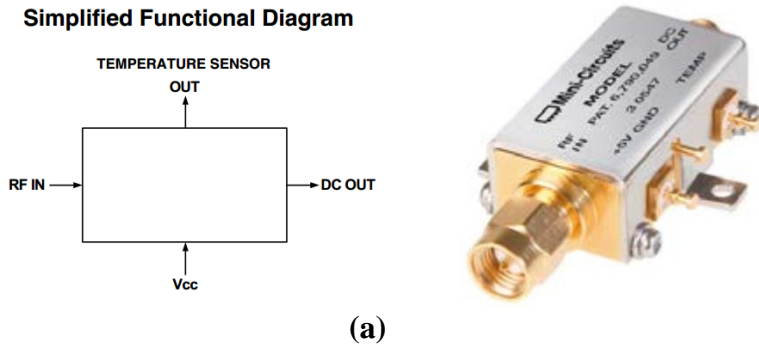
Fig. 3-15 Output Voltage Vs Input Power for the RF power detector (with part number: ZX47-60LN+).
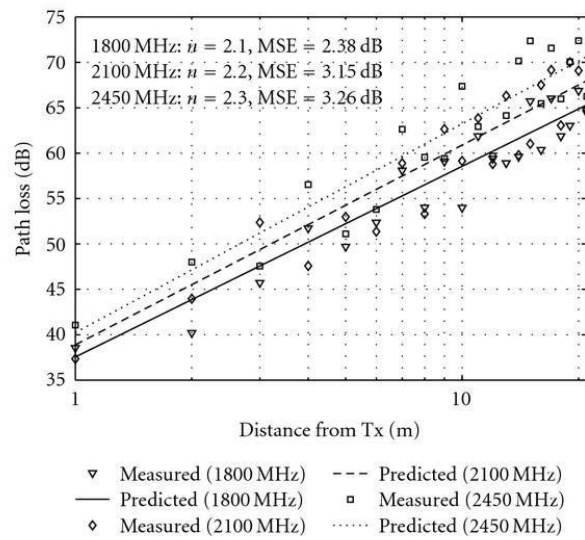
Fig. 3-16 Free-space propagation loss with two horn antenna versus the distance.
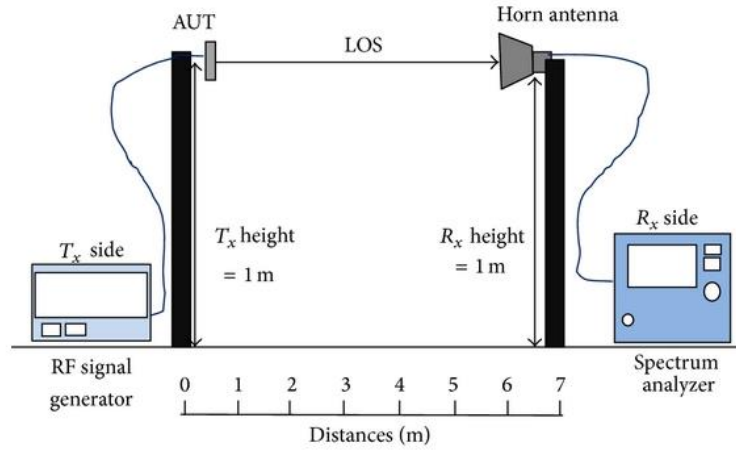
Fig. 3-17 The practical antenna measurement setup.
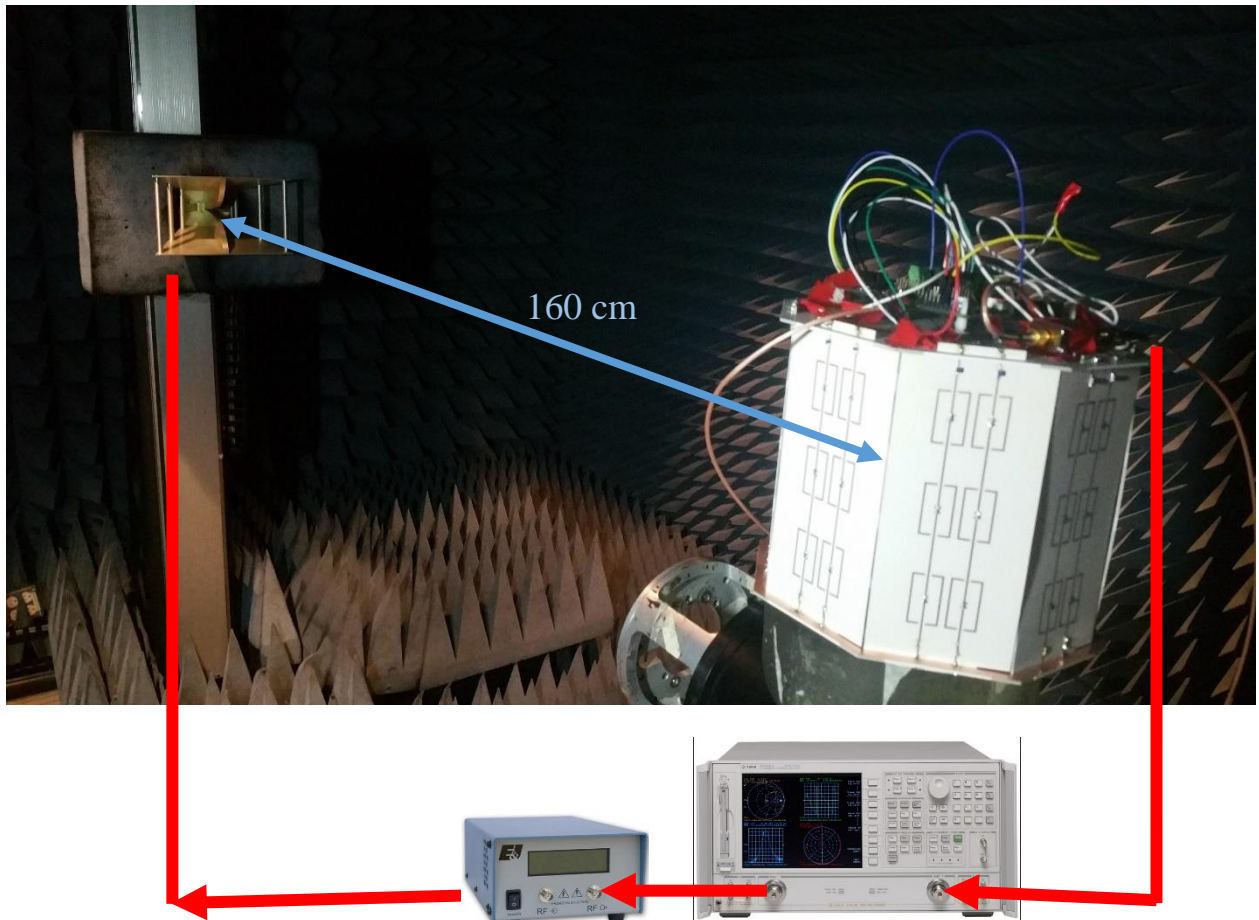
Fig. 3-18 Photo of the antenna measurement setup.

To summarize the obtained results, the data of gain, additional gain (AG) compared with the dipoles, 3 dB-beam width (3 dB-BW), side lobe level (SLL), and front-back ratio (FBR) are shown in Table 1. The additional gain reaches 3.61 dB at 2.45 GHz, and it is higher than 4.44 dB at 2.4 GHz. The 3 dB-beam width is from 27º to 34º. Another significant difference between this antenna and those mentioned in [19–21] is that a very deep nulling level can be achieved. We alternated the goal of the program to achieve an increasingly lower side lobe level in H-plane.

Table 1: Survey of the octagonal corner-reflector active FSS antenna.

Freq (GHz)	Gain (dBi)	AG (dB)	3dB-BW (degree)	SLL (dBi)	FER (dB)
2.4	5.45	4.44	27	3.49	17
2.45	5.3	3.61	26	4.1	20
2.5	5.1	3.53	34	3.54	18

3. 6 Conclusion

In this chapter, a highly agile electronically steerable octagonal corner-reflector active FSS antenna is proposed. The antenna is continuously steerable and outperforms many PIN-diode based on FSS configurations. The measured results achieved additional gain of up to 3.61 dB and a deep nulling level of −20 dBi. The 3 dB beam widths are 27°–34°, they can offer a steering resolution of 1°. Beam bandwidth measurement shows that it can offer stable high-gain mode for 2.45 GHz WiFi band.

Chapter 4 Design of the Control Unit for the Proposed Pattern Reconfigurable Antenna Based on Active Frequency Selective Surface

4. 1 Introduction

In this chapter, a control unit is presented which assists the antenna part to steer the radiation beam in the H-plane. Then,   by comparing the received power in different angle decides which direction is the arrival of the transmitted signal and based on that send a proper DC power to biasing circuit of the FSS walls to switch on or off the FSS layers.

Fig. 4-1 reveals the proposed control unit which is designed to allow easy build own Atmega control system or simply AVR platform. It also could be used for prototyping or purposes. The board contains most fundamental components, and everything is already prepared.

The ATA16R is an AVR based Board. Atmega16 (TQFP44) is used as the main controller on the kit. Board has special feature to control two DC motors or one step motor. Maximum total current is 1000mA. The functional block schematic of the circuit is shown in Fig. 4-2. Fig. 4-3 shows different part of the circuit in the proposed control unit.
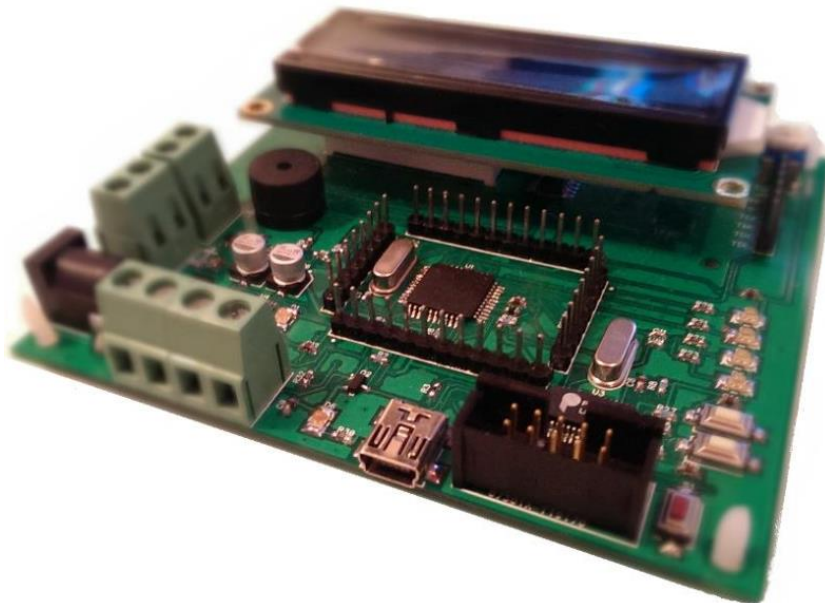
Fig. 4-1 Photo of the antenna control unit.
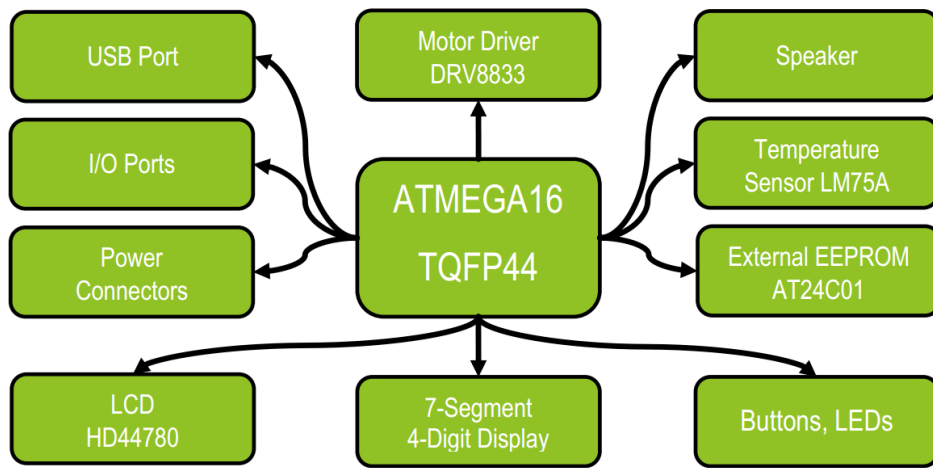
Fig. 4-2 The functional block-schematic of the antenna control unit.
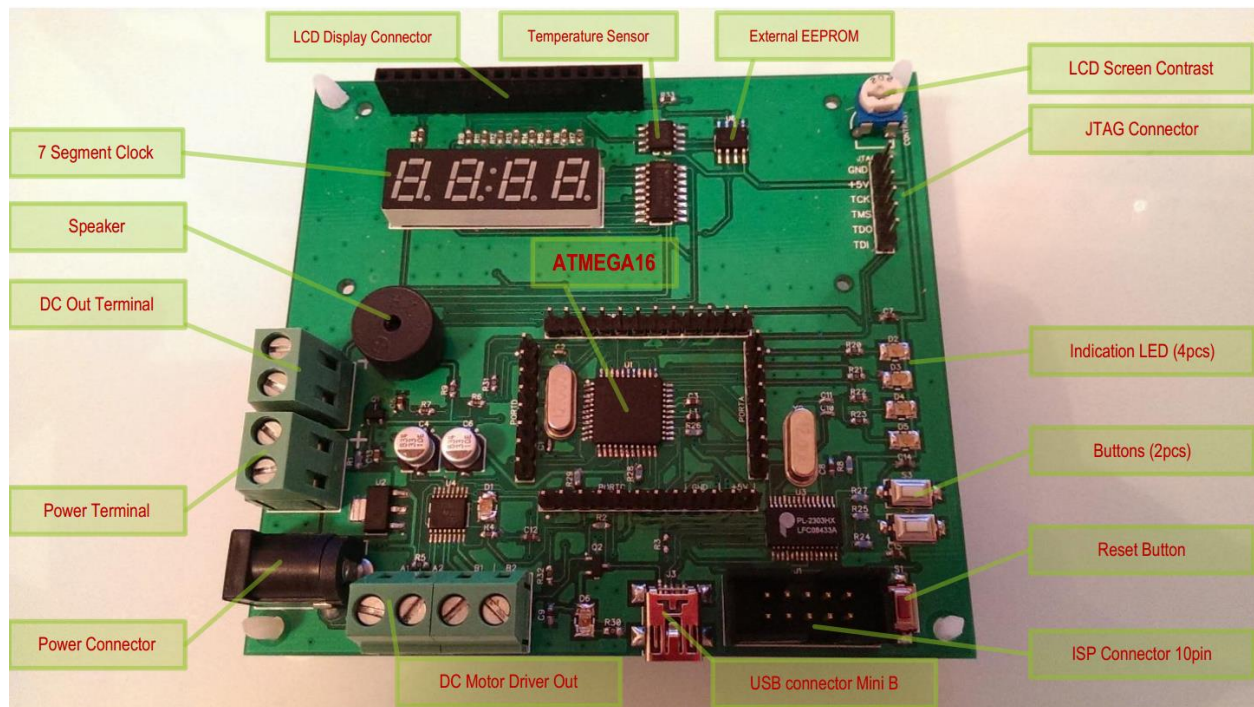
Fig. 4-3 The functional block-schematic of the antenna control unit.
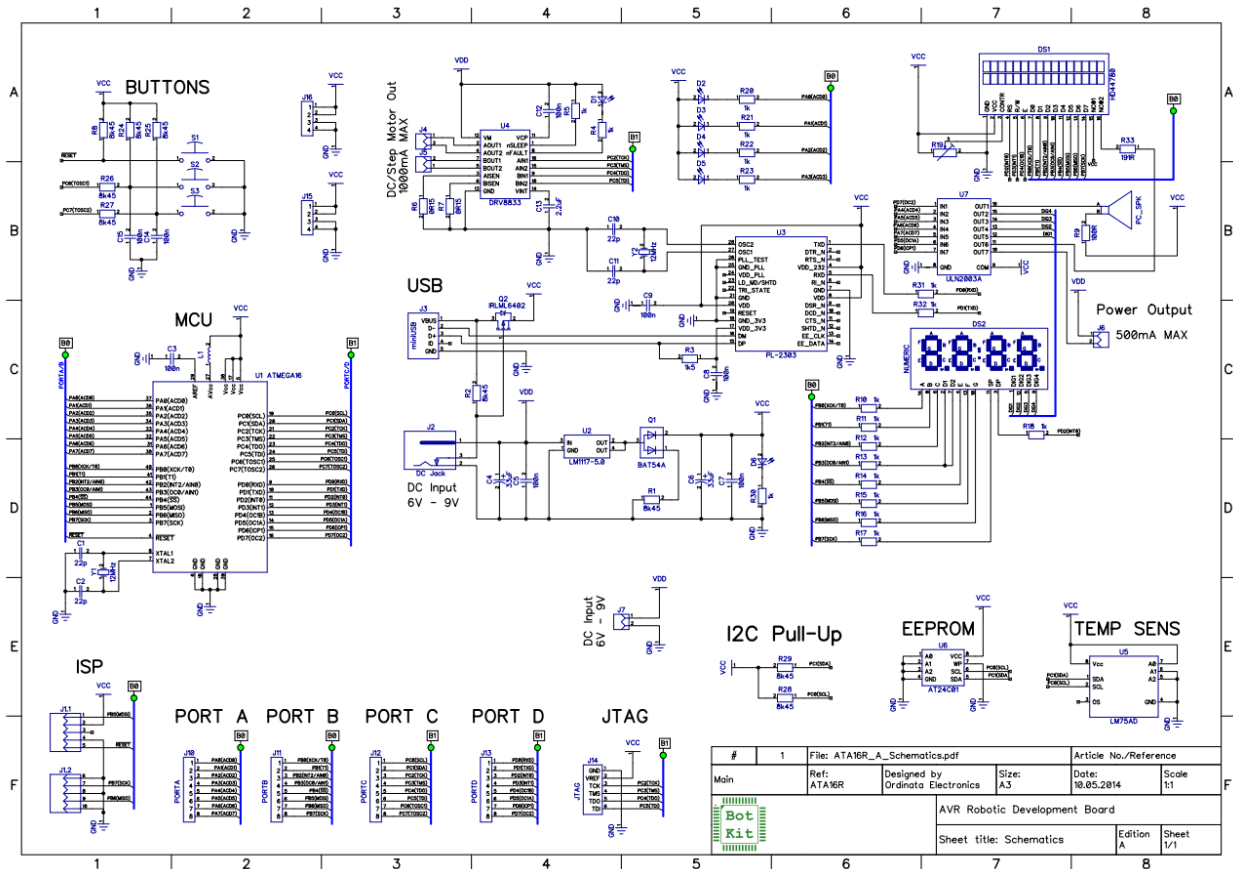
Fig. 4-4 Schematic of the antenna control unit.

4. 2 Control unit interface with the Reconfigurable antenna

In this section the interface between the proposed pattern reconfigurable antenna and the control unit as shown in Fig. 4-5 is presented. We have two input line to the control part; the temperature sensor and the DC out which are connected to the ADC0 and ADC1 channels of the microcontroller, respectively. The ATmega16 features a 10-bit successive approximation ADC. The ADC is connected to an 8-channel Analog Multiplexer which allows 8 single-ended voltage inputs constructed from the pins of Port A. The single-ended voltage inputs refer to 0V (GND). The device also supports 16 differential voltage input combinations. Two of the differential inputs (ADC1, ADC0 and ADC3, ADC2) are equipped with a programmable gain stage, providing amplification steps of 0 dB (1x), 20 dB (10x), or 46 dB (200x) on the differential input voltage before the A/D conversion. Seven differential analog input channels share a common negative terminal (ADC1), while any other ADC input can be selected as the positive input terminal. If 1x or 10x gain is used, 8-bit resolution can be expected. If 200x gain is used, 7-bit resolution can be expected. The ADC contains a Sample and Hold circuit which ensures that the input voltage to the ADC is held at a constant level during conversion. Fig. 4-6(a) shows the transform function of the RF power detector, and Fig. 4-6(b) shows the slope versus frequency over temperature range. As it can be seen from Fig. 4-6(b), the transform function slope of the

proposed RF power detector is -20 mv/dBm; as a result, we need a very accurate ADC conversion with the noise cancellation architecture.

Moreover, we have 8 output IO channels which can control the state of the SRR wall RF pin diodes. All AVR ports have true Read-Modify-Write functionality when used as general digital I/O ports. This means that the direction of one port pin can be changed without unintentionally changing the direction of any other pin with the SBI and CBI instructions. The same applies when changing drive value (if configured as output) or enabling/disabling of pull-up resistors (if configured as input). Each output buffer has symmetrical drive characteristics with both high sink and source capability. The output drive current is not enough to drive the RF pin diodes on the SRR walls. So we need buffer circuits to amplify the output current. The common ground is required to bring the current flowed to the walls back to the control unit.

The C++ code program of the MCU (micro controller unit) is given in Appendix 1.
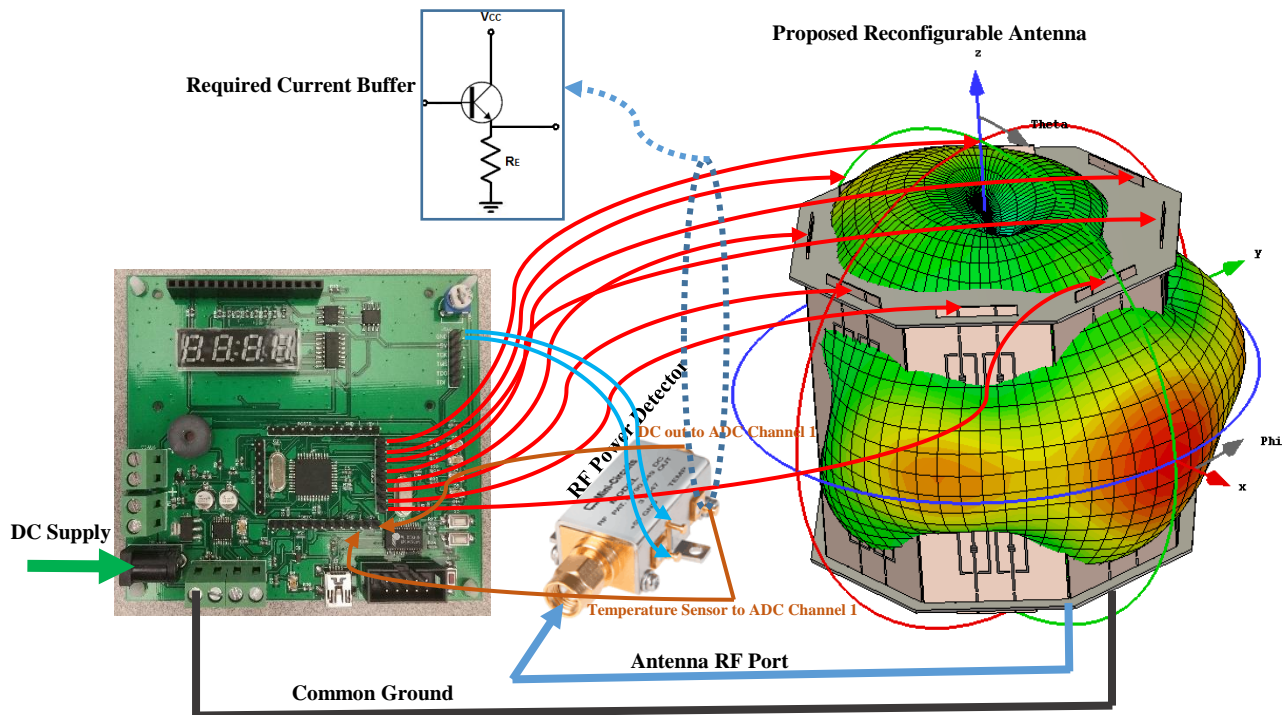
Fig. 4-5 Interface between the proposed pattern reconfigurable antenna and the control unit.
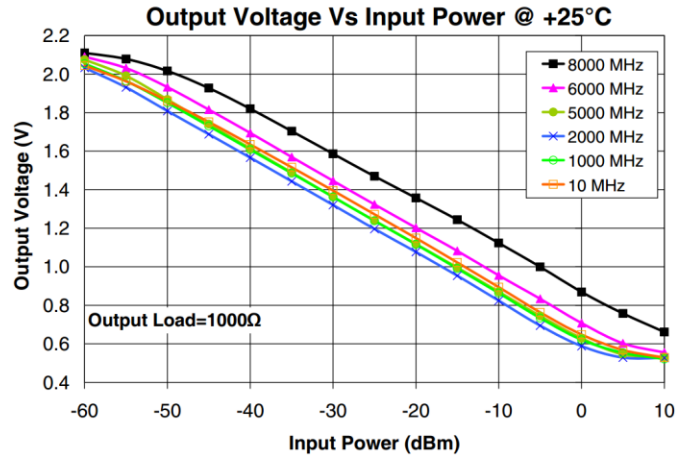
(a)
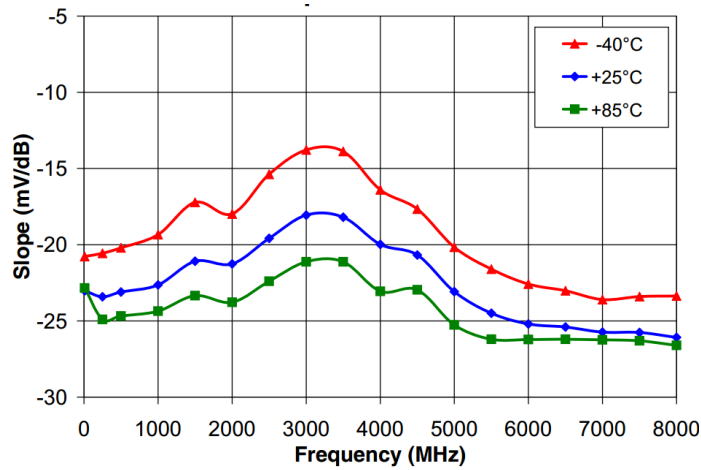
(b)

Fig. 4-6 (a) Output Voltage Vs Input Power for the RF power detector (with part number: ZX47-60LN+). (b) Slope versus frequency over temperature range.

4.3 Conclusion

The control unit based on AVR mirocontroler with   8 outputs is linked to eight FSS layer so as to switch the radiation beam of the monopole antenna. RF power detector is also connected to the antenna and based on the received power, the control unit decides which FSS layer should be switched on or off, which this was implemented by programing code in C++.

Chapter 5 Conclusion and future research works

5. 1 Conclusion

In this thesis, the investigation results on the applications of frequency selective surfaces in reconfigurable antennas have been presented. As the main objective of the work, this type of periodic structure has been pulled together with certain reconfigurable mechanisms to propose a group of new versatile reflector antenna structures─ those called "octagonal corner-reflector active FSS antenna". In fact, proposed antennas have this capability to sweep all azimuth angles, and they also can reconfigure their radiation-pattern from directional to omni-directional states. To successfully accomplish this mission, a step-by-step design procedure has been performed in this work, which is concluded in the following paragraphs. In the first step, the marvels of frequency selective surfaces in creating dual responses have been explored and the possible reconfiguration mechanisms using high frequency switches are identified. It has been demonstrated that the type of feeding method of active elements dictates the reconfiguration mechanism of the proposed reconfigurable frequency selective surfaces.

Moreover, it is theoretically and experimentally shown that the DC-feeding lines of active elements significantly affect the transmission/reflection responses of the electromagnetic windows. It has also been investigated that non-ideal effects of active elements undesirably change their responses. Therefore, both DC-feeding line and parasitic elements of PIN-diodes must be considered in the design process to obtain the desired reconfiguration performances. It has been demonstrated that to precisely fit the measured transmission response of the reconfigurable sheet constructed by a periodic array of discontinuous strips, a correction factor is required. This is indeed required to incorporate the effect of the fringing field around the discontinuous gaps. Then, an octagonal corner-reflector reconfigurable antenna topology has been proposed to meet the desired nimble-antenna functionalities. The obtained results have demonstrated that because of symmetrical illuminating mechanism used in this radiation topology, reforming the planar frequency selective surfaces to conformal cylindrical shape does not significantly change the transmission/reflection responses of the sheets. However, the undesired effect of non-ideal active elements significantly changes the radiation performances of the proposed pattern reconfigurable antenna by deviating the transmission/reflection responses of each semi-cylindrical parts of the reconfigurable electromagnetic window. It means that to obtain the desire radiation performances for the antenna, more care needs to be taken for this effect to enhance the relevant transparency/reflectivity levels of each semi-cylindrical part.

5. 2 Future Research Works

In this thesis, some research work has been carried out on the single layer planar and conformal reconfigurable frequency selective surfaces for antenna applications. However, not fully covered in this limited work, some other interesting investigations in this area are still left for future research topics as articulated in the following paragraph.

According to the multi-disciplinary research topics undertaken in this dissertation, three future avenues in different research topics can be foreseen. The first one deals with the alternative reconfiguration technologies that can be used for the proposed radiation topology in this thesis. As it is demonstrated, non-ideal switch effects and their biasing DC-feed lines significantly change the performances of the reconfigurable sheets. Finding other reconfiguration mechanism with emerging new technologies like MEMS, ferroelectric and plasma materials might be an interesting topic to tackle this problem and enhance the antenna performances and probably increasing its functionalities.

The second research avenue treats with the frequency selective surfaces. In this thesis, only a certain group of single layer screens are investigated just for TE-incident polarization. The possibility of applying other resonant elements, the effect of incident angles in improving their responses in conformal configuration, increasing the number of sheets in antenna configuration to improve its back radiation performances can also be some other future research topics. More importantly, the designed frequency selective surfaces are used in the near-field region of the dipole antenna. Calculating the radiation characteristics of the antenna with an appropriate full wave numerical method is another research topic that probably can explore some other attractive phenomena that are not considered in the current work. Antenna radiation topology can be the third interesting future research topic. In this thesis, the antenna radiation-pattern is sweeping only the azimuth angles and it deals with vertical polarized waves. Changing the radiation mechanism to sweep the elevation angles, handling both vertical and horizontal polarizations and proposing a particular method to increase antenna gain by a minimum cylinder height can be recognized as other future research topics in the antenna avenue.

Chapter 6 RESUMÉ

6.1 Introduction

Nous étudions en profondeur, le long de ce chapitre, les principes fondamentaux de la théorie des lignes de transmission des surfaces inductives et capacitives. Ces surfaces périodiques passives ont été utilisées pour réaliser la surface SSF reconfigurable proposée pour contrôler les ondes électromagnétiques incidentes. Le but est de concevoir une antenne reconfigurable que nous proposons à 2.45 GHz. Ceci est réalisé en reconfigurant l'impédance équivalente de l'écran vu par les ondes incidentes: inductive à capacitive. Une antenne à 8 panneaux est sélectionnée pour être conçue avec la technique proposée à 2.45 GHz. La section 6.2 portera sur une présentation et une conception de la fréquence active sélective proposée. Dans la section 6.3, nous concevons une antenne omnidirectionnelle, nous discutons par la suite des possibilités de son intégration au sein de l'antenne reconfigurable proposée. Dans la section 6.4, nous visons à concevoir, de manière complète, l'antenne reconfigurable eu diagramme, et nous verrons en fin de cette section une simulation de l'antenne proposée. La section 6.5, nous présentons les résultats mesurés et les comparons avec les données de simulation.

6.2 Gamme de surfaces sélective en fréquence active proposée

La Fig. 6.1 montre la réponse d'une structure SSF active. Les paramètres S sont présentés. Une cellule unitaire de SSF consiste en un dipôle à charge capacitive discontinue, intégré à une diode PIN monté en surface. En changeant l'état de la diode PIN, une réponse reconfigurable de la bande stoppante est obtenue aux alentours de 2.45 GHz. Toutefois, comme présenté à la Fig. 6.1, lorsque la diode dans la cellule unitaire est dans un état actif, SSF n'est pas complètement transparente pour les ondes verticalement polarisées. Ceci détériore considérablement le diagramme de radiation directive de l'antenne reconfigurable que nous proposons. Ainsi, la caractéristique de transmission du SSF doit être améliorée.

La solution la plus simple est de réduire la largeur de la bande jusqu'à une valeur limitée par des limitations pratiques. Toutefois, la caractéristique de transmission nécessite toujours des améliorations. En étudiant ce sujet plus en détail, nous avons trouvé que ce comportement non parfait du mode de transition est dû au fait que l'onde incidente verra le SSF comme un moyen avec différents paramètres constitutifs. Afin de pallier ce problème, nous avons essayé de concevoir la cellule unitaire SSF proposée comme substrat magnéto-diélectrique. Le substrat magnéto-diélectrique proposé augmente les paramètres constitutifs du substrat hôte. Les

substrats magnéto-diélectriques augmentent généralement la perméabilité du substrat. Cependant, si nous pouvons concevoir un substrat magnéto-diélectrique avec une permittivité et une perméabilité égales, nous pouvons améliorer la réponse SSF active en mode transitoire. Un substrat magnéto-diélectrique peut être composé de circuits de boucles SRR (résonateurs à anneau fendu) intégrés dans un support hôte à alimentation diélectrique faible. Ce substrat magnéto-diélectrique peut fournir une perméabilité et une perméabilité égales ($\varepsilon_r \cong \mu_r$). L'impédance intrinsèque d'un substrat magnéto-diélectrique ($\eta = \eta_o\sqrt{\varepsilon_r/\mu_r}$) sera presque égale à l'impédance intrinsèque de l'espace libre (η_o) si les valeurs de la permittivité relative et de la perméabilité relative sont égales ($\varepsilon_r/\mu_r \cong 1$). Cela permet une large bande passante d'impédance, en raison des conditions d'adaptation d'impédance améliorées entre les deux supports. Par conséquent, et afin d'améliorer la transparence de la structure SSF pour les ondes polarisées verticalement, nous avons intégré un résonateur à anneau fendu autour de la bande discontinue dans une SSF active, comme illustré dans la Fig. 6-2 (a).

Les paramètres constitutifs de la nouvelle cellule unitaire magnéto-diélectrique SSF sont extraits en utilisant la méthode rapportée par Shi et al. [22] sous les conditions limites indiquées dans la Fig. 6-2 (b). Comme présenté dans cette figure, le plan xy inférieur représente la première frontière maître (master boundary). Le plan xy supérieur est la frontière esclave correspondante (slave boundary). De même, les plans yz représentent les secondes frontières correspondantes maître/esclave. Les deux ports sont placés dans des plans xz. La distance entre eux est de 2.5 mm correspondante à une demi-longueur d'onde dans l'espace libre à 60 GHz. Les paramètres du port Floquet, sous les conditions spécifiées des frontières (représentées dans la Fig 6-2 (b)), excitent deux ondes planes avec des champs électriques orthogonaux tels que les modes TE (0,0) et TM (0,0) dans plan de la cellule unitaire magnéto-diélectrique SSF. De plus, les modes d'ordre supérieur peuvent également être spécifiés dans les propriétés du port. Les paramètres constitutifs efficaces sont extraits et peuvent être considérés comme des paramètres constitutifs efficaces de l'ensemble du SSF magnéto-diélectrique (Fig 6-3). Notons que la réponse en fréquence de la cellule unitaire magnéto-diélectrique SSF dépend des dimensions de la cellule unitaire. Les longueurs SRR (Ls1 et Ls2) sont les paramètres les plus importants qui influencent la fréquence de résonance de la cellule unitaire magnéto-diélectrique SSF. La fréquence de résonance du résonateur SRR diminue en augmentant sa longueur (Ls1 et Ls2). Comme on peut le constater sur la Fig. 6-3, les valeurs de la permittivité relative et de la perméabilité relative sont égales ($\varepsilon_r/\mu_r \cong 1$) à la fréquence 2.45 GHz. En conséquence, le magnéto-diélectrique SSF proposé est complètement transparent pour les ondes verticalement polarisées. Cela peut être vu dans les paramètres S de la cellule unitaire magnéto-diélectrique SSF proposée (Fig 6-4).

Dans chaque cellule unitaire magnéto-diélectrique SSF, une diode PIN de montage en surface est également intégrée dans les bandes dipolaires discontinues pour reconfigurer la réponse électromagnétique de la cellule unitaire magnéto-diélectrique SSF. En considérant une cellule unitaire magnéto-diélectrique SSF, quand la diode se trouve dans un état OFF, les éléments résonnants de cette cellule donnent une bande stoppante aux ondes électromagnétiques incidentes avec la polarisation le long des bandes dipolaires.

La bande stoppante disparaîtra avec l'activation des diodes, conduisant ainsi à la caractéristique de transmission souhaitée à la fréquence de fonctionnement. Un circuit LC série équivalent est utilisé lors de simulations pour modéliser l'état OFF de chaque diode PIN (GMP4201) [20]. Ce circuit ne présente pas d'impact effectif sur la réponse de transmission du SSF. La résistance parasite de chaque diode peut être négligée dans l'état ON et peut être modélisée comme un conducteur parfait en ce même état. Malgré leur opération non linéaire, les diodes PIN à haute fréquence sont parmi les éléments actifs les plus utilisés pour la reconfiguration de la réponse électromagnétique d'une structure SSF. La Fig. 6-5 (a) montre le modèle de circuit électrique utilisé de la diode PIN GMP4201 lors de la simulation [23]. Pour le mode de polarisation d'état ON, la diode a une résistance faible, ce qui ne présente pas d'impact significatif sur la réponse souhaitée de la structure SSF. L'auto-inductance de la diode est négligée quand le mode de polarisation d'état est ON. Toutefois, lorsque ce mode est OFF, la capacité parasite présente un impact significatif sur la bande de fréquence de la surface en bande stoppante (stop-band). Il s'avère donc nécessaire de considérer son effet lors de la conception de la structure SSF dans un mode de polarisation de l'état OFF. La fréquence centrale de la cellule unitaire magnéto-diélectrique SSF est principalement indiquée par les longueurs de résonance des bandes dipolaires et des anneaux discontinus à résonateur à anneau fendu. La longueur effective du dipôle dans la cellule unitaire est d'environ une demi-onde à une fréquence égale à 2.45 GHz. Cette longueur effective est liée à la périodicité des cellules unitaires magnéto-diélectrique SSF ainsi qu'à la capacité parasite de la diode PIN dans l'état OFF. La valeur moyenne de l'anneau SRR résonnant est, d'autre part, d'environ une longueur d'onde à des fréquences autour de 2.45 GHz. Les autres dimensions de la cellule unitaire sont optimisées à l'aide du logiciel Ansoft HFSS en termes de la bande passante maximale de l'état de transmission (valeur est centrée à 2.45 GHz) ainsi que de la réflexion maximale des états ON et OFF. Nous étudions l'effet des dimensions de la cellule unitaire pour la configuration du pattern de rayonnement de l'antenne lors des suivantes.
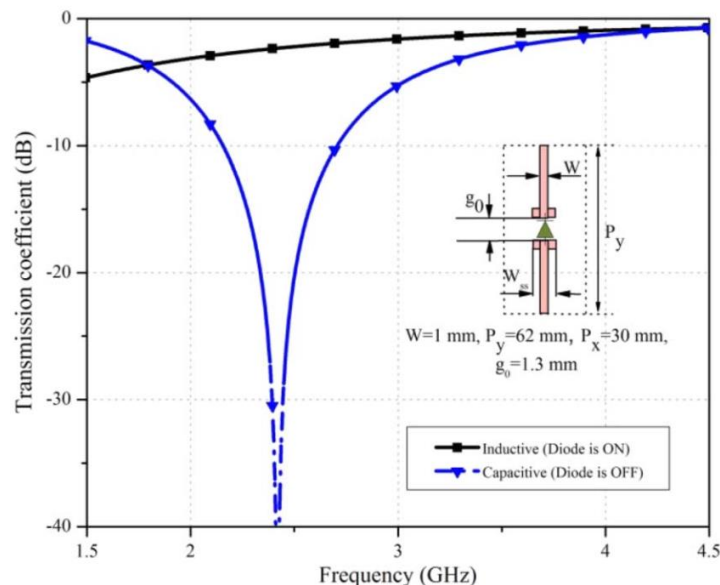
Fig. 6-1 Réponse de transmission d'un écran FSS actif constitué de bandes chargées capacitives discontinues.

(a

(b
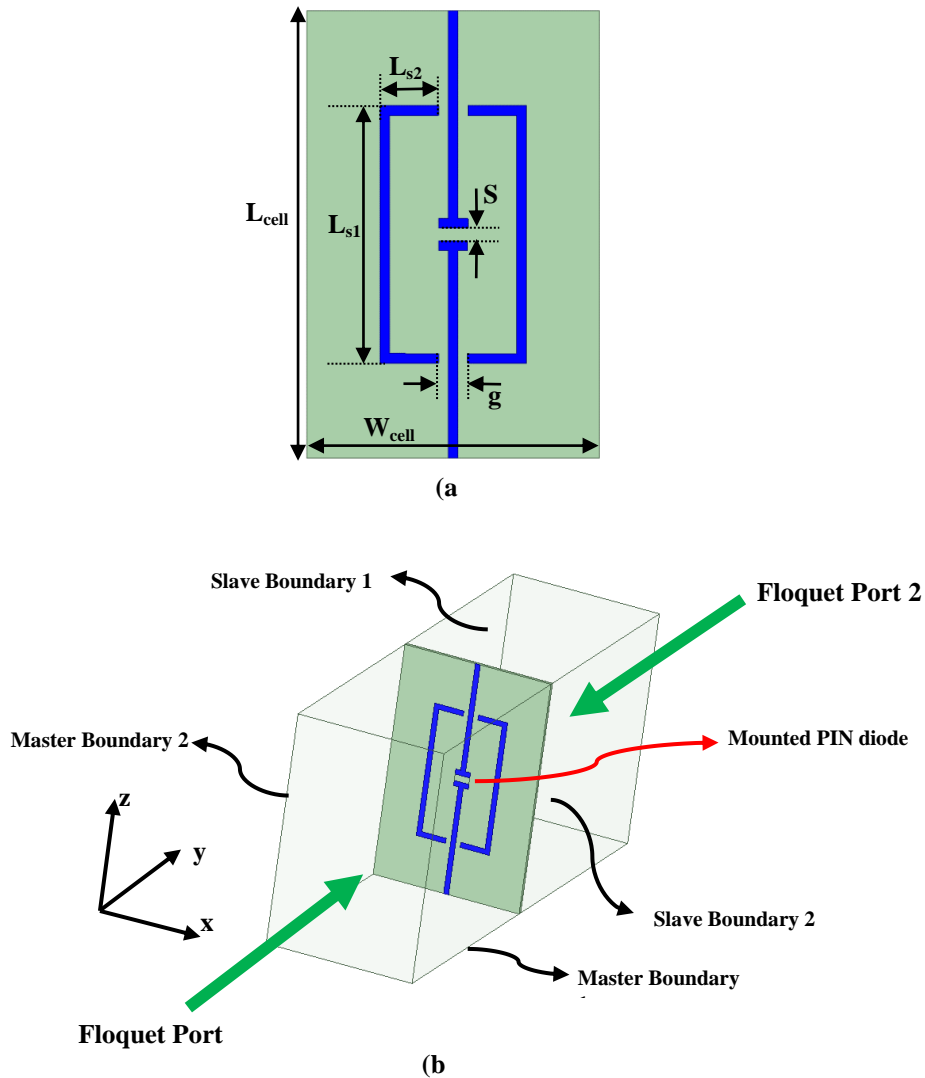
Fig. 6-2 (a) Dimensions de la cellule unitaire FSS diélectrique magnéto proposée. (b) Conditions limites particulières et définie l'excitation du port Floquet pour extraire les paramètres de diffusion. Les dimensions des cellules unitaires sont Lcell = 46, Wcell = 30, Ls1 = 26,5, Ls2 = 5, S = 1,3, g = 1, toutes en millimètre.
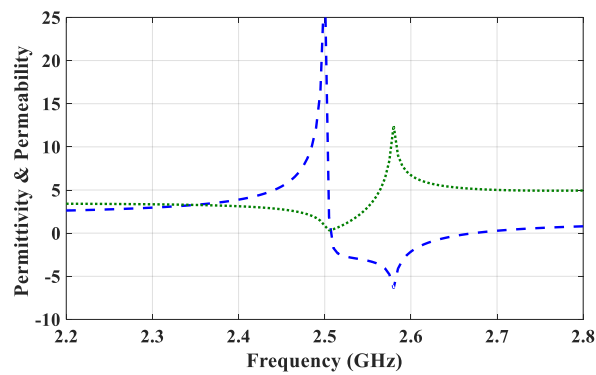
Fig. 6-3 Paramètres constitutifs efficaces de la paroi FSS magnéto-diélectrique.
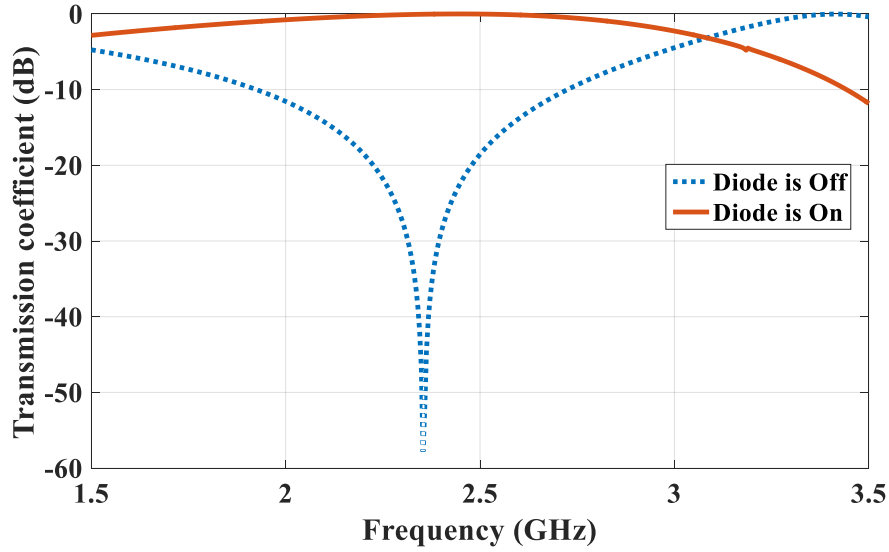
Fig. 6-4 Réponse de transmission du mur FSS magnéto-diélectrique.
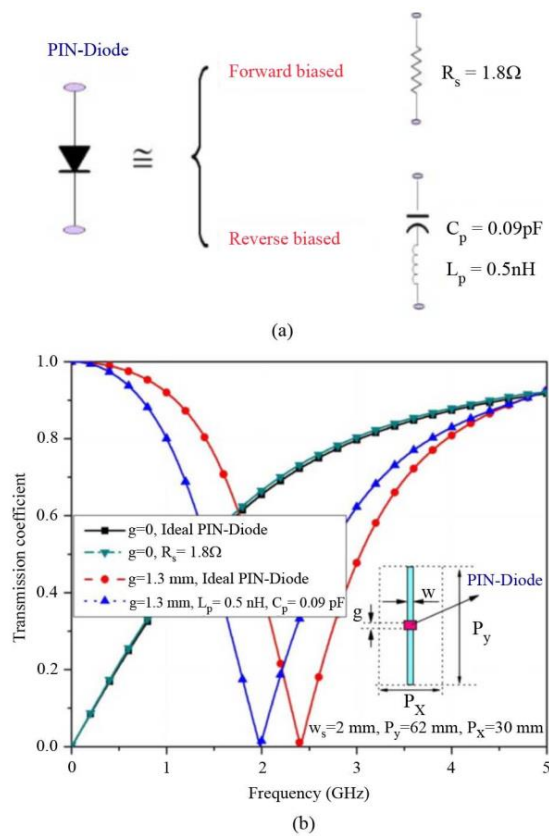
Fig. 6-5 Mode élément actif utilisé dans les simulations et son effet sur la réponse EM de la cellule unitaire des bandes discontinues. (a) Modèle actuel de circuit électrique à diode PIN utilisé dans la simulation. (b) Coefficient de transmission simulé des bandes discontinues

6. 3 Antenne de pattern omnidirectionnel

Nous présentons dans la Fig. 3-6 une antenne monopôle compacte. Il s'agit en fait d'une version simplifiée que celle présentée dans [24]. L'antenne monopôle proposée est sélectionnée en raison de ses caractéristiques de rayonnement omnidirectionnel à la fréquence de 2.45 GHz dans le plan azimut, ce qui la rend idéale pour une utilisation dans la conception de l'antenne de commutation de faisceau proposée. De plus, grâce à la simplicité de sa configuration, la fabrication de l'antenne monopôle s'avère être facile. L'antenne monopôle est constituée de deux éléments monopôles monté le cascade et de forme rectangulaire imprimés les uns sur les autres avec un petit plan GND à l'arrière du substrat. Les résonateurs supérieurs de l'antenne sont deux patches rectangulaires de différentes tailles, conçus pour opérer à 2.45 GHz. L'antenne proposée peut être alimentée directement par un câble coaxial de 50 Ω. Elle a été fabriquée sur un substrat RO3006 avec une permittivité relative de $\varepsilon_r = 6.15$ et une épaisseur de 1.27 mm. Les paramètres géométriques optimisés sont donnés comme suit: b1 = 12 mm, a1 = 12 mm, b2 = 9 mm, a2 = 10 mm, a3 = 4.6 mm et b3 = 7 mm. Les coefficients de réflexion simulés sont représentés sur la Fig. 6-7. Nous pouvons déduire que les résultats mesurés s'accordent avec les simulations. Un changement de fréquence négligeable est dû principalement aux tolérances de fabrication. Nous présentons les diagrammes de rayonnement de l'antenne monopôle proposée à la Fig. 6-8.
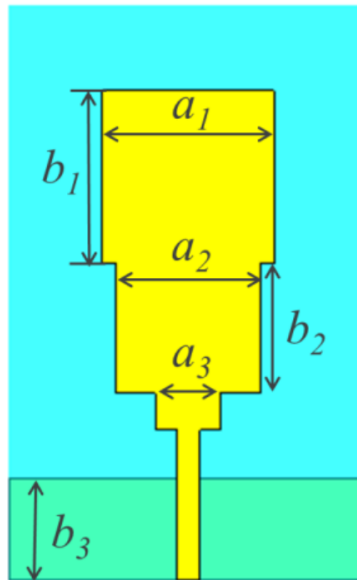
Fig. 6-6 Géométrie de l'antenne monopôle omnidirectionnelle proposée.
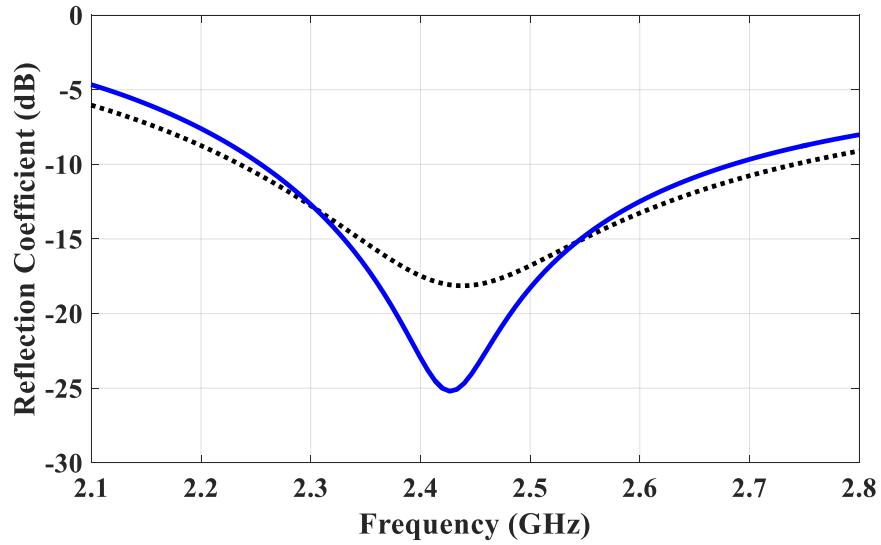
Fig. 6-7 Les coefficients de réflexion simulés et mesurés résultent de l'antenne monopôle omnidirectionnelle proposée
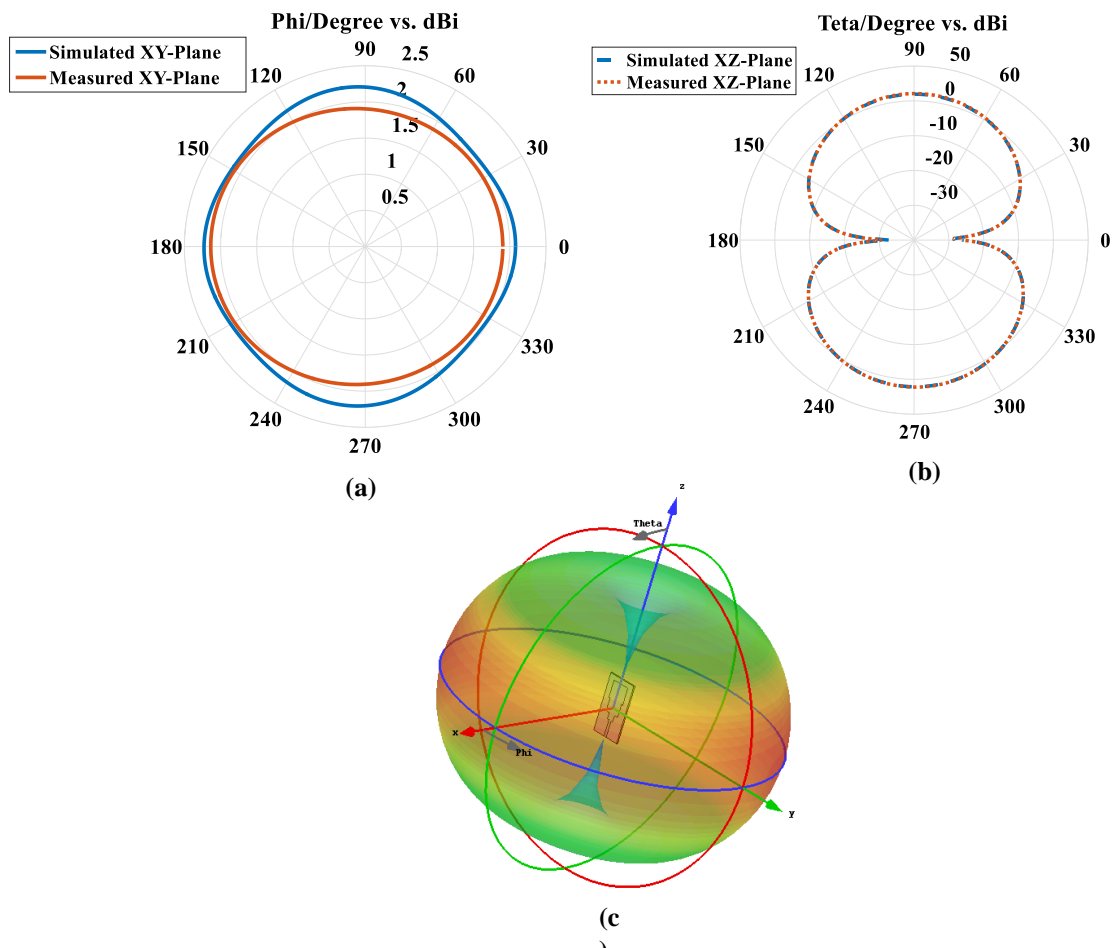
Fig. 6-8 Modèle de rayonnement simulé et mesuré de l'antenne monopôle omnidirectionnelle proposée à 2.45 GHz.

6. 4 Pattern proposé - Antenne reconfigurable utilisant une SSF active

Nous présentons dans la Fig. 6.9 le diagramme de l'antenne reconfigurable proposée. Puisque le mécanisme de rayonnement de cette antenne est basé sur le principe des antennes à réflecteur, ses dimensions physiques globales sont tout d'abord calculées en utilisant la structure disponible du réflecteur, qui représente en fait une antenne octogonale à réflecteur de coin. Selon la taille physique calculée du réflecteur cylindrique et de son mécanisme de réflexion, un réflecteur solide semi-cylindrique est adapté au réflecteur de coin octogonal afin de calculer et d'évaluer la taille appropriée de l'antenne SSF active octogonale à réflecteur de coin. Nous considérons en conséquence le mécanisme de rayonnement présenté dans la Fig. 6.10, où la source d'excitation est placée sur l'axe du réflecteur solide semi-cylindrique, à une distance de rayon R. Comme nous le savons, selon la distance entre le dipôle et le réflecteur solide semi-cylindrique, les ondes réfléchies des structures latérales de la SSF active octogonal à réflecteur de coin peuvent être en phase. Cette distance contrôle également les niveaux des lobes secondaires, des lobes latéraux et du lobe arrière du diagramme de rayonnement ainsi que la résistance au rayonnement de l'antenne SSF active octogonale à réflecteur de coin [25]. En conséquence, selon la position centrale R de la source d'excitation, différentes positions de conception peuvent être choisies avec un pattern de rayonnement directif optimal. Dans ce travail, un dipôle omnidirectionnel est placé en première place afin d'atteindre les dimensions minimales de la SSF active octogonale à réflecteur de coin. Cela réduira les éléments actifs requis et le coût de fabrication du réflecteur reconfigurable. Par conséquent, la distance d'antenne à partir de la SSF octogonale active à réflecteur de coin est choisie dans un intervalle de 0.25-0.7 λo, où λo est la longueur d'onde dans l'espace libre à la fréquence de fonctionnement. Pour cette SSF octogonale active à réflecteur de coin, la largeur d'aperture $W_{aperture}=2R$ est suffisamment grande pour réfléchir les parties principales des ondes qui contribuent au lobe principal du diagramme de rayonnement [25]. En outre, l'opération principale du réflecteur est de reflechir une onde rayonnée du dipôle, parallèlement à ses axes. Par conséquent, la partie principale des ondes rayonnées du dipôle à son centre sera réfléchie le long de l'axe de la SSF active octogonale à réflecteur de coin. En fait, cette SSF active octogonale à réflecteur de coin fournit une caractéristique de rayonnement similaire à un réflecteur solide semi-cylindrique avec un rayon de dimension R. La hauteur du réflecteur est choisie de telle façon à être supérieure au dipôle de la source rayonnante; ceci est dans le but de réduire le rayonnement arrière au niveau du plan E. Par conséquent, L_{wall} est choisi supérieur à la longueur d'onde, et selon la périodicité de la cellule unitaire, il est choisi de manière à consister en trois cellules unitaires. Le nombre des cellules unitaires dans chacune des panneaux du réflecteur est également sélectionné en fonction de la périodicité de la cellule unitaire et du rayon du rayon de la SSF active octogonale à réflecteur du coin. En conséquence, un panneau de 2×3 cellules unitaires est choisi de façon à être intégré dans chaque frontière du réflecteur; ce qui montre également le nombre d'étapes de commutation pour le diagramme de rayonnement afin de supporter tous les angles d'Azimut dans les 8 panneaux ou secteurs; tel que montré dans la Fig.1-7.
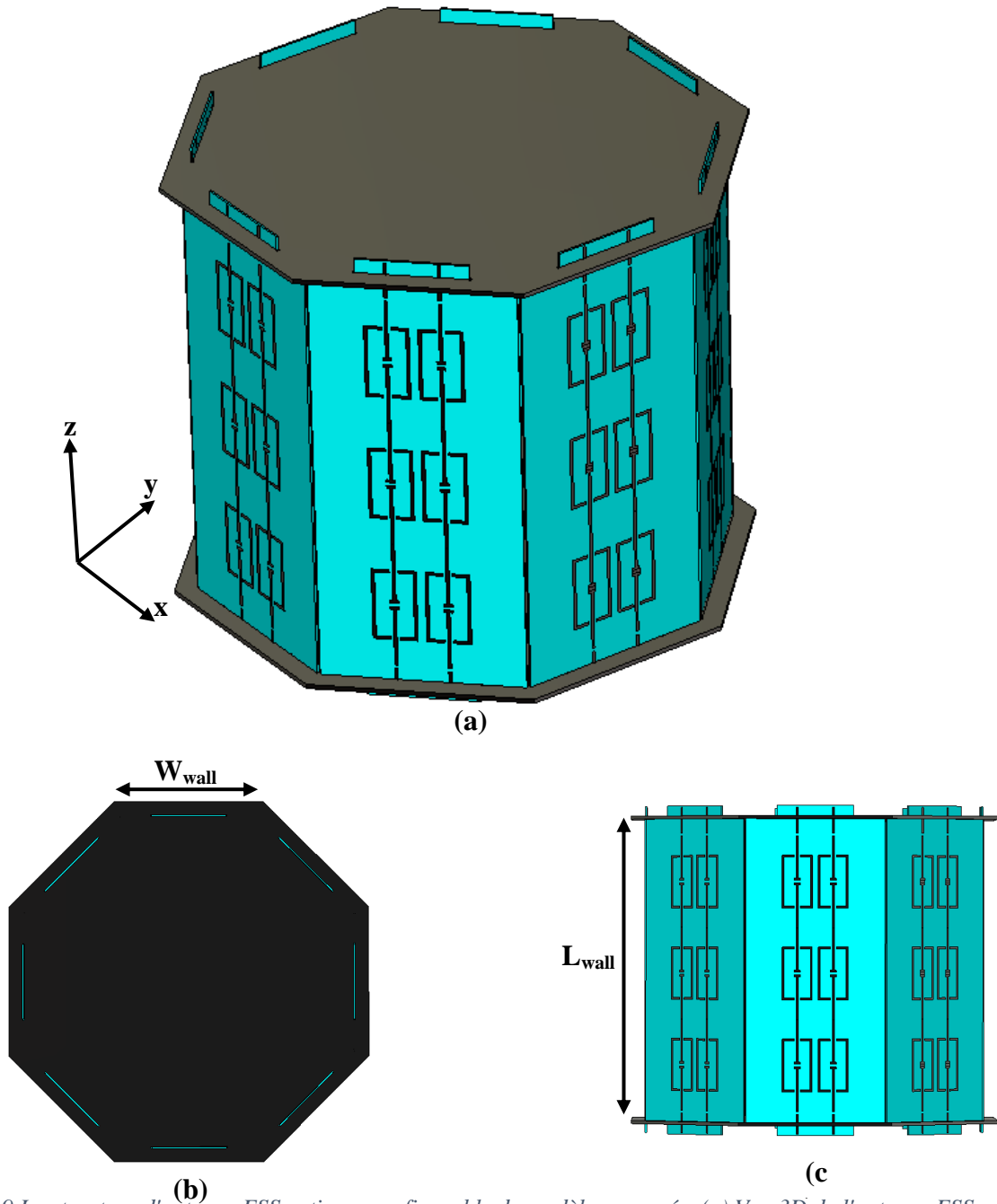
Fig. 6-9 La structure d'antenne FSS active reconfigurable de modèle proposée. (a) Vue 3D de l'antenne FSS active reconfigurable de modèle proposée. (b) Vue de dessus. Vue de côté.
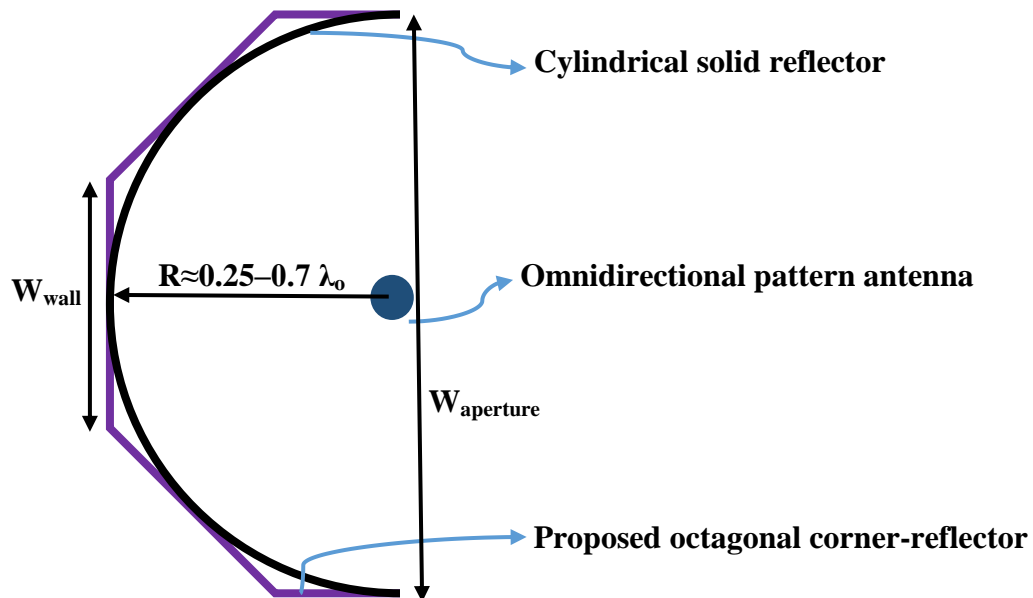
Fig. 6-10 Géométrie des antennes à réflecteur cylindrique et réflecteur FSS.

La Fig. 6-11 montre les résultats de simulation du coefficient de réflexion, réalisés à l'aide du logiciel HFSS pour les géométries de l'antenne, représentées dans les Fig. 6-9. Les dimensions finales de l'antenne SSF, active octogonale à réflecteur de coin, utilisées dans les simulations sont présentées dans la Fig. 6-9. Les dimensions des cellules unitaires ont été présentées dans la Fig. 6-2. Les courbes de coefficient de réflexion montrent que toutes les antennes offrent une bande correspondante autour de 2.45 GHz. D'autre part, comme la réponse de transmission de l'écran SSF dépend de la fréquence, la bande passante de l'antenne SSF à réflecteur semi-cylindrique est un peu plus petite que celle de l'antenne SSF active octogonale à réflecteur de coin. Cela signifie que pour l'antenne SSF octogonale active à réflecteur de coin, l'impédance d'entrée du dipôle avec modèle omnidirectionnel est davantage affectée par la SSF active octogonale à réflecteur de coin. Le réflecteur de coin avec une ouverture $W_{aperture}$, illustré à la Fig. 6-10, donne le gain le plus élevé. Comme nous l'avons prédit, un réflecteur solide semi-cylindrique avec une ouverture équivalente présente une courbe de gain similaire à celle d'une SSF active octogonale à réflecteur de coin avec la même ouverture. Le gain de l'antenne SSF active octogonale à réflecteur de coin dépend cependant de la fréquence. Sa dimension physique est légèrement plus grande que celle avec un réflecteur solide semi-cylindrique. Mentionnons ici que l'avantage unique de l'antenne SSF active octogonale à réflecteur de coin est l'augmentation de la directivité de l'antenne. Cela montre qu'un compromis entre le gain maximal et celui correspondant devrait être effectué. Le mécanisme de rayonnement prévu de l'antenne est confirmé avec succès en étudiant ses diagrammes de rayonnement, illustrés à la Fig.6-12.

Comme nous pouvons le déduire, le diagramme de rayonnement de l'antenne proposée est presque identique aux performances des réflecteurs cylindriques solides en termes des lobes arrières/latéraux.

La procédure et les lignes directrices de conception de l'antenne SSF active octogonale à réflecteur de coin proposée, basées sur les principes de l'antenne de réflecteur, peuvent être résumées comme suit:

➢ la fréquence de l'antenne est sélectionnée selon le mécanisme de reconfiguration requis à la fréquence de fonctionnement souhaitée, soit 2.45 GHz pour le présent projet;

➢ le rayon de la SSF active octogonale à réflecteur de coin est choisi dans l'intervalle de 0.25–0.7 λ_o, où λ_o est la longueur d'onde de l'espace libre;

➢ le nombre de cellules unitaires sur chaque frontière est calculé selon la valeur de périodicité de la cellule unitaire conçue;

➢ la hauteur de la SSF active octogonale à réflecteur de coin doit être supérieure à une longueur d'onde. Par conséquent, afin d'obtenir la taille minimale pour l'antenne avec le diagramme de rayonnement désiré, nous considérons trois cellules unitaires le long de l'axe de la SSF active octogonale à réflecteur de coin;

➢ les valeurs initiales du rayon de l'antenne octogonale active SSF à réflecteur de coin doivent être légèrement ajustées; ceci est dû principalement au couplage entre l'antenne omnidirectionnelle illuminante et la SSF active octogonale à réflecteur de coin. Le rayon doit être choisi dans un intervalle de 0.25-0.7 λ_o afin d'assurer une bande passante minimale de 10%;

➢ les dimensions de l'antenne sont finalement optimisées en utilisant le logiciel HFSS pour le diagramme de rayonnement désiré ainsi que les performances correspondantes.
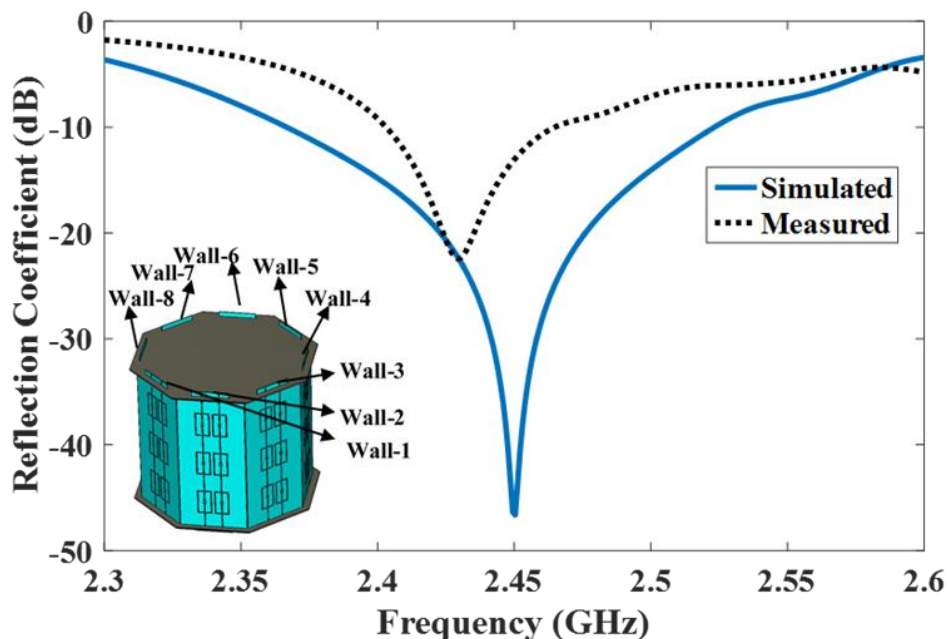
Fig. 6-11 Les résultats des coefficients de réflexion simulés et mesurés, réalisés pour les géométries d'antennes FSS actives de coin-réflecteur d'angle proposées, représentées sur les Figs. 6-9. Les murs 1, 2 et 3 sont actifs.

(a)   (b)

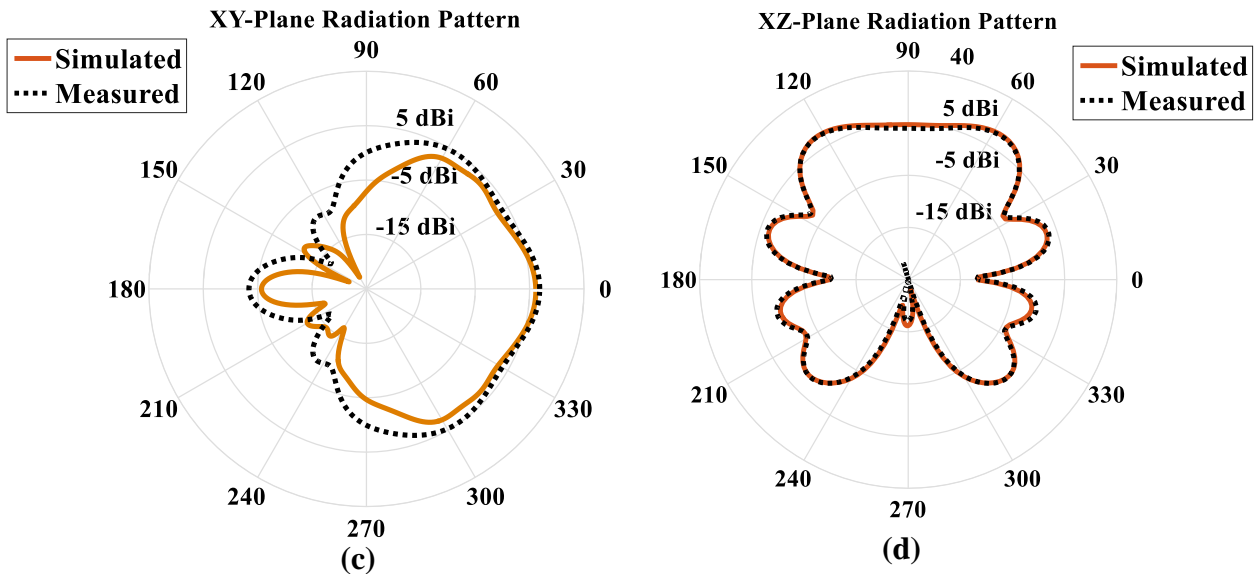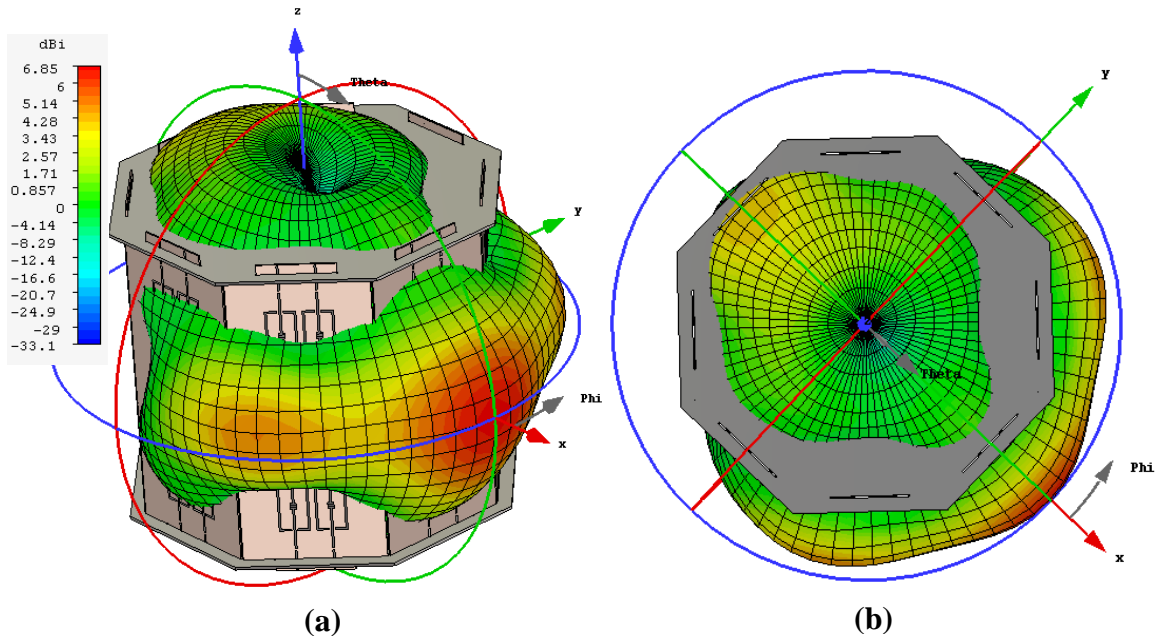(c)   (d)

Fig. 6-12 Des résultats de diagramme de rayonnement simulés et mesurés, réalisés pour les géométries d'antennes FSS activées par le réflecteur de coin octogonal proposé, représentées sur les Figs. 6-9. Les murs 1, 2 et 3 sont actifs.

# 6. 5 Résultats mesurés de l'antenne reconfigurable proposée

La Fig. 6-13 présente une photographie du prototype proposé de l'antenne SSF active octogonale à réflecteur de coin selon les dimensions fournies lors des sections précédentes. Une antenne omnidirectionnelle simple est utilisée comme antenne de base pour éclairer les structures comme expliqué dans la section 6.3. L'antenne monopole est constituée de deux éléments monopoles rectangulaires montés au cascade avec un petit plan de masse à l'arrière du substrat. Les principaux résonateurs de l'antenne sont deux éléments rectangulaires de différentes tailles, conçus pour opérer aux alentours de 2.45 GHz. L'antenne proposée peut être alimentée directement par une ligne de transmission coaxiale de 50 Ω. De plus, les diodes PIN à haute fréquence, polarisées avec un réseau d'alimentation DC, sont connectées aux bornes des structures SSF en utilisant des inducteurs à bobines d'arrêt RF (RF-Chock), comme indiqué dans la Fig. 6-13. Les bobines d'arrêt RF séparent le réseau d'alimentation de polarisation de l'écran SSF sur la bande passante souhaitée de l'antenne. Ils bloquent la fuite du signal RF vers le circuit de l'unité de contrôle. La mousse rigide est utilisée comme un support pour maintenir l'antenne omnidirectionnelle d'alimentation au milieu du cylindre.

Afin d'examiner les performances de la conception proposée, les pertes de retour de l'antenne sont mesurées dans un premier lieu. Certaines mesures ont été ensuite réalisées pour le diagramme de rayonnement du plan H de l'antenne dans le but de trouver le meilleur diagramme de rayonnement en termes du faisceau principal désiré, du gain réalisé, de lobe latéral et des niveaux du lobe arrière. D'autres modèles sont finalement mesurés afin d'évaluer les performances de rayonnement dans l'autre plan. La Fig. 6-14 montre les résultats mesurés du prototype de l'antenne SSF active octogonale à réflecteur de coin, comparés à ceux simulés. Comme nous pouvons le remarquer, l'antenne omnidirectionnelle à bande large fonctionne de façon efficace de 2.25 GHz à 2.7 GHz. Toutefois, lorsqu'elle est placée au centre de la SSF cylindrique, elle opère efficacement de 2.35 GHz à 2.55 GHz. La perte de retour mesurée pour cette structure démontre une correspondance plus faible par rapport à la simulation (de 2.4 GHz à 2.5 GHz). De plus, le fait de désactiver les diodes entraîne un léger décalage de la courbe de perte de retour, ceci a effectivement été prédit par les simulations. Ses diagrammes de rayonnement des plans E et H à la fréquence 2.45 GHz sont comparés à ceux des résultats de simulation de l'antenne SSF octogonale à réflecteur de coin. Une certaine asymétrie est remarquée dans les plans E et H de l'antenne omnidirectionnelle, principalement en raison du câble RF et du connecteur SMA utilisés dans l'implémentation de l'antenne (voir la Fig. 6-8). Cependant, son diagramme de plan H est presque uniformément rayonnant sur tous les angles. Les diagrammes de rayonnement, des plans E et H, mesurés démontrent la meilleure performance à la fréquence 2.45 GHz, ce qui confirme en validité du concept proposé. Il est claire que la configuration proposée peut fournir un diagramme de rayonnement directionnel avec un niveau de lobe arrière supérieur à -20dB et -17dB respectivement pour les diagrammes de plan H et E. En raison de la diffusion des ondes du bord d'ouverture, ce niveau est un peu dégradé comparativement aux autres angles dans le plan arrière. Comme nous l'avons prévu, les lignes d'alimentation DC parallèles affectent le diagramme du plan H. Le gain d'antenne a été mesuré à l'aide de la méthode de comparaison de mesure du gain. Ce gain peut être calculé à

partir de l'expression (5-3), dans laquelle PAUT est la puissance reçue par l'antenne sous test. PSTD et GSTD sont respectivement la puissance reçue et le gain de l'antenne cornet standard.
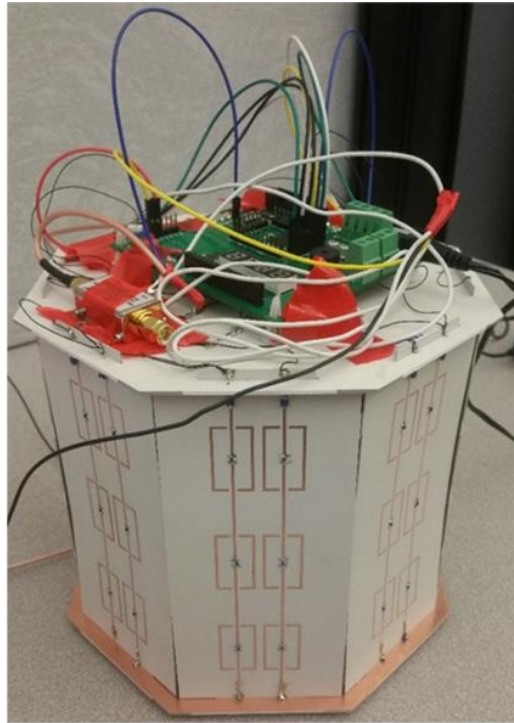
(a)
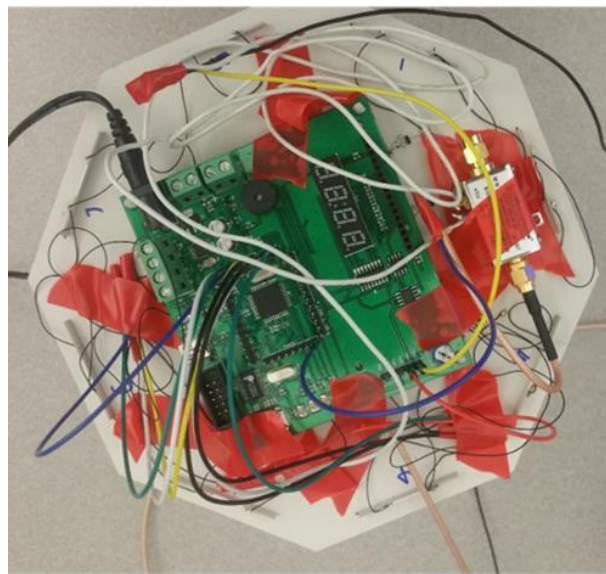
(b)

Fig. 6-13 Photo du prototype de l'antenne FSS activé à l'angle octogonale de l'invention.

$$G_{AUT} = G_{STD}P_{AUT} - P_{STD} \qquad (all\ units\ are\ in\ dB) \qquad\qquad (23)$$

La Fig. 6-14 montre les gains mesurés pour l'antenne à 2.45 GHz. À partir de cette figure, nous pouvons remarquer que l'antenne est capable d'offrir un diagramme de rayonnement directif avec un gain supérieur à 5 dB aux alentours de la fréquence de fonctionnement. La différence entre les résultats mesurés et ceux de la simulation est due à l'inexactitude de la conception et de la mesure.

L'antenne proposée, connue sous le nom d'antenne sous test (AUT), agit comme une antenne de récepteur (R_x) pour tester la capacité de l'antenne à recevoir le signal de l'émetteur (T_x) et à vérifier la direction de l'émission selon la puissance du signal reçu (P_r). Cela se fera en tournant la structure dans les 8 différentes directions à l'aide de l'unité de contrôle et en mesurant la puissance reçue dans différentes directions. En comparant les valeurs de la puissance reçue à différentespositions, nous pouvons prédire la direction de l'émission par rapport au récepteur. Nous avons ici une certaine limitation de mesures que nous devrions considérer afin d'effectuer une mesure valide.

La mesure du signal reçu (P_r) est tout d'abord effectuée lorsque les distances entre T_x et R_x varient de 1 m à 3 m. Si nous augmentons la distance entre T_x et R_x, nous ne serions pas capable de mesurer la puissance reçue du fait qu' au niveau de l'unité de contrôle, le détecteur de puissance RF (avec numéro de pièce: ZX47-60LN+) a une portée dynamique de -60 dBm à +10dBm, comme indiqué sur la fiche technique du composant de la Fig.6-15. La Fig.6-16 illustre la perte de propagation de l'espace libre entre deux antennes cornets. La Fig. 6-18 montre la photo de la configuration du test de mesure de l'antenne. Dans le présent travail, les mesures ont été effectuées sous les conditions d'une chambre aréchoïque (7.95 m $\times$ 3.17 m) dans le laboratoire du Groupe de recherche des antennes. La propagation pratique à l'intérieur a été, tout d'abord, effectuée dans une chambre aréchoïque à 1.6 m de distance entre T_x et R_x. Toutefois, à une distance supérieure à 1.5 m, ce test n'est plus applicable en raison du fait que nous n'avons pas de chaîne de récepteur pour AUT en dehors de la chambre pour évaluer les différents utilisateurs. Lors des mesures intérieures, les fréquences réelles des résultats expérimentaux de perte de retour, soit 2.45 GHz, sont utilisées pour injecter le signal au générateur de signal RF.

La mesure sur l'AUT a été effectuée dans une direction fixe. La configuration de mesure de l'antenne pratique à l'intérieur est illustrée dans la Fig. 6-17. Les deux AUT doivent être placées face à face et alignées l'une vers l'autre pour obtenir une condition LOS. Sur le côté gauche, le générateur de signal a été utilisé pour injecter le signal RF à l'AUT, tandis que l'équipement sur le côté droit est une antenne réceptrice connectée à l'analyseur de spectre. Théoriquement, la perte du target (Path loss, P_L) par rapport à la distance entre T_x et R_x est décrite dans le modèle de propagation par réflexion au sol (deux rayons) [26], comme indiqué dans [24].

$$P_L = 32.44 + [20\log(d)] + [20\log(f)] - G_T - G_R + [T_{other\ losses}] \qquad\qquad (24)$$

Où *d* est la distance (en km), *f* est la fréquence (en MHz), G_T est le gain de l'émetteur (en dBi), G_R est le gain du récepteur (en dBi), et les pertes $T_{other\ losses}$ comprennent le plancher et la frontière [26]. La valeur du gain G_R réfère à l'AUT pendant la simulation et la valeur du gain G_T réfère à l'antenne cornet avec un gain de 10 dBi. Le signal diminue quand la distance entre T_x et R_x augmente. La puissance reçue calculée est de -50dBm pour une distance de 1.6 m entre T_x et R_x. Si Nous augmentons la distance, le détecteur de puissance RF ne serait pas capable de mesurer efficacement la puissance du récepteur. Nous choisissons donc une distance de 1.6 m entre T_x et R_x.
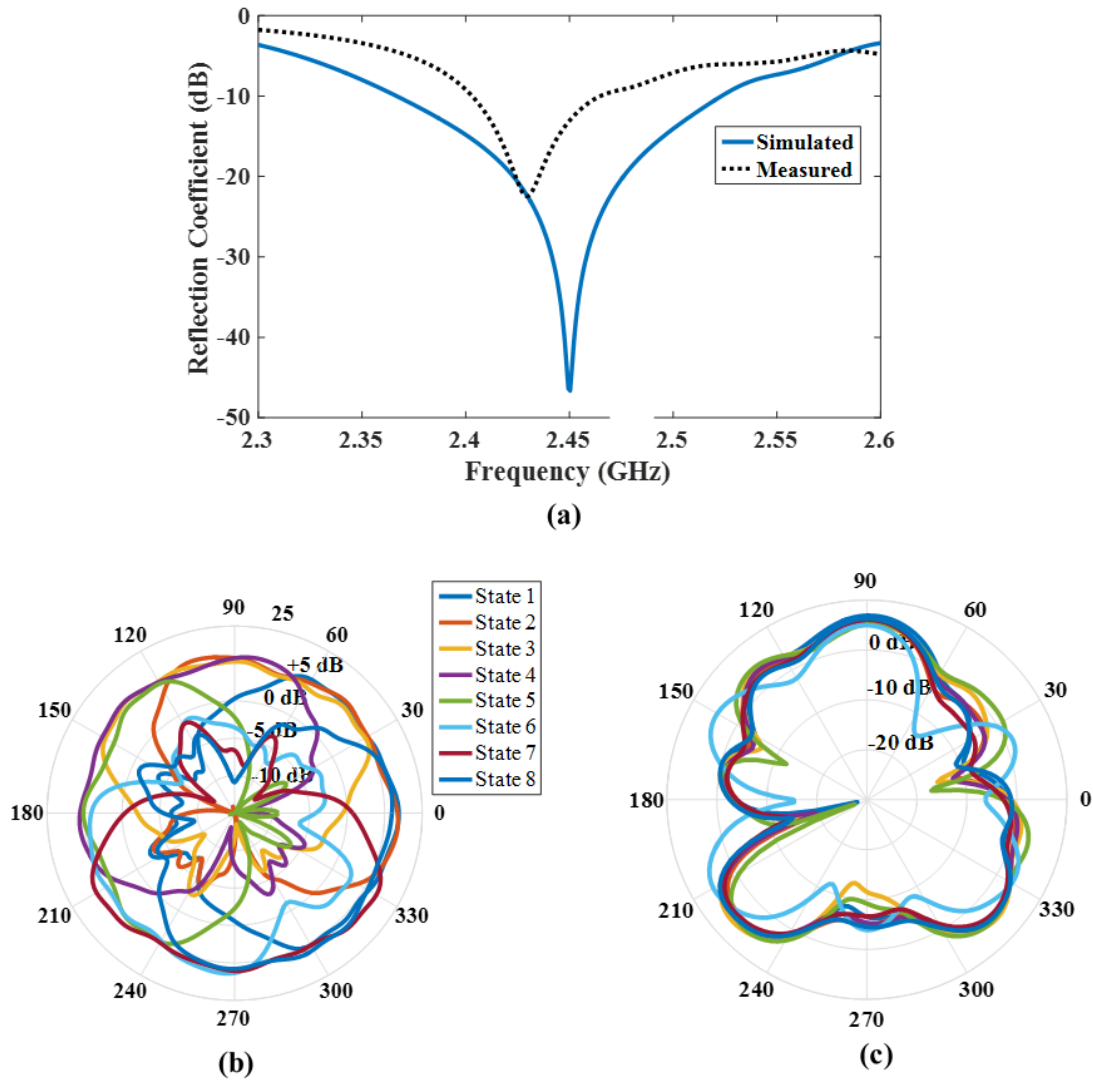
Fig. 6-14 Résultats mesurés pour l'antenne FSS active du réflecteur angulaire octogonale (a) Coefficient de réflexion. (B) diagramme de rayonnement du plan H. (C) diagramme de rayonnement en plan E.

(a)

(b)
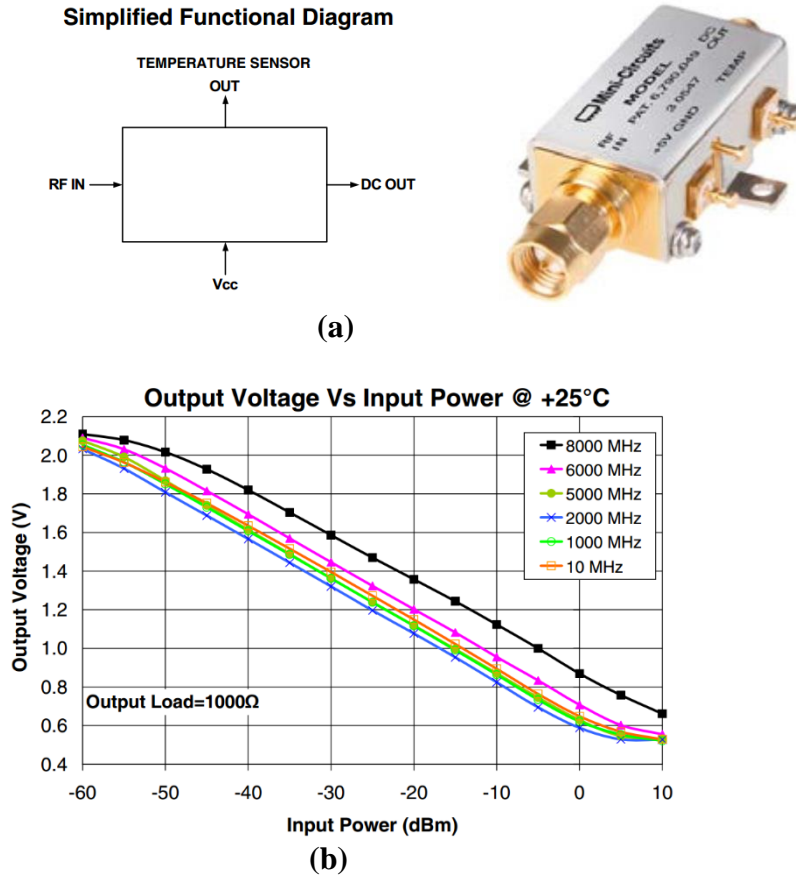
Fig. 6-15 Tension de sortie Vs Puissance d'entrée pour le détecteur de puissance RF (avec numéro de pièce: ZX47-60LN+).
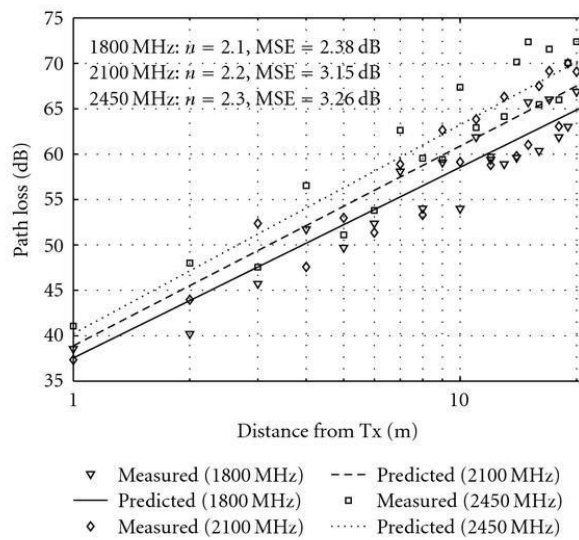
Fig. 6-16 Perte de propagation de l'espace libre avec une antenne à deux canaux par rapport à la distance.
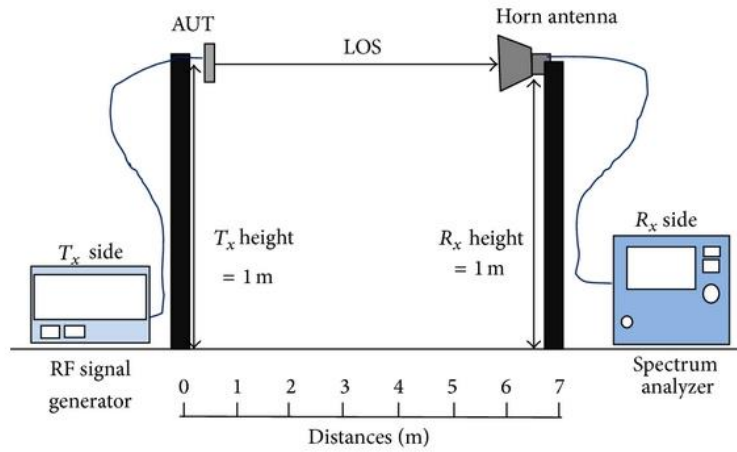
Fig. 6-17 La configuration pratique de la mesure de l'antenne.
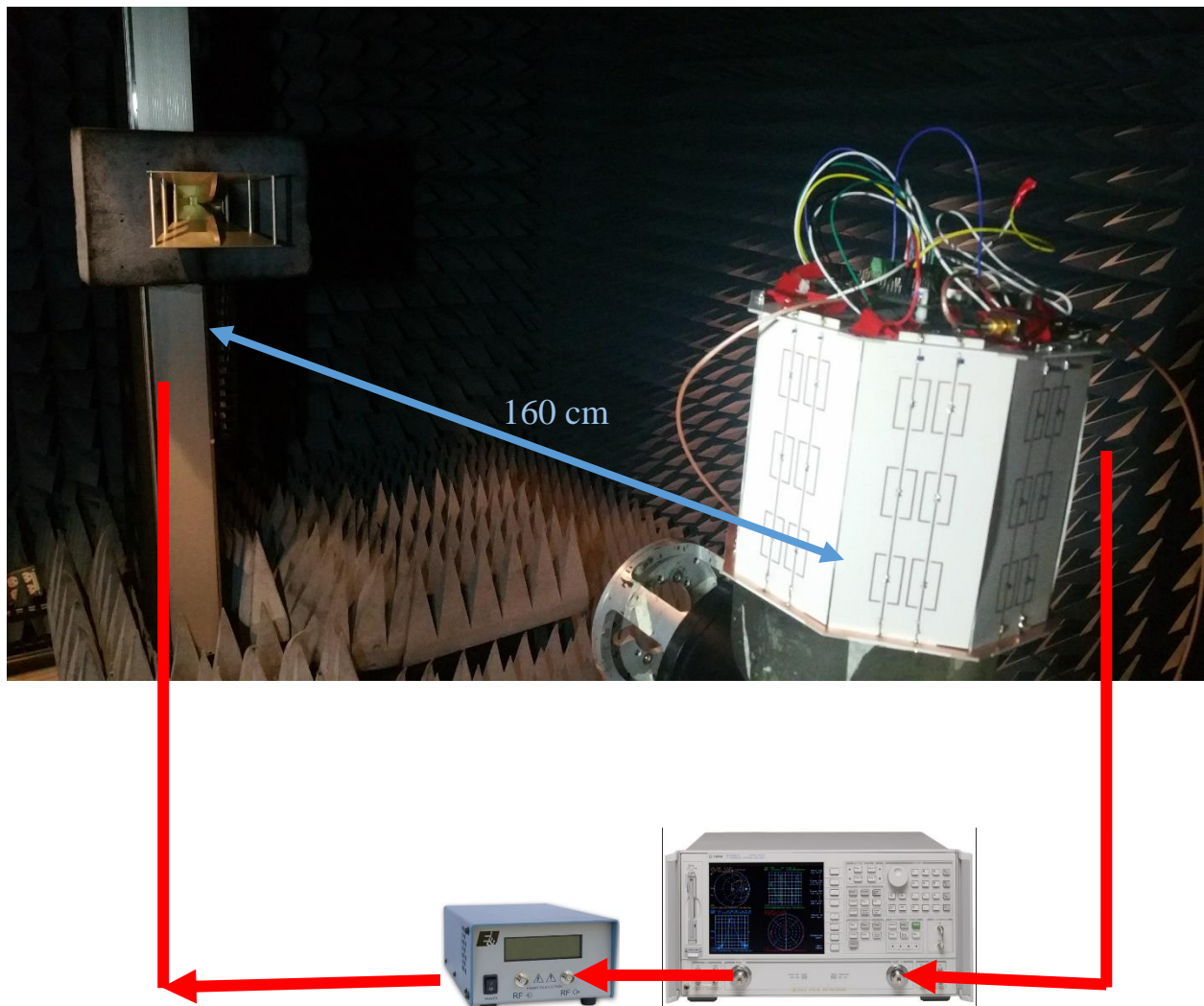
Fig. 6-18 Photo de la configuration de la mesure de l'antenne.

Nous illustrons dans le Tableau 1 les données de gain; gain supplémentaire (additional gain, AG); comparés aux dipôles, largeur du faisceau de 3 dB (3 dB-BW), niveau du lobe latéral (SLL) et le ratio FBR (front-back ratio). Le gain supplémentaire atteint 3.61 dB à 2.45 GHz, et est supérieur à 4.44 dB à 2.4 GHz. La largeur du faisceau de 3 dB est de 27° à 34°. Une autre différence significative entre cette antenne et celles mentionnées dans [19-21] est qu'un niveau très profond de 'nulling' peut être atteint. Nous avons alterné l'objectif du programme pour atteindre un niveau de lobe latéral plus petit au niveau du plan H.

Table 2: Sondage de l'antenne FSS active de réflecteur angulaire octogonal.

Freq (GHz)	Gain (dBi)	AG (dB)	3dB-BW (degree)	SLL (dBi)	FER (dB)
2.4	5.45	4.44	27	3.49	17
2.45	5.3	3.61	26	4.1	20
2.5	5.1	3.53	34	3.54	18

6. 6 Conclusion

Dans notre projet, nous avons proposé une antenne SSF active octogonale à réflecteur de coin, hautement agile. L'antenne est orientable et directive en permanence. Elle surpasse de nombreuses configurations de SSF basées sur les diodes PIN. Les résultats mesurés ont atteint un gain supplémentaire allant jusqu'à 3.61 dB et un niveau profond de '*nulling'* de -20 dBi. Les largeurs du faisceau de -3 dB sont de 27 ° à 34 °, elles peuvent offrir une résolution de balayage de 1°. La mesure de la bande passante du faisceau montre qu'il peut offrir un mode de gain élevé stable pour une bande WiFi de 2.45 GHz.

Appendix 1

The C++ code program of the MCU (micro controller unit):

```cpp
#ifndef F_CPU
#define F_CPU 12000000UL // 12 MHz clock speed
#endif
/////////////////////////////////////////////////////////////////////////////////////////////////
#define D0 eS_PORTB0
#define D1 eS_PORTB1
#define D2 eS_PORTB2
#define D3 eS_PORTB3
#define D4 eS_PORTB4
#define D5 eS_PORTB5
#define D6 eS_PORTB6
#define D7 eS_PORTB7
#define RS eS_PORTD2
#define EN eS_PORTD4
/////////////////////////////////////////////////////////////////////////////////////////////////
#include <avr/io.h>
#include <stdio.h>
#include <stdlib.h>
#include <util/delay.h>
#include "lcd.h"
/////////////////////////////////////////////////////////////////////////////////////////////////
// Voltage Reference: Int., cap. on AREF
#define ADC_VREF_TYPE ((1<<REFS1) | (1<<REFS0) | (1<<ADLAR))
// Read the 8 most significant bits
// of the AD conversion result
unsigned char read_adc(unsigned char adc_input)
{
        ADMUX=adc_input | ADC_VREF_TYPE;
        // Delay needed for the stabilization of the ADC input voltage
        _delay_us(10);
        // Start the AD conversion
        ADCSRA|=(1<<ADSC);
        // Wait for the AD conversion to complete
        while ((ADCSRA & (1<<ADIF))==0);
        ADCSRA|=(1<<ADIF);
        return ADCH;
}
/////////////////////////////////////////////////////////////////////////////////////////////////
int main(void)
{
        // Declare your local variables here
        int temp1;
        float temp2;
        float temp3;
        char power[20];
/////////////////////////////////////////////////////////////////////////////////////////////////
        // Input/Output Ports initialization
        // Port A initialization
        // Function: Bit7=In Bit6=In Bit5=In Bit4=In Bit3=In Bit2=In Bit1=In Bit0=In
        DDRA=(0<<DDA7) | (0<<DDA6) | (0<<DDA5) | (0<<DDA4) | (0<<DDA3) | (0<<DDA2) | (0<<DDA1) |
(0<<DDA0);
        // State: Bit7=T Bit6=T Bit5=T Bit4=T Bit3=T Bit2=T Bit1=T Bit0=T
```

```
        PORTA=(0<<PORTA7) | (0<<PORTA6) | (0<<PORTA5) | (0<<PORTA4) | (0<<PORTA3) | (0<<PORTA2) |
(0<<PORTA1) | (0<<PORTA0);

        // Port B initialization
        // Function: Bit7=out Bit6=out Bit5=out Bit4=out Bit3=out Bit2=out Bit1=out Bit0=out
        DDRB=(1<<DDB7) | (1<<DDB6) | (1<<DDB5) | (1<<DDB4) | (1<<DDB3) | (1<<DDB2) | (1<<DDB1) |
(1<<DDB0);
        // State: Bit7=T Bit6=T Bit5=T Bit4=T Bit3=T Bit2=T Bit1=T Bit0=T
        PORTB=(0<<PORTB7) | (0<<PORTB6) | (0<<PORTB5) | (0<<PORTB4) | (0<<PORTB3) | (0<<PORTB2) |
(0<<PORTB1) | (0<<PORTB0);

        // Port C initialization
        // Function: Bit7=In Bit6=In Bit5=In Bit4=In Bit3=In Bit2=In Bit1=In Bit0=In
        DDRC=(0<<DDC7) | (0<<DDC6) | (0<<DDC5) | (0<<DDC4) | (0<<DDC3) | (0<<DDC2) | (0<<DDC1) |
(0<<DDC0);
        // State: Bit7=T Bit6=T Bit5=T Bit4=T Bit3=T Bit2=T Bit1=T Bit0=T
        PORTC=(0<<PORTC7) | (0<<PORTC6) | (0<<PORTC5) | (0<<PORTC4) | (0<<PORTC3) | (0<<PORTC2) |
(0<<PORTC1) | (0<<PORTC0);

        // Port D initialization
        // Function: Bit7=In Bit6=In Bit5=In Bit4=out Bit3=out Bit2=out Bit1=In Bit0=In
        DDRD=(0<<DDD7) | (0<<DDD6) | (0<<DDD5) | (1<<DDD4) | (1<<DDD3) | (1<<DDD2) | (0<<DDD1) |
(0<<DDD0);
        // State: Bit7=T Bit6=T Bit5=T Bit4=T Bit3=T Bit2=T Bit1=T Bit0=T
        PORTD=(0<<PORTD7) | (0<<PORTD6) | (0<<PORTD5) | (0<<PORTD4) | (0<<PORTD3) | (0<<PORTD2) |
(0<<PORTD1) | (0<<PORTD0);
        /////////////////////////////////////////////////////////////////////////////////////////////////
  // ADC initialization
  // ADC Clock frequency: 750.000 kHz
  // ADC Voltage Reference: Int., cap. on AREF
  // ADC Auto Trigger Source: Free Running
  // Only the 8 most significant bits of
  // the AD conversion result are used
  ADMUX=ADC_VREF_TYPE;
  ADCSRA=(1<<ADEN) | (0<<ADSC) | (1<<ADATE) | (0<<ADIF) | (0<<ADIE) | (1<<ADPS2) | (0<<ADPS1) |
(0<<ADPS0);
  SFIOR=(0<<ADTS2) | (0<<ADTS1) | (0<<ADTS0);
        /////////////////////////////////////////////////////////////////////////////////////////////////
  // Alphanumeric LCD initialization
        Lcd8_Init(16);
        Lcd8_Clear();
        /////////////////////////////////////////////////////////////////////////////////////////////////
        while (1)
        {
                // Place your code here
                temp1=read_adc(0);
                temp2=temp1/255;
                temp3=((2-temp2)/.02333)-60;
                // moshkele tabdile float be string
                sprintf(power,"%4.2f",temp3);
                Lcd8_Clear();
                Lcd8_Set_Cursor(8,1);
                Lcd8_Write_String("dBm");
                Lcd8_Set_Cursor(1,1);
                Lcd8_Write_String(power);
                _delay_ms(500);
        }
///////////////////////////////////////////////
//Write on 7 Segment
```

```
for(n=0;n<=20;n++){
        for (j=0;j<=3;j++){
                if (j==0){ PORTA=0x80; }
                if (j==1){ PORTA=0x40; }
                if (j==2){ PORTA=0x20; }
                if (j==3){ PORTA=0x10; }
                if (buf[j]==0){ PORTB=0xBF; }
                if (buf[j]==1){ PORTB=0x86; }
                if (buf[j]==2){ PORTB=0xDB; }
                if (buf[j]==3){ PORTB=0xCF; }
                if (buf[j]==4){ PORTB=0xE6; }
                if (buf[j]==5){ PORTB=0xED; }
                if (buf[j]==6){ PORTB=0xFD; }
                if (buf[j]==7){ PORTB=0x87; }
                if (buf[j]==8){ PORTB=0xFF; }
                if (buf[j]==9){ PORTB=0xEF; }
                _delay_ms(50);
        }
                }

}
```

References

[1] B.A.Cetinar,G.R.Crusats,L.Jofre,andB.Necmi,"RF MEMS integrated frequency reconfigurable annular slot antenna," IEEE Trans. Antennas Propag., vol. 58, no. 3, pp. 626–632, Mar. 2010.

[2] A. G. Besoli and F. D. Flaviis, "A multifunctional reconfigurable pix-eled antenna using MEMS technology on printed circuit board," IEEE Trans. Antennas Propag. , vol. 59, no. 12, pp. 4413–4424, Dec. 2011.

[3] M. R. Hamid, P. Gardner, P. S. Hall, and F. Ghanem, "Switched band Vivaldi antenna," IEEE Trans. Antennas Propag., vol. 53, no. 5, pp. 1472–1480, May 2011.

[4] M. F. Jamlos, M. R. Kamarudin, M. A. Jamlos, and M. Jusoh, "A novel reconfigurable quadratic antenna for wimax and 4G systems," Microw. Opt. Technol. Lett., vol. 54, no. 2, pp. 416–421, 2012.

[5] T. Aboufoul, A. Alomainy, and C. Parini, "Reconfiguring UWB monopole antenna for cognitive radio applications using GaAs FET switches," IEEE Antennas Wireless Propag. Lett., vol. 11, pp. 392–394, 2012.

[6]H.A.Majid,M.K.A.Rahim,M.R.Hamid,N.A.Murad,and M. F. Ismail, "Frequency-reconfigurable microstrip patch slot antenna," IEEE Antennas Wireless Propag. Lett. , vol. 12, pp. 218–220, 2013.

[7] Aboufoul, T., Parini, C., Xiaodong, C., Alomainy, A.:'Pattern-reconfigurable planar circular ultra-wideband monopole antenna', IEEE Trans. Antennas Propag., 2013, 61, pp. 4973–4980.

[8] Inseop, L., Sungjoon, L.:'Monopole-like and boresight pattern reconfigurable antenna', IEEE Trans. Antennas Propag., 2013, 61, pp. 5854–5859.

[9] Kang, W.S., Park, J.A., Yoon, Y.J.:'Simple reconfigurable antenna with radiation pattern', Electron. Lett., 2008, 44, pp. 182–183.

[10] Ming-Iu, L., Tzung-Yu, W., Jung-Chin, H., Chun-Hsiung, W., Shyh-Kang, J.:'Compact switched-beam antenna employing a four-element slot antenna array for digital home applications', IEEE Trans. Antennas Propag., 2008,56, pp. 2929–2936.

[11] Pei-Yuan, Q., Guo, Y.J., Can, D.:'A beam switching quasi-Yagi dipole antenna', IEEE Trans. Antennas Propag., 2013, 61, pp. 4891–4899.

[12] Pei-Yuan, Q., Guo, Y.J., Weily, A.R., Chang-Hong, L.:'A pattern reconfigurable U-slot antenna and its applications in MIMO systems', IEEE Trans. Antennas Propag., 2012, 60, pp. 516–528.

[13] Kraus, J.D., Marhefka, R.J.:'Antennas: for all applications' (2011, 3rd edn.).

[14] Pal, A., Mehta, A., Mirshekar-Syahkal, D., Nakano, H.:'Low-profile steerable loop antenna with capacitively coupled feeds', IEEE Antennas Wirel. Propag. Lett., 2012, 11, pp. 873–876.

[15] Pal, A., Mehta, A., Mirshekar-Syahkal, D., Deo, P., Nakano, H.: 'Dual-band low-profile capacitively coupled beam-steerable square-loop antenna',IEEE Trans. Antennas Propag., 2014, 62, pp. 1204–1211.

[16] https://s.campbellsci.com/documents/us/technical-papers/link-budget.pdf

[17] Yueh-Lin Tsai, Ruey-Bing Hwang and Yu-De Lin, "A reconfigurable beam-switching antenna base on active FSS," 2012 15 International Symposium on Antenna Technology and Applied Electromagnetics, Toulouse, 2012, pp. 1-4.

[18] M. Bouslama, M. Traii, T. A. Denidni and A. Gharsallah, "Beam-Switching Antenna With a New Reconfigurable Frequency Selective Surface," in IEEE Antennas and Wireless Propagation Letters, vol. 15, no. , pp. 1159-1162, 2016.

[19] M. Sazegar et al., "Beam Steering Transmitarray Using Tunable Frequency Selective Surface With Integrated Ferroelectric Varactors," in IEEE Transactions on Antennas and Propagation, vol. 60, no. 12, pp. 5690-5699, Dec. 2012.

[20] A. Edalati and T. A. Denidni, "High-Gain Reconfigurable Sectoral Antenna Using an Active Cylindrical FSS Structure," in IEEE Transactions on Antennas and Propagation, vol. 59, no. 7, pp. 2464-2472, July 2011.

[21] M. N. Jazi and T. A. Denidni, "Agile Radiation-Pattern Antenna Based on Active Cylindrical Frequency Selective Surfaces," in *IEEE Antennas and Wireless Propagation Letters*, vol. 9, no. , pp. 387-388, 2010.

[22] J. Li, Q. Zeng, R. Liu and T. A. Denidni, "A Compact Dual-Band Beam-Sweeping Antenna Based on Active Frequency Selective Surfaces," in *IEEE Transactions on Antennas and Propagation*, vol. 65, no. 4, pp. 1542-1549, April 2017.

[23] Y. Shi, Z. Y. Li, K. Li, L. Li and C. H. Liang, "A Retrieval Method of Effective Electromagnetic Parameters for Inhomogeneous Metamaterials," in *IEEE Transactions on Microwave Theory and Techniques*, vol. 65, no. 4, pp. 1160-1178, April 2017.

[24] GMP4200 PIN-Diode Series [Online]. Available: http://www.mi crosemi.com/ datasheets/ gmp4200 % 20 series.pdf

[25] A. Rathore, R. Nilavalan, H.F. AbuTarboush, and T. Peter, "Compact dual-band (2.4/5.2GHz) monopole antenna for WLAN applications," Proceedings of the IWAT 2010, pp. 1–4, Mar. 2010.

[26] J. D. Kraus, Antennas. New York: McGraw-Hill, 1988.

[27] M. I. Jais, M. F. B. Jamlos, M. Jusoh et al., "A novel 2.45 GHz switchable beam textile antenna (Sbta) for outdoor wireless body area network (WBAN) applications," Progress in Electromagnetics Research, vol. 138, pp. 613–627, 2013.